Department of Physics and Astronomy
Heidelberg University

Master Thesis in Physics
submitted by

Raphael Elias Schäfer

born in Frankfurt am Main (Germany)

2025

Numerical simulations of sine-Gordon soliton dynamics realised in a spinor Bose-Einstein condensate

This Master Thesis has been carried out by Raphael Elias Schäfer at the
Kirchhoff-Institut für Physik in Heidelberg
under the supervision of
Prof. Dr. Markus Oberthaler

Abstract

In a recent submission [1], sine-Gordon solitons have been experimentally observed in the relative phase between the ±1- and 0-modes of a spin-1 Bose-Einstein condensate, which was motivated by the derivation of an effective sine-Gordon theory for this system [2]. In this thesis, based on the spin-1 Gross-Pitaevskii equation, numerical studies on these solitons are made. First, single solitons are investigated regarding their velocity dependence on the quadratic Zeeman shift q and their behaviour with regard to experimental imperfections in their preparation. A stable breather solution, albeit with a different relation between amplitude and frequency as for the sine-Gordon breather, is found. Furthermore, the breather also exhibits non-trivial oscillatory dynamics in the other spin-1 observables. In order to efficiently capture the breathers full spin-1 behaviour, a tilting angle is introduced, parametrising the breather's dynamics on the so-called spin-nematic sphere. When preparing the solitons for different tilt angles, they show an additional velocity dependence. For both the initial velocity being controlled by q, and the tilt angle, kink-antikink collisions are then investigated. By utilising the analytical result of the sine-Gordon model for the phase shift, which is the positional shift of a soliton due to the collision, the parameters of an underlying effective sine-Gordon model are extracted, deviating from those derived in [2].

Zusammenfassung

In einem kürzlich eingereichten Artikel [1] wurden Sine-Gordon Solitonen in der relativen Phase zwischen ±1- und 0-Moden in einem Spin-1 Bose-Einstein Kondensat beobachtet. Die Motivation hierfür war ein zuvor erschienener Artikel [2], in dem eine effektive Sine-Gordon Theorie für dieses System hergeleitet wird. In dieser Thesis werden diese Solitonen numerisch auf Basis der Spin-1 Gross-Pitaevskii Gleichung untersucht. Zunächst werden hierbei einzelne Solitonen bezüglich ihrer Geschwindigkeitsabhängigkeit von der quadratischen Zeeman Verschiebung q und Auswirkungen von experimentellen Abweichungen vom korrekten Anfangszustand betrachtet. Wir finden zusätzlich eine stabile „Breather"-Lösung, die allerdings von der Sine-Gordon Vorhersage für die Beziehung zwischen Frequenz und Amplitude abweicht. Außerdem zeigt der Breather nicht-triviale Oszillationsdynamik in anderen Spin-1 Observablen. Um diese effizienter zu beschreiben, wird ein „Kippwinkel" eingeführt, der die Dynamik des Breathers auf der sogenannten Spin-nematischen Kugel parametrisiert. Wenn die Solitonen mit verschiedenen Kippwinkeln präpariert werden, ändert sich ihre Geschwindigkeit. Für die Anfangsgeschwindigkeiten, eingestellt über verschiedene q, sowie verschiedene Kippwinkel, werden außerdem Kollisionen untersucht. Unter Verwendung der analytischen Ergebnisse des Sine-Gordon Modells für die räumliche Verschiebung der Solitonen durch die Kollision werden die Parameter des zugrunde liegenden effektiven Sine-Gordon Modells extrahiert. Die gefundenen Werte weichen von den in [2] hergeleiteten ab.

Contents

1 Introduction

In a wide range of physical systems that contain wave-like phenomena, like, e.g., water [3], clouds [4], signals in neurons [5] or also Bose-Einstein condensates (BECs) [6–9], special wave-packets that have a stable shape over time, even when interacting with other waves, can be observed. These shape-preserving wave-packets are called solitons. They can be obtained as solutions of a wide variety of non-linear models, with a paradigmatic example being the sine-Gordon model. This model of a scalar relativistic field features a periodic potential and inhabits kink-solitons as analytical solutions.

In a recent submission [1], the experimental observation of sine-Gordon solitons existing in the so-called spinorphase φ_S of a quasi-one-dimensional ^{87}Rb spin-1 spinor BEC is reported. This work expands a variety of different solitons found in Bose-Einstein condensates (BECs) over the last 25 years [6–11] and also on more recent experimental observations of new types of solitons, specifically in multi-component BECs, like vector solitons [12], and magnetic solitons [13, 14]. As the sine-Gordon solitons in the spin-1 spinor BEC feature a magnetic domain wall, specifically in the transverse spin, a connection to recent theoretical studies on solitons in a spinor BEC can be made [15–19].

The realisation of sine-Gordon solitons in a spin-1 spinor BEC was motivated by a recently developed low energy effective field theory (LEEFT) [2], which introduced a double sine-Gordon model in the easy-plane phase of a spin-1 spinor BEC in the spinorphase φ_S, which is the phase between the ±1- and 0-modes of a spin-1 system. The double sine-Gordon model expands the sine-Gordon model by an additional periodic potential with double the frequency of the sine-Gordon potential, thereby breaking the integrability of the sine-Gordon model. In particular, the specific effective sine-Gordon model has its sine-Gordon limit, so the double frequency potential being significantly smaller than the sine-Gordon potential, at a quadratic Zeeman shift, which defines the energy balance of spin-changing collisions, of $q \to 0$. This limit will be the main subject of this thesis, mainly regarding the questions in which range of q this limit is valid, which phenomena of the sine-Gordon model can be observed in the spinor BEC and at which points additional spin-1 effects must be considered. Furthermore, controlling the quadratic Zeeman shift, potentially allows probing the transition from the integrable sine-Gordon model to the non-integrable double sine-Gordon model.

In order to characterise the experimentally generated solitons, a 1D spin-1 simulation of the Gross-Pitaevskii equation (GPE) is used, especially to better understand their interactions and compare them to results from the sine-Gordon model. For this, collisions between solitons are an interesting topic, as there exist analytical predictions capturing the interaction effects during collision in the sine-Gordon model. Building upon soliton simulations, it is also tested whether breather solutions, which are a key feature of the

sine-Gordon model, also exist in the spin-1 system.

This thesis is structured as follows: First, the theoretical and experimental background will be introduced in Sec. 2. After this, in Sec. 3 the initial conditions used for realising the solitons in the simulation are presented and the behaviour of single solitons at different q is discussed. In this discussion, different initial conditions that mimic experimental imperfections are also simulated to gain a better understanding of the dependence of the dynamics of the soliton on these. After this a sine-Gordon breather initial condition in the spinorphase is simulated at $q = 0$ in Sec. 4. In this section the so-called spin-nematic sphere, which incorporates an additional spin-1 observable, proves to be a useful space for observing the breather dynamics. Expanding on this insight "tilted solitons", which explore this additional degree of freedom are simulated and described in Sec.5. The effects of this tilting and a first experimental realisation are further discussed in this section. In Sec. 6 kink-antikink collisions for different incoming velocities are then simulated to characterise their interaction and compare it with results from sine-Gordon theory. The results are then discussed in Sec. 7 and an outlook on possible future investigations arising from this is provided.

2 Theoretical and experimental background

In the following, first, the spin-1 system and then specifically the spin-1 BEC in the mean-field limit are introduced. After this a short overview of the general experimental system of the ^{87}Rb BEC is given. To define the framework of the effective theory, the sine-Gordon model and the solutions from it that are later used are introduced and then the LEEFT for the spinorphase, introduced in [2], is summarised. Finally, a short overview of the basis of the spin-1 GPE simulation is also given.

2.1 Spin-1 System

In this part the spin-1 system at the single particle level is introduced based on [20, 21]. Its general state $\vec{\psi}$ can be written as three modes ψ_m corresponding to the states in the three possible magnetic quantum numbers in spin-1, $m = 0, \pm 1$. Each mode can be defined by a real probability amplitude r_m, such that $\sum_m r_m^2 = 1$, and its real-valued phase φ_m, leading to the state as a three component vector:

$$\vec{\psi} = \begin{pmatrix} \psi_{+1} \\ \psi_0 \\ \psi_{-1} \end{pmatrix} = \begin{pmatrix} r_{+1} \mathrm{e}^{\mathrm{i}\varphi_{+1}} \\ r_0 \mathrm{e}^{\mathrm{i}\varphi_0} \\ r_{-1} \mathrm{e}^{\mathrm{i}\varphi_{-1}} \end{pmatrix} \tag{1}$$

By pulling out a global phase and introducing the spinorphase φ_S, as the phase between the $m = 0$- and $m = \pm 1$-modes, and the Larmorphase φ_L, as the phase difference between the two outside-modes,

$$\varphi_\mathrm{S} = \varphi_0 - \frac{1}{2}(\varphi_{+1} + \varphi_{-1}) \,, \tag{2}$$

$$\varphi_\mathrm{L} = \varphi_{+1} - \varphi_{-1} \,, \tag{3}$$

the state can be rewritten to only depend on these two phases and the probability amplitudes:

$$\psi = \begin{pmatrix} r_{+1} \mathrm{e}^{\mathrm{i}\varphi_\mathrm{L}/2} \\ r_0 \mathrm{e}^{\mathrm{i}\varphi_\mathrm{S}} \\ r_{-1} \mathrm{e}^{-\mathrm{i}\varphi_\mathrm{L}/2} \end{pmatrix} \tag{4}$$

As the spin-1 system used in the following is based on the hyperfine structure of ^{87}Rb, the spin and the basic spin-observables will be denoted by F and F_i in the following. The spin-observables F_i, with $i = x, y, z$, make up the first three observables of the spin-1

system used here. The operators $\hat{F}_i$ used to measure them in matrix form are:

$$\hat{F}_x = \frac{1}{\sqrt{2}} \begin{pmatrix} 0 & 1 & 0 \\ 1 & 0 & 1 \\ 0 & 1 & 0 \end{pmatrix} , \quad \hat{F}_y = \frac{1}{\sqrt{2}} \begin{pmatrix} 0 & -\mathrm{i} & 0 \\ \mathrm{i} & 0 & -\mathrm{i} \\ 0 & \mathrm{i} & 0 \end{pmatrix} , \quad \hat{F}_z = \begin{pmatrix} 1 & 0 & 0 \\ 0 & 0 & 0 \\ 0 & 0 & -1 \end{pmatrix} \tag{5}$$

To visualise the expectation values of a state in these observables the so-called spin-sphere can be used. On this sphere the angle between the state's orientation in the F_x-F_y-plane and the F_x-axis is the Larmorphase φ_L. In the spin-1 system, five additional operators are needed to fully describe the system for which the quadrupole operators $\hat{Q}_{ij}$ are chosen here. These operators are defined via the anticommutator of the spin operators $\hat{F}_i$ and the identity operator $\mathbb{1}_3$ as:

$$Q_{ij} = \{\hat{F}_i, \hat{F}_j\} - \frac{4}{3}\delta_{ij}\mathbb{1}_3 \tag{6}$$

2.1.1 Spin-Nematic sphere

With the observables Q_{yz} and Q_{xz} from this definition, F_x and F_y, and the additional observable Q_0 defined by the operator

$$\hat{Q}_0 = -\frac{1}{3}\mathbb{1}_3 - \hat{Q}_{zz} = \begin{pmatrix} -1 & 0 & 0 \\ 0 & 1 & 0 \\ 0 & 0 & -1 \end{pmatrix} , \tag{7}$$

the so-called spin-nematic subspace [21, 22] can be defined. For this, the transversal spin $\hat{F}_\perp$ and $\hat{Q}_\perp$ are defined as operators with the Larmorphase as:

$$\hat{F}_\perp = \cos\varphi_\mathrm{L}\hat{F}_x + \sin\varphi_\mathrm{L}\hat{F}_y \tag{8}$$

$$\hat{Q}_\perp = \cos\varphi_\mathrm{L}\hat{Q}_{yz} - \sin\varphi_\mathrm{L}\hat{Q}_{xz} \tag{9}$$

The observables $F_\perp$, $Q_\perp$ and Q_0 then can be visualised on the spin-nematic sphere. On this sphere the angle between $F_\perp$ and $Q_\perp$ is the spinorphase φ_S. In the following a homogenous φ_L will be considered when talking about a one-dimensional spin-1 system. Due to the underlying symmetry, only $\hat{F}_x$ and $\hat{Q}_{yz}$ will be considered, as by rotating the observables around F_z, the axis along which the spin is oriented can be aligned with F_x.

2.1.2 Mean-field description of the BEC

To describe the dynamics in a spinor-BEC at high densities a mean-field approach can be used [20, 21]. In this approach the space- and time-dependent field operators of each mode $\hat{\Psi}_m(\vec{x}, t)$ can be replaced by their expectation values $\psi_m(\vec{x}, t) = \sqrt{n_m(\vec{x}, t)}\mathrm{e}^{\mathrm{i}\varphi_m(\vec{x},t)}$ making the expectation value becoming continuous and also allowing the resulting function to be

written using the spinor- and Larmorphase, like Eq. 4. For the purpose of this thesis, this state is sufficient, as both the simulations and the experiment work close to mean-field level. By transforming the mean-field Hamiltonian [20] into a rotating frame, the linear Zeeman shift can be eliminated, leaving:

$$\hat{H}_{\mathrm{MF}} = \sum_{m=-1}^{+1} \psi_m^* \left(-\frac{\hbar^2 \vec{\nabla}^2}{2M} + V_{\mathrm{trap}} + qm^2 \right) \psi_m + \frac{c_0}{2} n^2 + \frac{c_1}{2} |\vec{F}|^2 \tag{10}$$

Here M is the mass of a single atom, q the quadratic Zeeman shift, c_0 the contact-interaction strength, c_1 the spin-spin interaction strength, n the total density and $\vec{F}$ the spin density vector which is given by:

$$\vec{F} = \begin{pmatrix} F_x \\ F_y \\ F_z \end{pmatrix} , \quad \text{with } F_i = \vec{\psi}^\dagger \hat{F}_i \vec{\psi} \tag{11}$$

In this one can also define the characteristic spatial and temporal scales as

$$\xi_{\mathrm{s}} = \frac{\hbar}{\sqrt{2Mn|c_1|}} , \quad \text{and} \quad t_{\mathrm{s}} = \frac{\hbar}{n|c_1|} , \tag{12}$$

where ξ_{s} is the spin healing length and t_{s} the spin interaction time. Often t_{s} is defined with an additional factor 2π, but as the dimensionless unit of time of the LEEFT matches t_{s} as defined above, compare Sec. 2.4, for consistency, this definition is used in this thesis.

2.1.3 Single-mode-approximation

As ^{87}Rb features $|c_0| \gg |c_1|$, the total density will be assumed to be in good approximation flat. The relevant dynamics are then mainly captured in the spin degree of freedom. If then going into the single mode approximation (SMA), i.e. the system size is smaller than the spin healing length ξ_{s}, meaning the spatial wave function $\psi(\vec{r})$ is valid for all modes,

$$\hat{H}_{\mathrm{SMA}} = \frac{c_1}{2} \hbar \hat{\vec{F}}^2 - \frac{q}{2} \hbar \hat{Q}_0 , \tag{13}$$

can be used as the Hamiltonian of the system [22]. In the ground state of the easy-plane phase (see Sec. 2.1.4) F_z becomes zero, with which the Hamiltonian can be reduced to F_x, F_y and Q_0. The dynamics for states close to this ground state with $\langle F_z^2 \rangle = 0$ are then located in the spin-nematic-subspace, meaning that the dynamics of the system can be understood on the spin-nematic sphere.

Considering iso-energy lines shown in Fig. 1, one finds, for q in the easy-plane, the so-called separatrix, corresponding to the black eight-like shape in the figure. In the middle

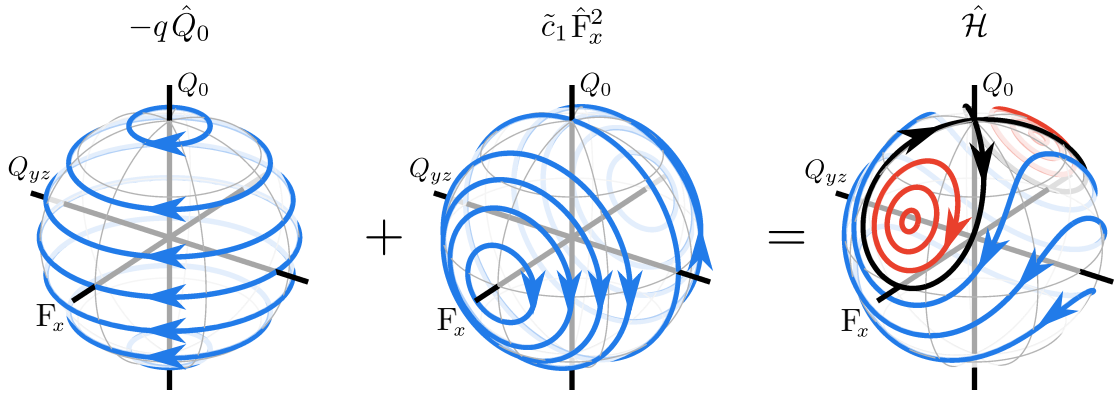

Figure 1: The dynamics on the spin-nematic sphere in the SMA for $q = n|c_1|$ first for the two contributing parts, then added together. The separatrix can be seen in black and the bound trajectories around the fix point in red. The figure is adapted from [21].

of the red circles in the eight, the fix points for the set q are located and when changing q also the size of the separatrix changes as the fix points move, as, like also shown in the figure, the contribution of the $\hat{Q}_0$-part of the Hamiltonian changes.

2.1.4 Phase-diagram

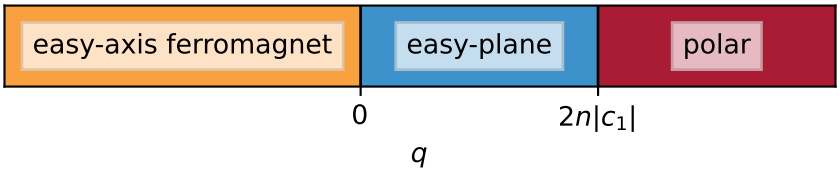

Figure 2: The phase diagram of the spin-1 spinor BEC at a constant $c_1 < 0$.

For the spin-spin-interaction strength $c_1 < 0$ (ferromagnetic interactions) a spinor BEC features three different phases depending on the quadratic Zeeman shift q [23]. Each of these phases show a characteristic ground state. For $q < 0$ the BEC is in the so-called Easy-Axis Ferromagnet phase, where the single-mode ground state is a fully elongated F_z-Spin, so the entire population in either $m_F = +1$ or $m_F = -1$. On the spin sphere this corresponds to the state being located at one of the poles, while at the spin-nematic sphere it is on the south pole (see Fig. A1).

For $q > 2n|c_1|$ the system is in the polar phase. In the ground state of this phase all atoms are in the $m_F = 0$ mode, leading to $Q_0 = 1$ and the state being located at the north pole of the spin-nematic sphere, as shown in Fig. A2.

The phase in which most of the simulations discussed in this thesis are done is the so-called Easy-Plane Ferromagnet phase at $0 < q < 2n|c_1|$. In this phase, the ground state depends on the value of q and corresponds to a spin in the plane spanned by F_x and F_y, the length of which decreases with q leading to a finite positive expectation value of

Q_0. Both the state in the plane and the finite value of Q_0 is shown for three different q in Fig. 3. This ground state is given by:

$$\boldsymbol{\psi}_{\mathrm{EP}} = \sqrt{n}\begin{pmatrix} \frac{1}{2}\sqrt{1-\frac{q}{2n|c_1|}}\mathrm{e}^{\mathrm{i}\varphi_{\mathrm{L}}/2} \\ \frac{1}{\sqrt{2}}\sqrt{1+\frac{q}{2n|c_1|}} \\ \frac{1}{2}\sqrt{1-\frac{q}{2n|c_1|}}\mathrm{e}^{-\mathrm{i}\varphi_{\mathrm{L}}/2} \end{pmatrix} \overset{q\to 0}{\to} \sqrt{n}\begin{pmatrix} \frac{1}{2}\mathrm{e}^{\mathrm{i}\varphi_{\mathrm{L}}/2} \\ \frac{1}{\sqrt{2}} \\ \frac{1}{2}\mathrm{e}^{-\mathrm{i}\varphi_{\mathrm{L}}/2} \end{pmatrix} \tag{14}$$

If the value of Q_0 or $F_\perp$ is not exactly matched to the ground state for the set q, these values oscillate around the correct value, which will be explained in the following.

In the experiment the control of the phase via the quadratic Zeeman shift q is realised by a microwave (MW) dressing [24, 25]. Over time the actual value of q set by this changes slightly, which becomes inherently obvious in the easy-plane phase of the spinor BEC, as in this phase the background has a preferred transversal spin length $|F_\perp|$, as can be seen in the potential, shown in Fig. 4 for three different q. If this value is not matched, $|F_\perp|$ oscillates around it [25] and Q_0 oscillates shifted in phase by π around its stable value. This can also be seen from the single mode dynamics in the previous section, shown in Fig. 1. When always preparing an elongated spin $|F_\perp| \approx 1$, one can use this to find $q = 0$. While this is a valid method to achieve this, in the experiment it will also always have some inaccuracy, as it is impossible to imprint a truly fully elongated spin due to noise and the amplitude of the oscillation reaching the level of the background noise already for finite q.

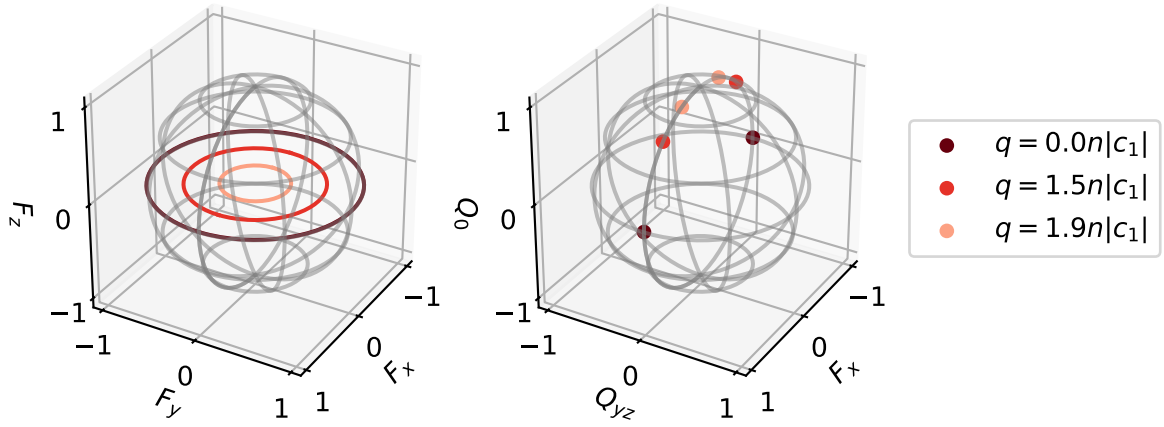

Figure 3: The ground state of the easy-plane phase for three different q on the spin- (left) and spin-nematic sphere (right). The orientation on the circle for the length given by q depends on the Larmorphase. For a Larmorphase of 0 and π the ground states are shown on the nematic sphere. For each φ_{L} a nematic sphere with the corresponding $F_\perp$ and $Q_\perp$ exists, where the state looks the same. Here the ground state moves from the equator upwards on the surface of the sphere along the line with $Q_{yz} = 0$ for a larger q.

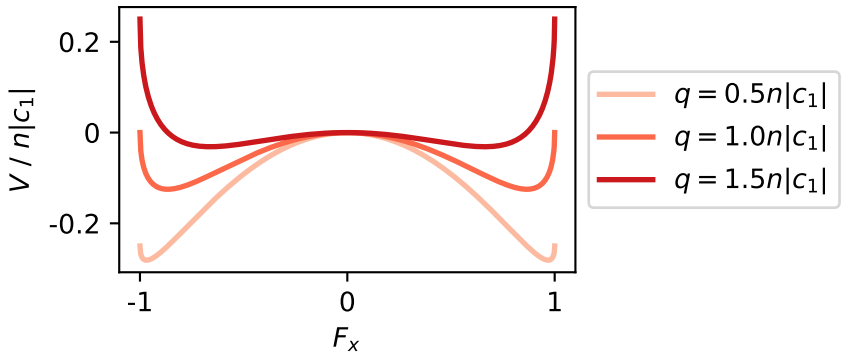

Figure 4: The potential in the transversal spin (here φ_{L} is chosen again such that this is F_x) for three different values of q. The local maximum at $F_x = 0$ is shifted to 0. This potential corresponds to a cut through the spin-nematic sphere shown in Fig. 1 along the line with $Q_{yz} = 0$ on the hemisphere with positive Q_0.

2.2 Experimental system

The experimental system [21, 24, 26] consists of multiple cooling and trapping stages for the ^{87}Rb-atoms. Starting with two magneto-optical traps the atoms are transferred in a magnetic trap trap before loading the dipole trap. Here they are condensed and prepared in the desired initial state for the time evolution. In the electronic ground state of ^{87}Rb the $F = 1$ and $F = 2$ levels of the hyperfine structure are accessible, leading to eight different states. To shift the atoms between these states, Rabi oscillations can be driven by MW or radiofrequency (RF) pulses. The coils used for this and the level structure are shown in Fig. 5. A MW-dressing can also be applied during the time evolution to control the quadratic Zeeman shift q. For this first a magnetic offset field is applied and then the MW shifts the level back to a controllable value of q. To change the spin-basis in which the measurement is taken the RF-pulses can be applied using two coils. This is for example used for the readout of observables different to F_z. For measuring multiple non-commuting observables in one readout a POVM readout utilising the additional five levels in $F = 2$ can be performed [27],[21]. For this readout some statistical accuracy is exchanged for measuring up to three different non-commuting observables by splitting the BEC into up to three different observable bases and then performing the readout. To perform the measurement, a magnetic field gradient is applied, leading to the atoms separating into the different levels, i.e. a Stern-Gerlach measurement is done, before an absorption image is taken, for which an example is shown in Fig. 5 (c).

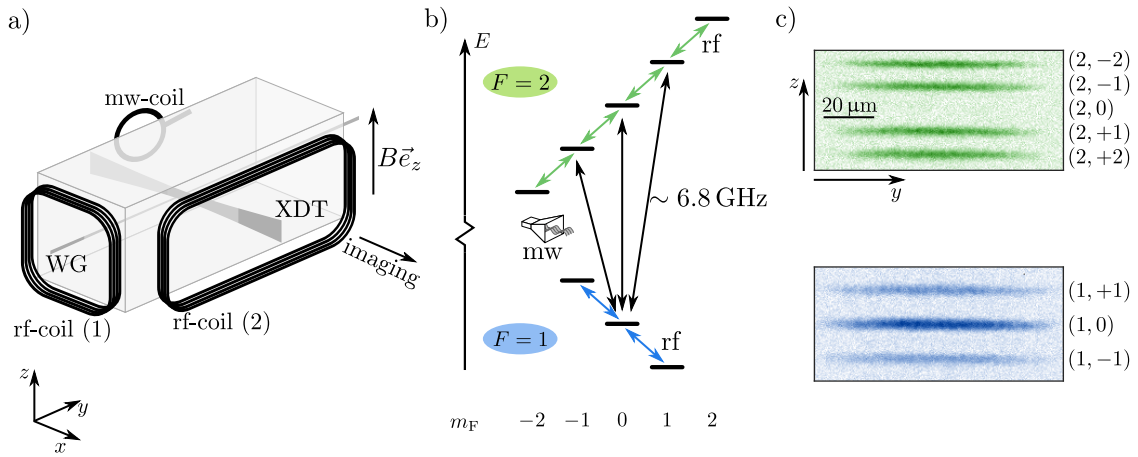

Figure 5: (a) The setup of the dipole trap and the RF- and MW-coils, along with the magnetic offset field in z-direction. (b) The level structure of ^{87}Rb accessible in the experiment. (c) An example for the images taken in $F = 2$ and $F = 1$ using the Stern-Gerlach imaging. The figure is adapted from [21].

2.3 The sine-Gordon model

A popular theoretical model for systems featuring a periodic potential, as shown in Fig. 6, is the so-called sine-Gordon model [28, 29]. This model is based on a specific equation of motion for a phase φ, the sine-Gordon equation:

$$\partial_t^2 \varphi - \partial_x^2 \varphi + \frac{m^2}{\beta} \sin(\beta\varphi) = 0 \tag{15}$$

In the shape given above space x and time t are both dimensionless, m is the dimensionless sine-Gordon mass and β is the parameter of nonlinearity [29]. Effectively m changes the amplitude of the potential $V(\varphi) = -(m/\beta)^2 \cos(\beta\varphi)$ (shown in Fig. 6), so its strength compared to the dimensionless kinetic energy and β changes its periodicity. For a dimensionless x and t the speed of light c equals one. One of the main characteristics of the sine-Gordon model is that it inhabits analytical soliton solutions. The two main soliton solutions are a kink K and an antikink $\overline{K}$ which for a soliton velocity v and an initial position $x(t = 0) = x_0$ are given by:

$$\varphi_{K,\overline{K}}(x,t) = \pm\frac{4}{\beta} \arctan\left(\exp\left(m\frac{x - vt - x_0}{\sqrt{1 - v^2}}\right)\right) \tag{16}$$

For two combinations of m and β the kink with $v = 0$ is shown in Fig. 6

If a sine-Gordon kink and an antikink collide, the phase performs a flip and in the outgoing positions of both are shifted relative to their incoming trajectories, as can be seen in Fig. 7. This shift in position is called phase shift δx and is given by the spatial difference at a time $t = t'$ of the in- and outgoing trajectories of the solitons. For a system

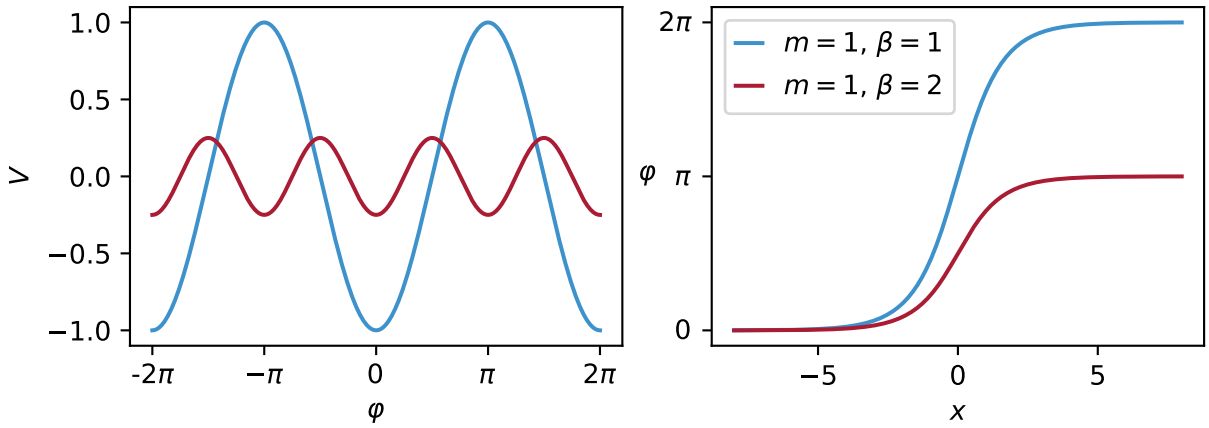

Figure 6: On the left the potential of the sine-Gordon model for two different combinations of m and β is shown. For the same combinations on the right the spatial profile of the kink with $v = 0$ is plotted.

exactly following the sine-Gordon model, the time t', at which the phase shift is measured, does not matter as the kink-antikink collision is fully elastic, $v_{\text{in}} = v_{\text{out}}$. If the velocities of kink v_K and antikink $v_{\overline{K}}$ have equal absolute values $v_K = -v_{\overline{K}}$ the phase shift of both the kink and antikink is also the same in absolute value and is given by [29, 30]:

$$\delta x = \operatorname{sgn}(v)\,\frac{2\sqrt{1-v^2}}{m}\ln\left|\frac{1}{v}\right| \tag{17}$$

Note that for the sine-Gordon model the collision point of the incoming trajectories occurs at a later time than for the outgoing trajectories, as the kink-antikink interaction is attractive.

Another interesting solution special to the sine-Gordon model is the so-called breather. It oscillates with a frequency ω and for a starting phase φ_0 is given by:

$$\varphi_{\text{br}}(x,t) = \frac{4}{\beta}\arctan\left(\frac{\sqrt{1-\omega^2}}{\omega}\,\frac{\sin\left(\frac{m\omega}{\sqrt{1-v^2}}\,(t-vx)-\varphi_0\right)}{\cosh\left(\frac{m\sqrt{1-\omega^2}}{\sqrt{1-v^2}}\,(x-vt-x_0)\right)}\right) \tag{18}$$

The observed frequency of the oscillation ω_{obs} is also directly coupled to the maximum amplitude A of the breather [28], which is also visible in Fig. 8. The relation between the two can be read from Eq. 18 using the frequency to amplitude relation given in [28] and that for $m = 1$, $\omega_{\text{obs}} = \omega$ and is given by:

$$A = \frac{4}{\beta}\arccos\left(\frac{\omega_{\text{obs}}}{m}\right) \tag{19}$$

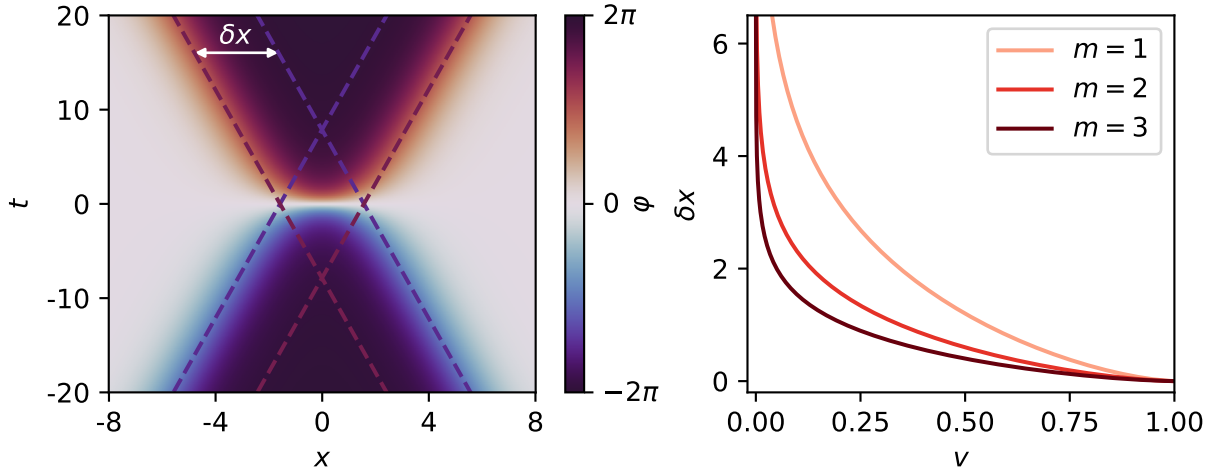

Figure 7: (left) Collision of a kink and antikink in the sine-Gordon model. The phase shift δx between in- and outgoing trajectories is clearly visible and also the jump in the phase from -2π to 2π between the kink and antikink is visible. (right) The phase shift δx against the incoming velocity of kink and antikink as expressed by eq. 17 for three different values of the mass term m in the sine-Gordon equation (eq. 15).

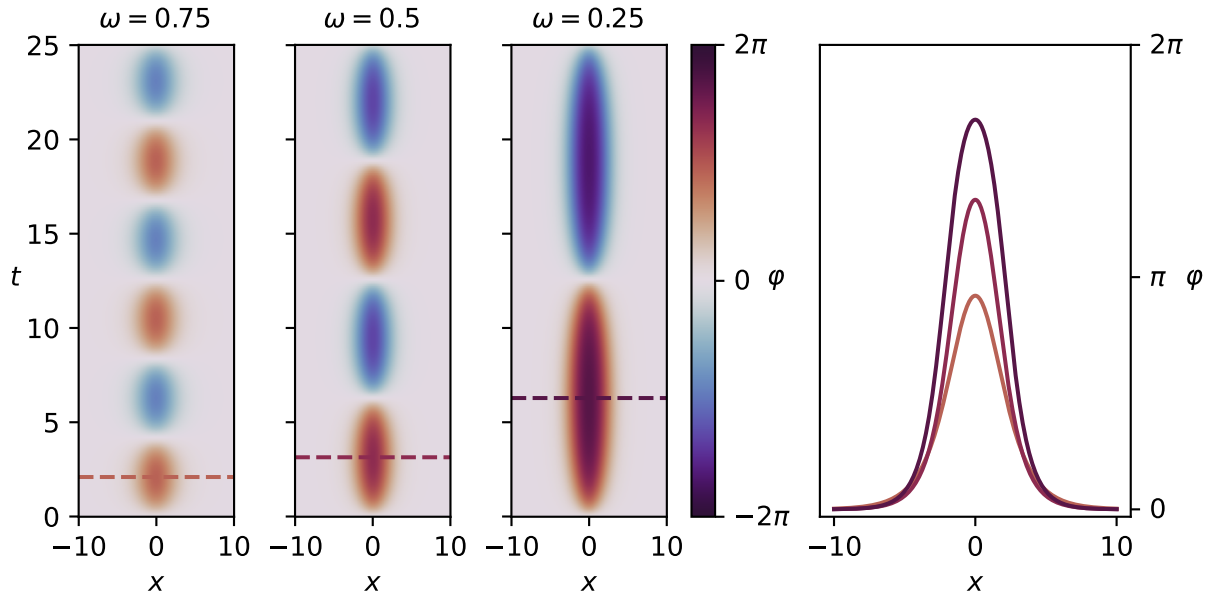

Figure 8: (On the left three breathers for $m = \beta = 1$ with different frequencies ω are shown. On the right the change in amplitude and width related to the change in frequency can be seen by comparing slices at the maximum of each breather.

2.3.1 Double Sine-Gordon model

The sine-Gordon model can be extended by another periodic term with double the frequency of the general periodicity, leading to a potential that can for example be parametrised as [31]:

$$V(\varphi) = -\frac{4}{1+|4\eta|}\left(-\cos\frac{\varphi}{2} + \eta\cos\varphi\right) \tag{20}$$

This leads to an equation of motion of the following shape:

$$\partial_t^2\varphi - \partial_x^2\varphi + \frac{2}{1+|4\eta|}\left(-\sin\frac{\varphi}{2} + 2\eta\sin\varphi\right) = 0 \tag{21}$$

The resulting model is called double sine-Gordon model, as it features a double frequency term. To tune the strength of the double frequency term compared to the sine-Gordon term, $\eta \in \mathbb{R}$ is changed. In the double sine-Gordon model also soliton solutions exist, which depending on η, change their spatial profile [31]. For $\eta < -\frac{1}{4}$ two (anti-)kink solutions exist, interpolating between the different minima. In this thesis the focus will be on the limit of the effective theory (see Sec. 2.4 where $|\eta| < \frac{1}{4}$. In this range the potential still only possesses a minimum and a maximum at the positions where it would be for the underlying pure sine-Gordon, as shown in Fig. 9. Due to this, the soliton solutions in it still look similar to sine-Gordon solitons for this region of η, changing their steepness in the spatial profile and for $\eta > 1/4$ seemingly splitting up in two, which is expressed as [31]:

$$\varphi_{\mathrm{K},\overline{\mathrm{K}}} = \pm 4\arctan\left[\sqrt{\frac{1}{1+4\eta}}\sinh\left(\sqrt{\frac{1+4\eta}{1+|4\eta|}}\cdot x\right)\right] \tag{22}$$

This expression leads to an (anti-)kink for all $\eta > -\frac{1}{4}$ and for two $|\eta| < \frac{1}{4}$ is compared to the sine-Gordon kink ($\eta = 0$) in Fig. 10.

In contrast to the sine-Gordon model, collisions in the double sine-Gordon model are not necessarily elastic, as it is a non-integrable model. But, due to this, at low collision velocities so-called n-bounce collisions can occur. In these collisions the solitons collide again for n times after a first collision. An interesting feature of these collisions is the fractal nature of their resonance spectrum [31, 32].

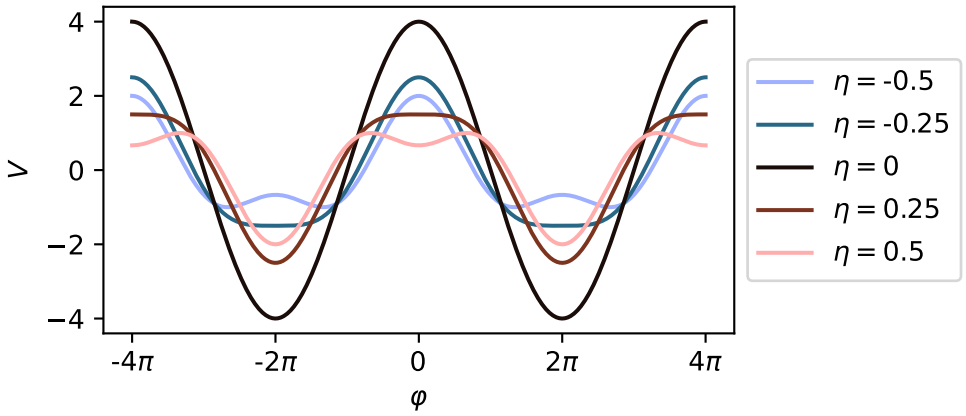

Figure 9: The potential of the double sine-Gordon model for different values of η. The case $\eta = 0$ corresponds to the sine-Gordon potential. As one can see, the potential topologically is similar to the sine-Gordon model up to $|\eta| = 1/4$. For $|\eta| > 1/4$, depending on the sign, the minima or the maxima split up into two separate extrema.

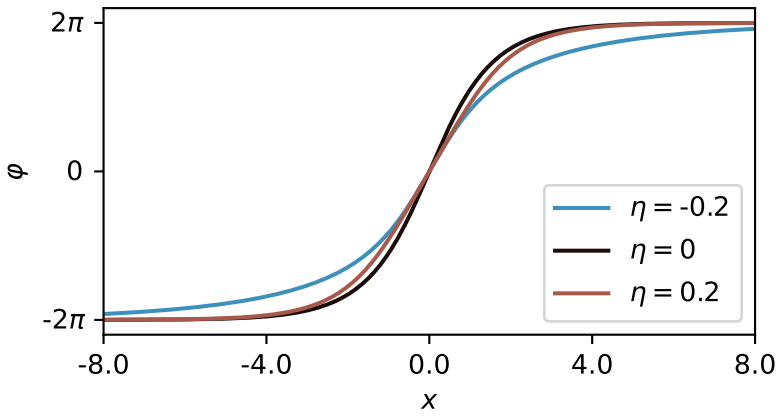

Figure 10: The kink solution for $\eta > -1/4$ (Eq. 22) in the double sine-Gordon model for three different values of η. The case $\eta = 0$ corresponds to the sine-Gordon case, from which the case $\eta = 0.2$ only weakly deviates. For the negative $\eta = -0.2$ the deviation is stronger and the kink is visibly more stretched.

2.4 Low Energy Effective Field Theory for Easy-Plane

In a recent publication [2] a low energy effective field theory (LEEFT) for a spin-1 BEC in the easy-plane phase was developed. In this LEEFT the Spinor BEC can be reduced to only the spinorphase φ_{S} being needed for describing the dynamics of the system. For φ_{S} the theory corresponds to a double sine-Gordon model, in which the strength of the double frequency term depends polynomial on the quadratic Zeeman shift q. Depending on the dominant wavenumber regime, two different dependencies are found. For $k \approx 0$ the Lagrangian density in one dimension reads as:

$$\begin{aligned}\mathcal{L}^{\mathrm{eff}}_{\varphi_{\mathrm{S}}} = &-\frac{\hbar}{8c_1}\dot{\varphi}_S^2 - \frac{\hbar n_1(n-2n_1)}{Mn}\left(\partial_x\varphi_{\mathrm{S}}\right)^2 \\ &-\frac{1}{\hbar}\left(2c_1n_1(n-2n_1) - \frac{q^2}{16c_1}\right)\cos\left(2\varphi_{\mathrm{S}}\right) + \frac{q^2}{32c_1\hbar}\sin^2(2\varphi_{\mathrm{S}})\end{aligned} \tag{23}$$

Here n is the total density of the BEC and n_1 is the density of one of the side-modes ($m = \pm 1$) of the BEC in the Easy-Plane ground state, see Eq. 14, for the specific q used. This can be transformed to dimensionless variables $\overline{x}$, $\overline{t}$ and $\overline{\mathcal{L}}^{\mathrm{eff}}$ using $k_{\xi_{\mathrm{s}}} = \frac{\sqrt{2Mn|c_1|}}{\hbar}$:

$$x = \frac{1}{k_{\xi_{\mathrm{s}}}}\overline{x} = \xi_{\mathrm{s}}\overline{x} \tag{24}$$

$$t = \frac{2M}{\hbar k_{\xi_{\mathrm{s}}}^2}\overline{t} = \frac{\hbar}{n|c_1|}\overline{t} = t_{\mathrm{s}}\overline{t} \tag{25}$$

$$\mathcal{L}^{\mathrm{eff}} = \frac{\hbar n k_{\xi_{\mathrm{s}}}^2}{2M}\overline{\mathcal{L}}^{\mathrm{eff}} \tag{26}$$

When additionally using the relations

$$n_1 = \frac{2|c_1|n - q}{8|c_1|}\,, \quad \text{and} \tag{27}$$

$$\overline{q} = \frac{q}{2n|c_1|}\,, \tag{28}$$

one obtains:

$$\overline{\mathcal{L}}^{\mathrm{eff}}_{\varphi_{\mathrm{S}}} = \frac{1}{4}\left[\frac{1}{2}\left(\partial_{\overline{t}}\varphi_{\mathrm{S}}\right)^2 - \left(1-\overline{q}^2\right)\left(\partial_{\overline{x}}\varphi_{\mathrm{S}}\right)^2 + \left(1-2\overline{q}^2\right)\cos\left(2\varphi_{\mathrm{S}}\right) - \frac{\overline{q}^2}{2}\sin^2(2\varphi_{\mathrm{S}})\right] \tag{29}$$

For the dominant wave numbers being on the scale of the spin-interaction $k \approx k_{\xi_{\mathrm{s}}}$ the dimensionless Lagrangian reads:

$$\overline{\mathcal{L}}^{\mathrm{eff}}_{\varphi_{\mathrm{S}}} = \frac{1-\overline{q}^2}{4}\left[\left(\partial_{\overline{t}}\varphi_{\mathrm{S}}\right)^2 - \left(\partial_{\overline{x}}\varphi_{\mathrm{S}}\right)^2\right] + \overline{A}\cos\left(2\varphi_{\mathrm{S}}\right) - \overline{B}\sin^2(2\varphi_{\mathrm{S}})\,, \quad \text{with} \tag{30}$$

$$\overline{A} = \frac{1-\overline{q}^2}{4}\left(1 - 2\overline{q}^2 + 4\overline{q}^2(1-\overline{q}^2) + 8\overline{q}^2(1-\overline{q}^2)^2\right)\,, \tag{31}$$

$$\overline{B} = q^2 \frac{1-\overline{q}^2}{4}\left(1 + 4(1-\overline{q}^2) + 4(1-\overline{q}^2)^2\right) \tag{32}$$

The equations of motion then become by using Euler-Lagrange:

$$0 = \partial_{\overline{t}}^2\varphi_{\mathrm{S}} - 2(1-\overline{q}^2)\partial_{\overline{x}}^2\varphi_{\mathrm{S}} + 2(1-2\overline{q}^2)\sin(2\varphi_{\mathrm{S}}) + \overline{q}^2\sin(4\varphi_{\mathrm{S}})\,, \quad \text{for } k \approx 0 \tag{33}$$

$$0 = \partial_{\overline{t}}^2\varphi_{\mathrm{S}} - \partial_{\overline{x}}^2\varphi_{\mathrm{S}} + \frac{4\overline{A}}{1-\overline{q}^2}\sin(2\varphi_{\mathrm{S}}) + \frac{4\overline{B}}{1-\overline{q}^2}\sin(4\varphi_{\mathrm{S}})\,, \quad \text{for } k \approx k_{\xi_{\mathrm{s}}} \tag{34}$$

To make the equation of motion for the case $k \approx 0$ (Eq. 33) completely dimensionless, one has to transform $\overline{x}$ again to:

$$\tilde{x} = \frac{1}{\sqrt{2(1-\overline{q}^2)}}\overline{x} = \frac{k_{\xi_{\mathrm{s}}}}{\sqrt{2(1-\overline{q}^2)}}x \tag{35}$$

Assuming $q \approx 0$, the system can, in good approximation, be described by a sine-Gordon model. The easiest parameter to measure in the experiment is the width of the soliton ℓ. From Eq. 16 one can see that this depends not only on the transformation to dimensionless space $\frac{\overline{x}}{x}$ (or $\frac{\tilde{x}}{x}$ respectively) but also on the sine-Gordon mass m, like $\ell = \sqrt{1-v^2}\frac{x}{m\overline{x}}$ (or $\ell = \sqrt{1-v^2}\frac{x}{m\tilde{x}}$ respectively). The mass in the for small q can be directly taken from the equations of motion using $\beta = 2$ and following Eq. 15:

$$m = 2\sqrt{1-2\overline{q}^2} \overset{\overline{q}\to 0}{=} 2\,, \quad \text{for } k \approx 0 \tag{36}$$

$$m = 2\sqrt{\frac{2\overline{A}}{1-\overline{q}^2}} \overset{\overline{q}\to 0}{=} \sqrt{2}\,, \quad \text{for } k \approx k_{\xi_{\mathrm{s}}} \tag{37}$$

This leads to:

$$\ell_0 = \sqrt{1-v^2}\sqrt{\frac{1-\overline{q}^2}{1-2\overline{q}^2}}\frac{1}{\sqrt{2}k_{\xi_{\mathrm{s}}}}\,, \quad \text{for } k \approx 0 \tag{38}$$

$$\ell_{k_{\xi_{\mathrm{s}}}} = \sqrt{1-v^2}\sqrt{\frac{1-\overline{q}^2}{2\overline{A}}}\frac{1}{2k_{\xi_{\mathrm{s}}}}\,, \quad \text{for } k \approx k_{\xi_{\mathrm{s}}} \tag{39}$$

Assuming $v \approx 0$ and $q \approx 0$ both equations give:

$$\ell = \frac{1}{\sqrt{2}k_{\xi_{\mathrm{s}}}} = \frac{\hbar}{\sqrt{4Mn|c_1|}} \tag{40}$$

When rearranging this relation, one can get a good approximation for the effective 1D-density in the experiment from the measured soliton width at a small q and $v \approx 0$. If the atom number and trap size stay approximately the same, this effective 1D-density should then also be valid for a larger q at which the soliton width might not be given by this

relation any more. By this, one can also calculate the transformation in space and time for small q:

$$x = \sqrt{2}\ell\overline{x} \tag{41}$$

$$t = \frac{4M\ell^2}{\hbar}\overline{t} \tag{42}$$

These transformations are especially needed to obtain dimensionless velocities v from measured velocities v_{meas}:

$$v = \frac{\overline{x}}{x}\frac{t}{\overline{t}}v_{\text{meas}} = \frac{2M}{\hbar k_{\xi_s}}v_{\text{meas}} \overset{q\to 0}{=} \frac{2\sqrt{2}M\ell}{\hbar}v_{\text{meas}} \tag{43}$$

When comparing the potential for the $k \approx 0$ case, see Fig. 11, with the potential of the double sine-Gordon definition before, see Fig. 9, one can see that up to $\overline{q} \gtrsim 0.5$, so $q \gtrsim |c_1|$, the potential is in the regime of the double sine-Gordon potential with $0 \leq \eta < \frac{1}{4}$. In this range of η the profile of the soliton still is relatively close to the profile of a sine-Gordon kink, compare Fig. 10. As in this thesis the focus will be on $q < n|c_1|$, the shape of the solitons is expected to be very close to a sine-Gordon soliton. And as additionally the sine-Gordon part of the potential scales with $1-\overline{q}^2$ and the double sine-Gordon part with $\overline{q}^2$, especially for small q good agreement with the sine-Gordon predictions is expected.

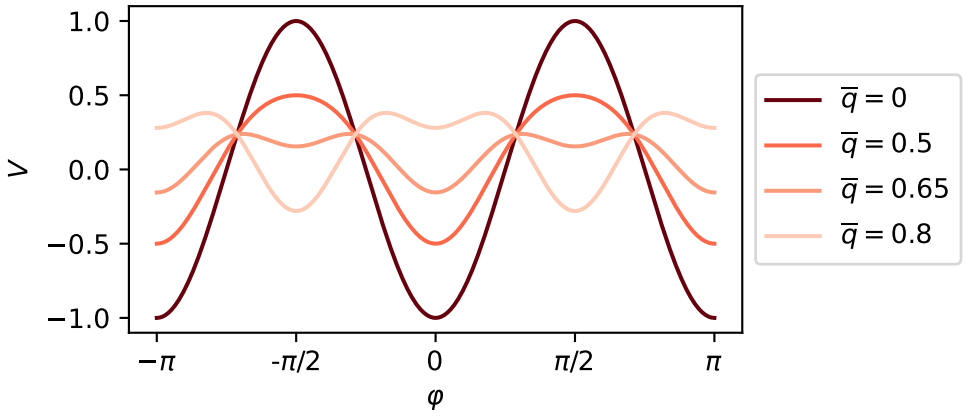

Figure 11: The dimensionless potential due to the Lagrangian of the LEEFT for $k \approx 0$ (see Eq. 29) for different values of $\overline{q}$. When comparing with Fig. 9 the potential leaves the range $0 \leq \eta < 1/4$ only for $\overline{q} \gtrsim 0.5$. For larger values the corresponding case is $\eta > 1/4$ and, as can be seen in the Lagrangian, at $q = \sqrt{2}$ the sign of the sine-Gordon part of the potential flips.

2.5 Numerical methods

To numerically solve the spin-1 mean-field GPE a split-step-Fourier method is used [33]. The simulations are performed on one spatial dimension consisting of N_x grid points, as the experiment also works in a quasi-1D regime. To work on the numerical grid in space and time the system first has to be discretised. When choosing the discretisation, it is important that the discrete steps are smaller than the healing length and the healing time of the condensate with the set parameters, respectively.

In the split-step Fourier approach, the time-evolution operator $\hat{U}(t) = \exp\left\{\left(-\mathrm{i}\hat{H}t\right)\right\}$ is the base of the time evolution. To efficiently compute this for the small time discrete time steps Δt, the Hamiltonian $\hat{H}$ is decomposed into a kinetic part $\hat{A}$ and a part including the non-linear terms $\hat{B}$, as $\hat{H} = \hat{A} + \hat{B}$. Then using the Baker-Campbell-Hausdorff formula and neglecting terms of order $\mathcal{O}(\Delta t^2)$, a timestep of the size Δt of the wavefunction ψ looks like

$$\psi(x, t + \Delta t) = \mathrm{e}^{-\mathrm{i}\hat{A}\Delta t}\mathrm{e}^{-\mathrm{i}\hat{B}\Delta t}\psi(x, t) + \mathcal{O}(\Delta t^2)\,, \tag{44}$$

so effectively the operator is split into two which are applied after each other. As in Fourier space the spatial derivative in the kinetic part $\hat{A}$ is proportional to k, for the step along $\exp\left\{\left(-\mathrm{i}\hat{A}\Delta t\right)\right\}$, first a fast fourier transform (FFT) is used to transform the state to momentum space, then the operator can be applied as a k-dependent factor and afterwards an inverse FFT is used to transform back to real space. For the propagation along $\exp\left\{\left(-\mathrm{i}\hat{B}\Delta t\right)\right\}$, here the step is further broken down into two separate steps. The first step are the diagonal parts of the underlying 3×3-matrix and the second step the off-diagonal parts, i.e. the spin-changing collisions, which is also explained more in-depth in [33]. In the actual propagation these steps are split up as a half-step of $\Delta t/2$ along the diagonal part, then a full step along the off-diagonal part, and finally another half-step along the diagonal part.

3 Single solitons

To further investigate the sine-Gordon solitons in the BEC, in this section, their general realisation and behaviour will first be described. For this first, the method used for preparing them in the experiment and the initial conditions used in the simulation are presented. Then their profile in different spin-1 observables is looked into and their behaviour under perturbations in the initial shape and background and under a change of the quadratic Zeeman shift is investigated.

3.1 Experimental phase imprinting scheme

When I started my master thesis in the team of the ^{87}Rb Spin-1 BEC experiment in the group of Markus Oberthaler, there already was ongoing experimental work regarding the realisation of solitons with a spinorphase profile similar to a sine-Gordon soliton profile. For this, a new phase imprinting scheme was developed, relying on the effective magnetic field induced by a locally applied laser beam, due to the vector Stark shift [1, 25, 34].

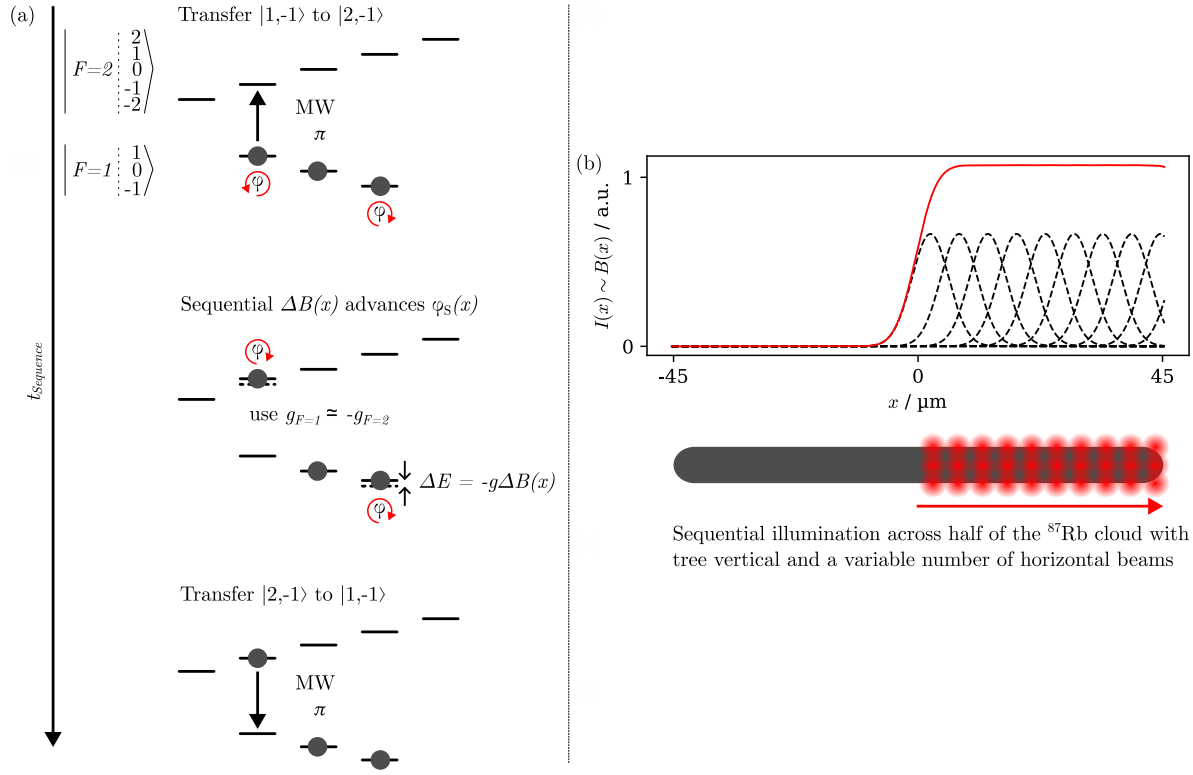

Figure 12: (a) The imprint scheme used to realise the sine-Gordon solitons in the experiment. First the atoms from $|1,-1\rangle$ are transferred to $|2,-1\rangle$, then the local magnetic field is applied and at last the atoms are transferred back to $F = 1$. (b) Desired imprint shapes can be realised by overlapping the Gaussian intensities in different ways. Figure taken and modified from [1].

After the atoms have been prepared in the easy-plane phase ground state for $q = 0$, i.e. with an elongated spin along F_x (see Eq. 14), a π-pulse from $F = 1$, $m_F = -1$ to $F = 2$, $m_F = -1$ is applied (see Fig. 12). As $g_{F=1} \approx -g_{F=2}$ (the difference is below the percent level), the phase of the atoms in $m_{F=1} = +1$ evolves in the same direction as the phase of the atoms in $m_{F=2} = -1$, when an external magnetic field is applied. The atoms in the $m_F = 0$ state experience no phase evolution due to the external field, leading to a change in spinorphase $\Delta\varphi_S$ (compare Eq. 2). This change depends on the additional local magnetic field $\Delta B(x)$ and the time τ it is applied as $\Delta\varphi_S \propto \Delta B(x)\tau$ [1, 34]. To vary the magnetic field locally, a steerable laser beam (via two acousto-optical-deflectors) on the tuneout wavelength of ^{87}Rb is used [35, 36]. Its intensity is proportional to the local effective magnetic field, as the linear Stark shift cancels out leaving only the effective magnetic field, due to the vector Stark shift. So, by changing the time, for which it is applied at each position, and the positions themselves any imprint consisting of different amplitude Gaussian profiles can be realised, as the intensity profile of the beam is always a Gaussian (see Fig. 12). After approximately 650µs in the $F = 2$, $m_F = -1$ state, the atoms are then sent back to $F = 1$, $m_F = -1$ by another MW π-pulse. The densities of the modes of the BEC now remain unchanged, but their relative phases have changed, leading to an imprint in the spinorphase.

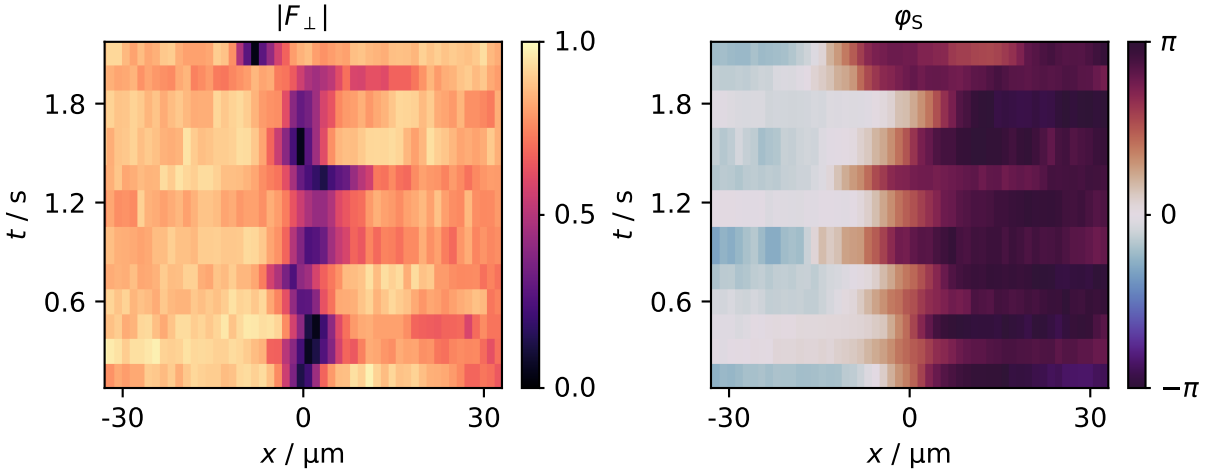

Figure 13: The sine-Gordon soliton observed in the ^{87}Rb-BEC in $|F_\perp|$ and φ_S at $q \approx 0$. This data was also used in [1].

Using this scheme, a profile similar to a sine-Gordon soliton in the spinorphase can be realised. It then turns out that the resulting phase profile actually behaves as a soliton, as it is stable in time (up to 15 s), as is shown in Fig. 13 and 14, and under collisions. During the time evolution in the experiment there is also no observable change in density due to the soliton. In the transversal spin $F_\perp$ the spinorphase imprint leads to a magnetic domain wall structure (so F_x and F_y both have a sign flip at the soliton position). In $|F_\perp|$ this is observed as a sharp dip at the soliton position (see Fig. 13 and 14). As half of

the BEC has to be illuminated for a single soliton imprint the experimental results were obtained in a small box trap.

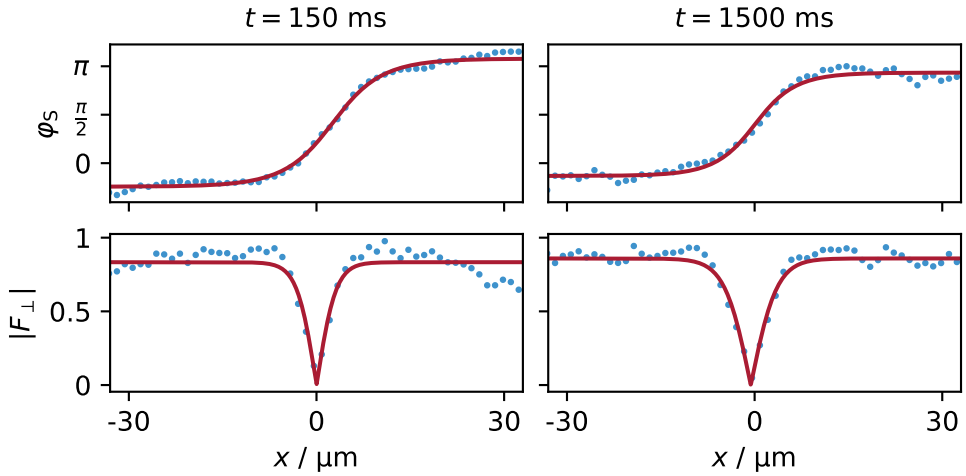

Figure 14: Slices of the soliton observed in the experiment at $q \approx 0$, as shown in Fig. 13. Additional to the data in red, fits of the expected functions in $|F_\perp|$ (see Eq. 48) and φ_S (see Eq. 51) are shown in blue.

3.2 Numeric starting conditions and width of soliton

In order to gain numerical insight into the behaviour of this type of soliton, we studied them using a 1D Spin-1 GPE simulation. In the following, the initial state preparation and the results of the real-time dynamical simulations are discussed. As the simulations were carried out in a system with periodic boundary conditions, the initial state always consisted of a kink and an antikink, so there is no phase jump at the border (other solutions satisfying the periodic boundary conditions, like e.g. two kinks, would also be possible). To make sure there is no interaction between the solitons, they are placed far from each other but such that their distance is not half the system size, so there is also no interaction cancelling out. As the general initial state of the BEC, the densities are prepared in the easy-plane ground state, either for q on the value also set for the propagation, to minimize the effect of background oscillations or, to get a better comparison to the experiment, for $q = 0$. In the following, these two different initial density preparations will be named matched background (if $q_{\text{init}} = q_{\text{propagation}}$ and unmatched background (for $q_{\text{init}} = 0$). In this section $q = 0.001n|c_1|$ (so $q \approx 0$) was chosen, where matched and unmatched background are up to very small deviations identical. This slight deviation from $q = 0$ was chosen, so the system is not at the critical point of the phase transition between easy-plane and easy-axis ferromagnet. To now realise a local spinorphase profile, a space-dependent phase is defined and then half of it is multiplied as a phase with a positive sign to the ± 1-modes and the other half of it with a negative sign to the 0-mode, like it

is done for solving the continuity equation in the supplementary material of [1].

The behaviour of the local phase imprint was interrogated for two different initial conditions: The first one aimed at replicating the experimental imprint scheme, by having the spinorphase (anti-)kink shaped like half of a Gaussian distribution, similar to what a Gaussian beam as the edge of the experimental imprint does. The rest of the spinorphase is then just flat. If this imprint is used, the soliton adapts to a sine-Gordon like shape in the spinorphase and oscillates around a certain width, as shown in Fig. 15.

The second is the theoretical shape of a sine-Gordon soliton in the spinorphase φ_{S}, which in the sine-Gordon equation as introduced above (Eq. 15) has $\beta = 2$, and at $t = 0$ can be written as:

$$\varphi_{\mathrm{S},\,K,\overline{K}}(x, t = 0) = \pm 2 \arctan\left(\exp\left(\frac{x - x_0}{\ell_{\mathrm{init}}}\right)\right) \tag{45}$$

This is used to find a solution with less additional perturbations present, i.e. no internal width oscillation. The only parameter to set in this solution is the width $\ell_{\mathrm{init}} = \frac{\sqrt{1-v^2}}{m}$ of the soliton, compare Eq. 16. In [16] the width of the Ferrodark solitons (FDS) is found to be

$$\ell = \frac{1}{\sqrt{2}}\xi_{\mathrm{s}} = \frac{\hbar}{\sqrt{4Mn|c_1|}}\,, \tag{46}$$

which is the first width that was tested in the simulations of the solitons. As a sine-Gordon (anti-)kink has no preferred width, a fixed width like ℓ would be a spin-1 effect.

As can be seen in Fig. 15, the solitons are stable for the width ℓ also used in [16]. Setting a different initial width leads to oscillations of the width approximately around the width ℓ. For small initial deviations from ℓ the mean of the oscillation $\langle\ell\rangle$ matches it quite well, see Fig. 16, while for larger initial deviations $\langle\ell\rangle$ becomes slightly larger than ℓ, as shown in Fig. 15. This is likely due to the width having a lower limit of 0, but no upper limit and therefore "compressing" the soliton is more energy intensive than extending it. The first peak of the width oscillation for the initial width of 0.5ℓ in Fig. 15 being higher than 1.5ℓ further supports this. Additionally, one can observe that the oscillation is damped, so the energy is likely dissipated via the radiation visible in Fig. 15. These internal modes of the soliton are a research topic in their own right and especially systematic studies of their structure for different q and with this on the transition from the sine-Gordon effective theory towards a double sine-Gordon effective theory would be very interesting. An implication this has for the dynamics of the solitons is that different to the full sine-Gordon model the width of the soliton is not freely adjustable to change the velocity of the soliton, but is given as a fixed value by the system. As it turns out this fixed width also has an advantage in the experiment, as it allows the effective comparison between experimental, numerical, and analytical data, due to its direct relation to the effective 1D spin healing-length ξ_{s}, which is also related to the spin healing time t_{s} and

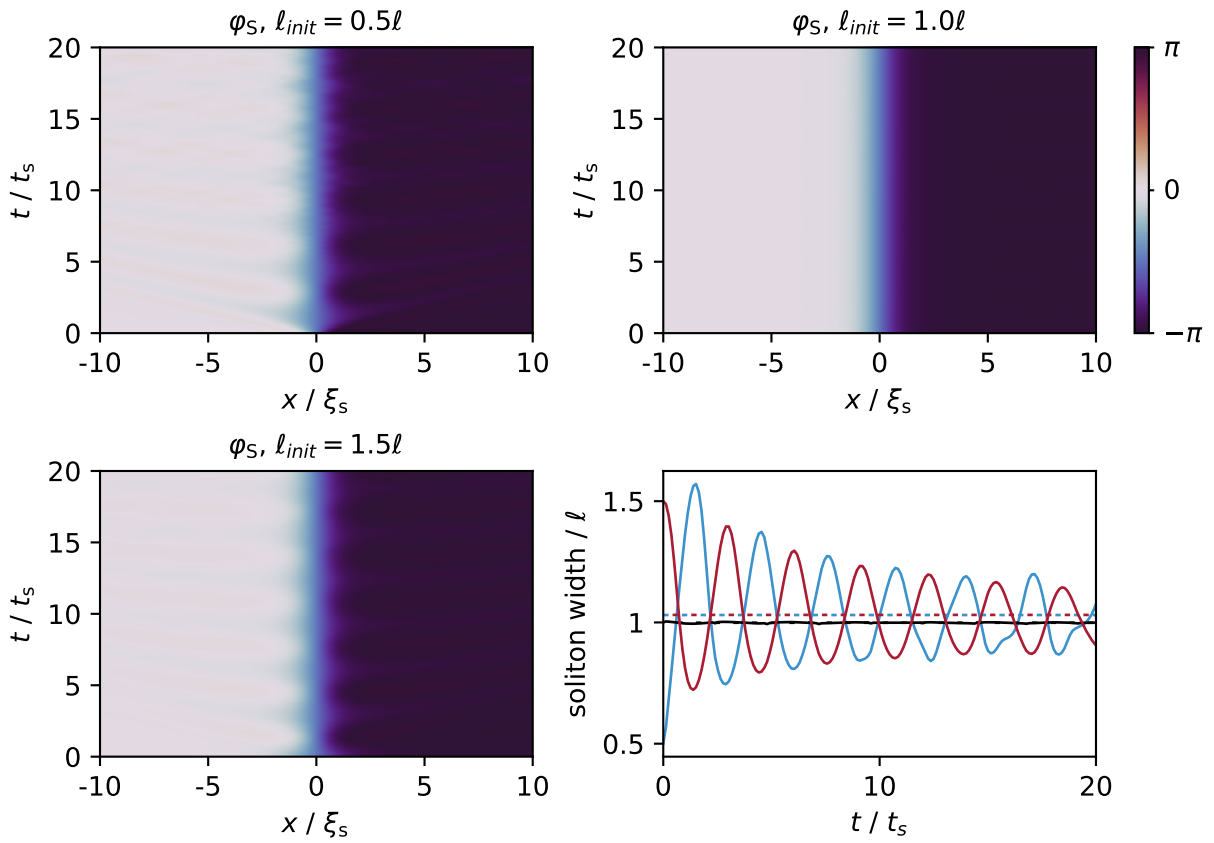

Figure 15: Simulations of the initial condition as defined in Eq. 45 with different values of ℓ_{init}. As can be seen in the bottom right the solution with $\ell_{\text{init}} = \ell$ (black) is stable, while $\ell_{\text{init}} = 0.5\ell$ (blue) and $\ell_{\text{init}} = 1.5\ell$ (red) oscillate around a mean value that is a bit larger than ℓ (dashed lines). This is due to the size of the deviations from ℓ. For small deviations, their mean matches ℓ more closely (compare Fig. 16).

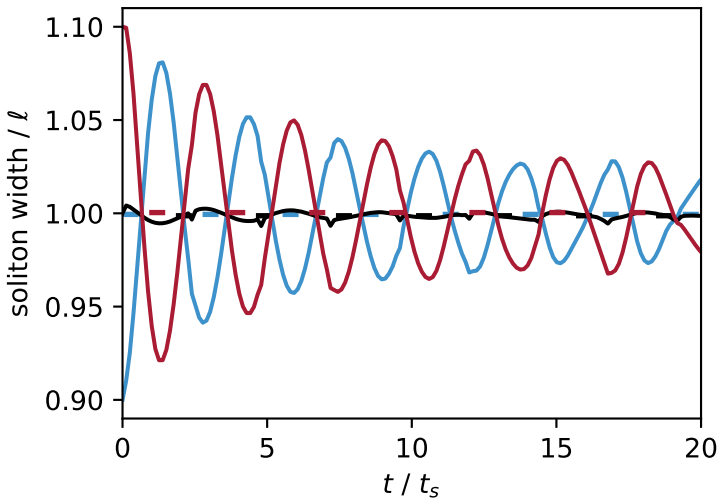

Figure 16: The width of the antikink for smaller initial deviations from ℓ, $\ell_{\text{init}} = 0.9\ell$ (blue) and $\ell_{\text{init}} = 1.1\ell$ (red), oscillates around a mean value (dashed lines) closer to ℓ, compared to Fig. 15. Here also the small changes in ℓ due to numerical inaccuracies, as well as small density fluctuations due to the imprint (see Fig. 21) are visible.

the 1D density of the BEC via physical constants. This means that by extracting the width of the solitons from the experiment one can obtain these values, which allows direct calculation of them from each measured soliton time-series, as opposed to more involved separate measurements only for obtaining these values, which especially for extracting the effective 1D-density is challenging.

3.3 Soliton evolution in different observables

As was shown above, in the spinorphase the soliton takes the shape of a sine-Gordon soliton. In spin-1 observables the spinorphase can be defined as the angle between F_x and Q_{yz} or F_y and Q_{xz}, where the distribution to each spin-nematic subspace depends on the Larmorphase, as defined in Eq. 8 and 9. While in the experiment small magnetic field fluctuations lead to a random de-phasing of the Larmorphase over time, in the simulation the solitons are prepared in such a way that the non-zero expectation values are in F_x and Q_{yz}, which also remains like this in time due to the stable Larmorphase, shown in Fig. 19, 17 and 18. The sign change in F_x, meaning that in F_x the soliton corresponds to a magnetic domain wall, directly hints towards a sharp kink visible in the Larmorphase. The change in F_x is realised through a rotation (the kink or antikink in spinorphase) on the equator of the spin-nematic sphere, meaning there is a bump or dip in Q_{yz} (see Fig. 17 and 18).

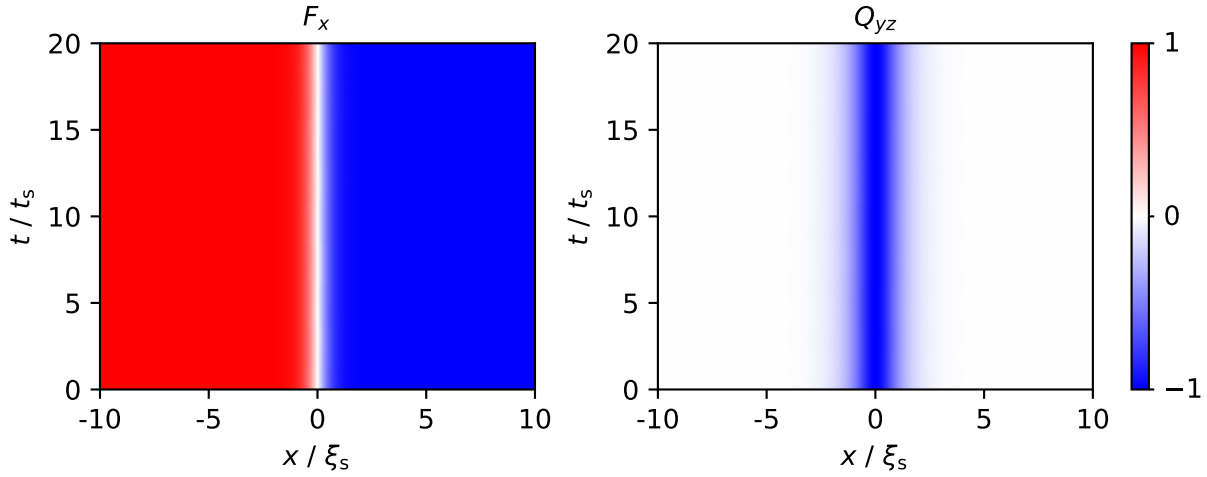

Figure 17: The magnetic domain wall in F_x at the soliton position and the corresponding dip in Q_{yz} to get an antikink going from $\varphi_S = 0$ to $\varphi_S = -\pi$.

To observe soliton dynamics in the experiment, a measurement different to the spinorphase is needed, when one wants to obtain data not requiring post-selection. For the spinorphase data (from an F_x-Q_{yz}-readout) this post-selection is needed, as the Larmorphase is random and can be at a value where the signal mostly is in F_y and Q_{xz} and all four observables cannot be read out at the same time. As an observable independent

of this the transversal spin $|F_\perp| = |F_x + \mathrm{i}F_y|$ is used and measured with an F_x-F_y readout [27]. In this observable, the soliton is equivalent to a dip, which is shown in Fig. 20 and similar to the spin profile of the recently introduced FDS [16] its shape follows:

$$|F_\perp|(x) = \left|\tanh\left(\frac{x - x_0}{\ell}\right)\right| \tag{47}$$

In addition to the spin observables the BEC can also feature local density excitations. In the simulation a small density dip at the position of the soliton emerges after a short evolution time, both for moving and non-moving solitons. This is also present in [16] for the FDS, but due to our significantly lower spin-spin interaction strength c_1 compared to the density-density interaction strength c_0, the density dip observed in the simulations is negligible, as seen in Fig. 21. As these simulations are done without added noise, the

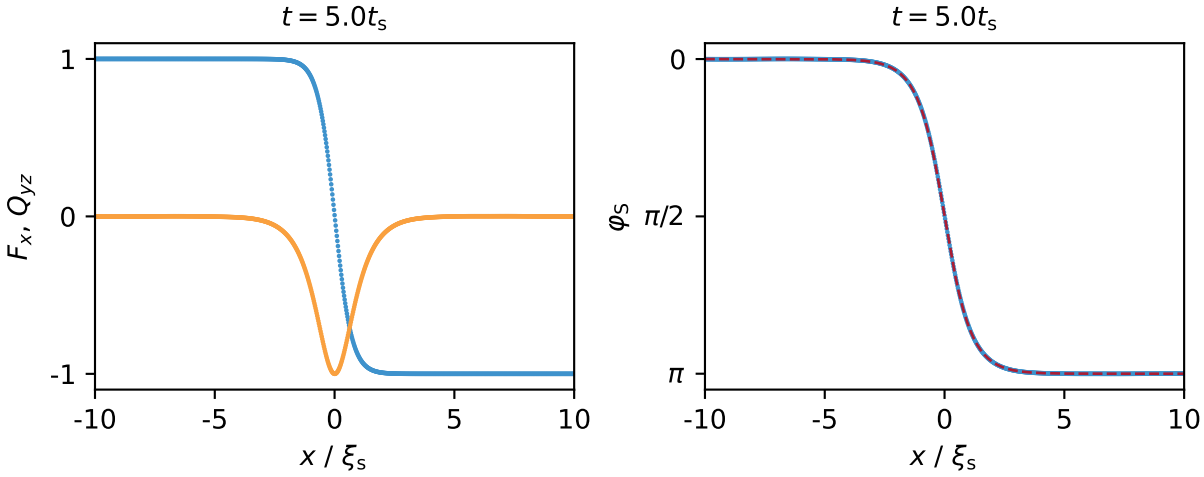

Figure 18: On the left F_x (blue) and Q_{yz} (orange) are shown in a single time slice and on the right the antikink in the spinorphase emerging from this (blue) with the analytical expectation for an antikink with $\ell_{\mathrm{init}} = \ell$ (see Eq. 45) (dashed red line) are plotted.

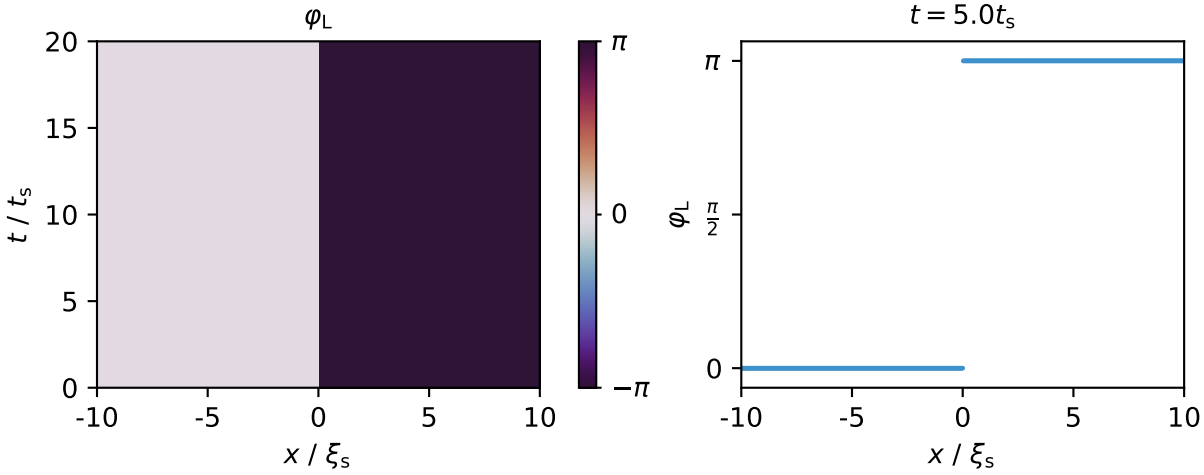

Figure 19: The sharp kink in the Larmorphase φ_{L} due to the sign change in F_x.

density packets radiating from the soliton when the dip forms are also visible, although smaller than 1% as well. In addition to the total density, there is also only negligible dynamics in the densities of the single modes. This can be seen from F_z remaining flat in the time evolution and Q_0 only showing fluctuations below the one percent level (see Fig. A3). To eliminate the radiation effects, I also tried different shapes of density dips as an initial condition, which remained unsuccessful. The formation of the soliton is again a topic in its own right with these results as first numerical indications.

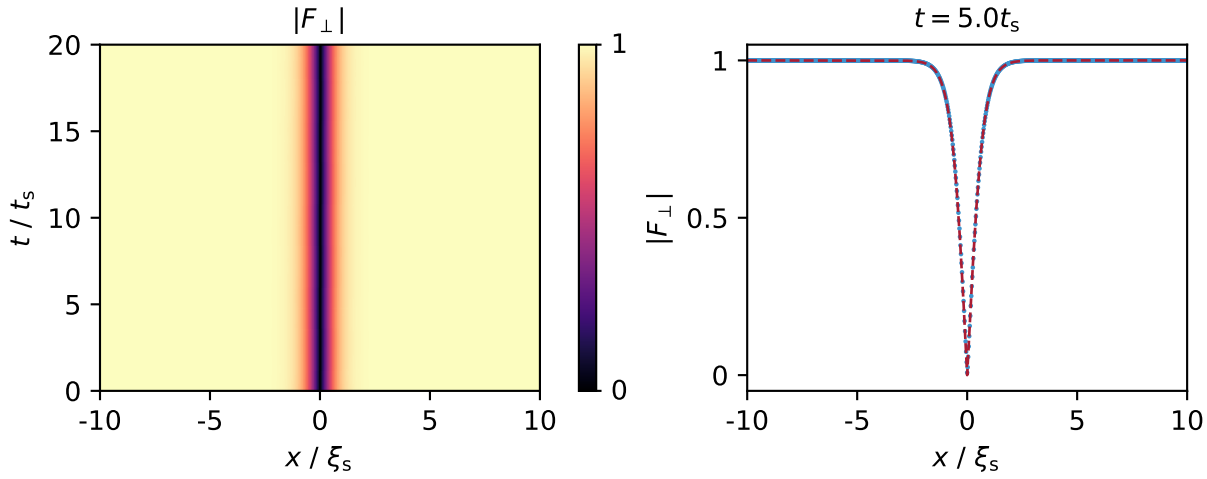

Figure 20: The dip on the soliton position in the transversal spin $|F_\perp|$, in the slice additional to the simulated data (blue) also the theoretical expectation, see Eq. 47, is shown as a dashed red line.

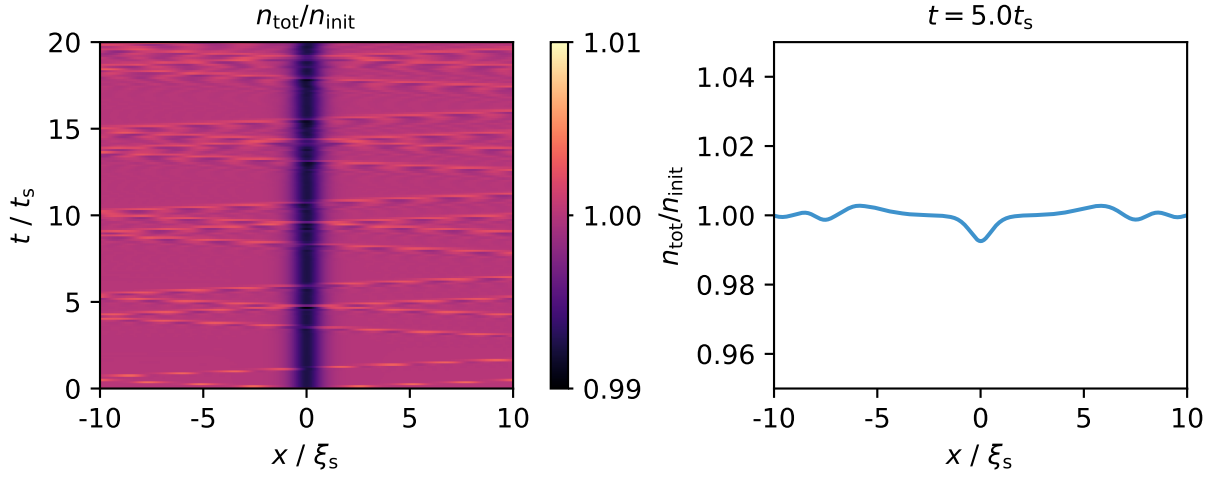

Figure 21: Total density over time for the soliton at $q \approx 0$, zoomed in to the percent level. The dip at the soliton position is clearly visible (especially in the slice). Additionally, the radiation of the forming of both dips (the antikink shown and the additional kink in the system) is visible, as fast-moving peaks.

3.4 Velocity dependence on the quadratic Zeeman shift

While the fixed width of the soliton in the spin-1 system ensures that the soliton imprinted is always the same object, it also leads to the soliton always having a fixed velocity in the (double) sine-Gordon model (see Eq. 15). This means that other ways to change the velocity of the soliton are needed.

It was observed that one way to control the velocity is changing the quadratic Zeeman shift q. In the experiment it was found that when comparing the velocities with the oscillations of the background value of $|F_\perp|$, $v = 0$ is the case for $q \approx 0$ and for larger q the velocity increases. Numerical simulations allow to check the velocity dependence of the solitons on q.

3.4.1 Unmatched background

This subsection focuses on simulations with an unmatched background and the initial condition close to an experimental imprint to get an estimate close to the experimental behaviour. The extraction of the soliton velocity from the data only requires a short time evolution, as the free trajectory of a single soliton is linear (see Fig. 22). Additionally, kink and antikink move with identical velocities in opposite directions, see Fig. A4. Due to this, in the following the data of the antikink will be presented, as for the kink only the sign in the velocity changes. To extract the velocity of the soliton from the data, $|F_\perp|$ is used as an observable. This not only allows for a reliable fit to the position via the dip, but in the experiment does not require post selection based on the random Larmorphase for later times. For this the fit function

$$|F_\perp|_{K,\overline{K}}(x) = \left| A \cdot \tanh\left(\frac{x - x_{\text{soliton}}}{\ell_{\text{fit}}}\right)\right| + B \tag{48}$$

is used. Here in the $|F_\perp|$-profile for $q \approx 0$ (Eq. 47) an amplitude A was added to account for different $|F_\perp|$-background lengths due to the different q and the resulting background oscillations and a possible offset B is allowed. The additional fit parameters are the position of the soliton x_0 and the width of the soliton ℓ_{fit}. By performing this fit in each time step, the trajectory $x_{\text{soliton}}(t)$ of the soliton can be extracted, to which a linear fit is then made, where the initial position x_0 and the velocity v are the fit parameters:

$$x_{\text{soliton}}(t) = v \cdot t - x_0 \tag{49}$$

When repeating this for multiple q, the resulting relation between v and q is approximately linear for small q and even seems to hold for $q < 0$, where the solitons remarkably also remain stable with linear velocity over q for small q, although the system is not in the easy-plane phase, as seen in Fig. 24. In order to extract the velocity dependence on q

a linear fit is performed in the linear range of the data seen in Fig. 24, i.e. $|q| \leq 0.4n|c_1|$, and the parameters extracted from the fit with $v(q) = \alpha_0 + \alpha_1 q$ are:

$$\begin{aligned} \alpha_0 &= (-0.0009 \pm 0.0011)\frac{\xi_\mathrm{s}}{t_\mathrm{s}} \\ \alpha_1 &= (1.093 \pm 0.004)\frac{\xi_\mathrm{s}}{t_\mathrm{s}}\frac{1}{n|c_1|} \end{aligned} \tag{50}$$

They confirm that for $q = 0$ the solitons have zero velocity.

From this data it is not directly obvious whether the deviations from the linearity,

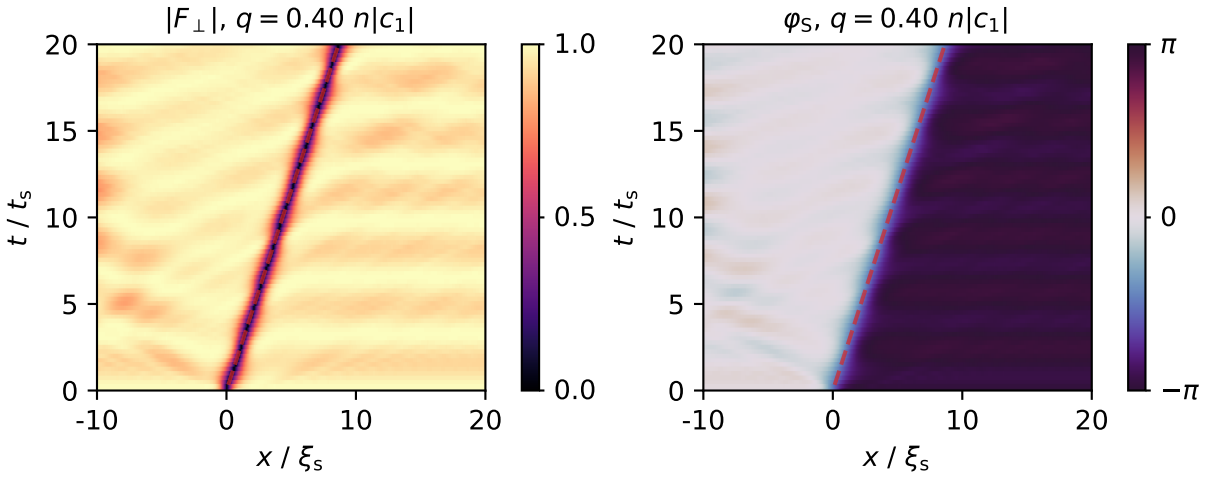

Figure 22: The moving soliton with an initial condition close to the experimental realisation and an unmatched background for $q = 0.30n|c_1|$. The background oscillation and the radiation from the adaption to the correct shape as well as the oscillation in width are clearly visible.

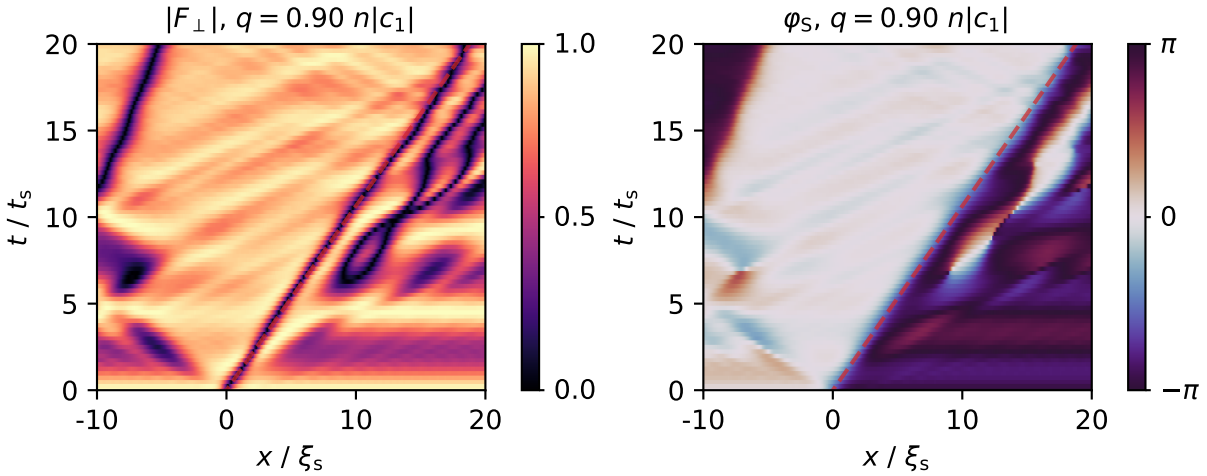

Figure 23: The soliton and strong background dynamics for a high q prepared with an unmatched background and an experiment-like initial condition. The additional antikink at the left is due to the radiation of both the imprinted kink- and antikink meeting at the boundary.

especially for $q \geq 0.8n|c_1|$, are actually expected behaviour from the solitons or due to strong background oscillations. These background oscillations lead to the emergence of defects in $|F_\perp|$ that look similar to the solitons and also seem to influence their dynamics, see Fig. 23. This also makes fits to the solitons significantly more difficult as the profile might jump to a neighbouring dip and the assumption of a linear trajectory is not fulfilled anymore, when a neighbouring dip is close. Furthermore, the width extracted from the different fits gets influenced by this, as even when confining the area over which the fit is made, the fit function might get influenced by additional local minima leading to the

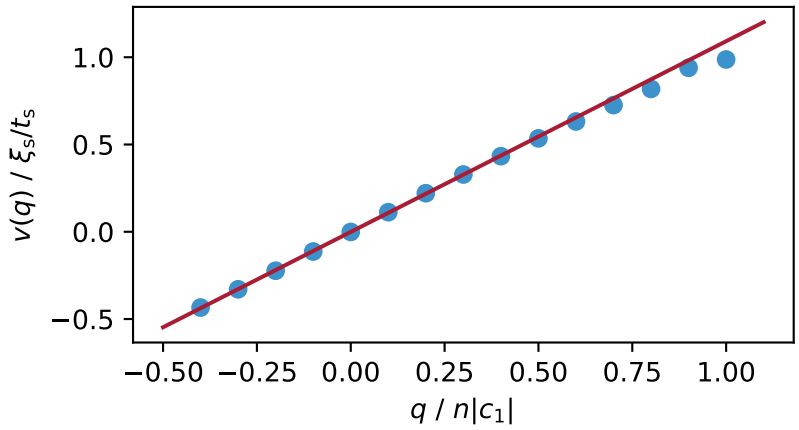

Figure 24: The velocity over q for an unmatched background and an experiment-like imprint, with a linear fit made to $|q| \leq 0.4n|c_1|$. The optimal fit parameters are given in Eq. 50 and noticeably the soliton is also stable for $q < 0$, with negative velocity.

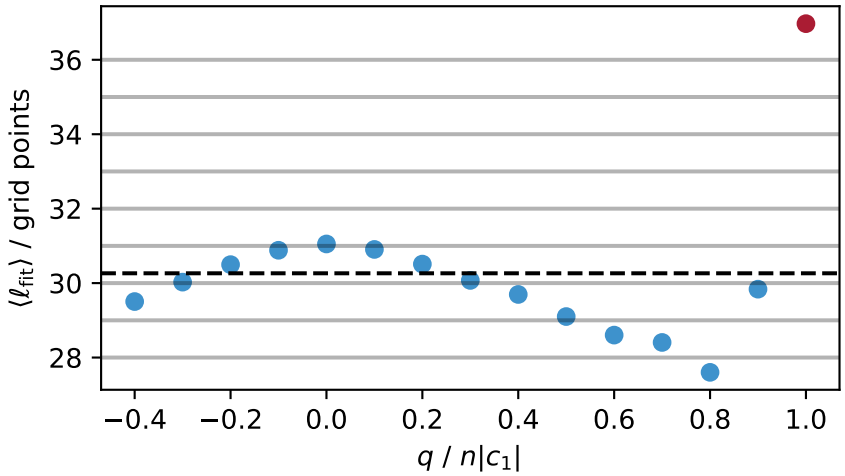

Figure 25: The mean width of the soliton over q extracted from the fits to the spinorphase profile. The dashed black line is the theoretically expected value of the width ℓ. The deviations for small q from this can be explained when comparing with Fig. 15, where for deviations of the initial width from ℓ the oscillation does not exactly have ℓ as its mean. For later deviations likely, the background deviations play a part, which for $q = 1.0n|c_1|$ (red point) even leads to the fit not being able to correctly extract the width anymore.

optimal background value of the fit changing from the actual background, which also can influence the extracted width. To get the width more precisely, a fit to the spinorphase turned out to be reliable, when already taking the knowledge of the position in each time step from the $|F_\perp|$-fit as the initial guess for the position parameter in the fit, as for this parameter $|F_\perp|$ is more reliable. This is due to the oscillations in φ_S just slightly changing the height of the soliton, while in $|F_\perp|$ the background height changes constantly due to the oscillation (see Fig. 23). The function used for the fit to the spinorphase is

$$\varphi_{\mathrm{S},K,\overline{K}}(x) = A \cdot \arctan\left(\exp\left(\frac{x - x_\mathrm{soliton}}{\ell_\mathrm{fit}}\right)\right) + B\,, \tag{51}$$

with amplitude A, offset B, initial position x_0 and width ℓ_fit as fit parameters. The extracted mean widths $\langle \ell_\mathrm{fit} \rangle$ are shown in Fig. 25. As one can see, for small absolute q the deviations are on the size of one grid point compared to the expected width ℓ. This is likely due to the same effect shown in Fig. 15, where an initial deviation from ℓ leads to a slightly different mean of the resulting width oscillation than ℓ. The strong deviation for $q = 1.0n|c_1|$ is due to the spinorphase fit not being able to extract the positions correctly anymore, also leading to incorrectly extracted widths.

3.4.2 Matched background

To asses the source of these deviations and see if the background and shape of the soliton also have an effect on the velocity for smaller q, the simulation is repeated with a matched background and the initial condition in the spinorphase as the stable profile for $q = 0$. As can be seen in Fig. 26, here the complete easy-plane range of q leads to stable soliton results, which follow a linear trajectory and are not influenced by background oscillations. This also results in a wider approximately linear range of the velocity over q, see Fig. 28. Remarkably stable solitons also exist far outside of the easy-plane, when preparing the state following the equation of the easy-plane ground state (Eq. 14) for the q outside of the easy-plane. The resulting velocities seem to behave like $v(-q) = -v(q)$ also outside of the linear region. Additionally, the extracted widths of the soliton, see Fig. 27, now lie much closer to the expected value of ℓ. For small q they match the expected value well and only starting from $q > 1.0n|c_1|$ the deviations become larger than one grid point. This could either be due to spin-1 effects or the effective model describing the system leaving the sine-Gordon limit of the double sine-Gordon model.

When assuming that the width stays constant, one can develop fit functions for $v(q)$ from the effective theory. In units of $\overline{x}$, as introduced in Eq. 24, the width obtained from the fit corresponds to $\overline{\ell} = \frac{1}{\sqrt{2}}$. Assuming the shape of the soliton follows Eq. 16 for q in the sine-Gordon limit, the mass of the sine-Gordon model m, the Lorentz-boost $\frac{1}{\sqrt{1-v^2}}$ and for the case $k \approx 0$ also the additional transformation of the space coordinate $\tilde{x}/\overline{x}$, see

Eq. 35, have to give the inverse of this constant width:

$$\frac{1}{\bar{\ell}} = \sqrt{2} = \frac{m}{\sqrt{1-v^2}} \cdot \frac{\tilde{x}}{\bar{x}} \tag{52}$$

This can now be rearranged to obtain a relation for the dimensionless velocity dependence on q in the sine-Gordon limit:

$$v = \sqrt{1 - \frac{m^2}{2}\left(\frac{\tilde{x}}{\bar{x}}\right)^2} \tag{53}$$

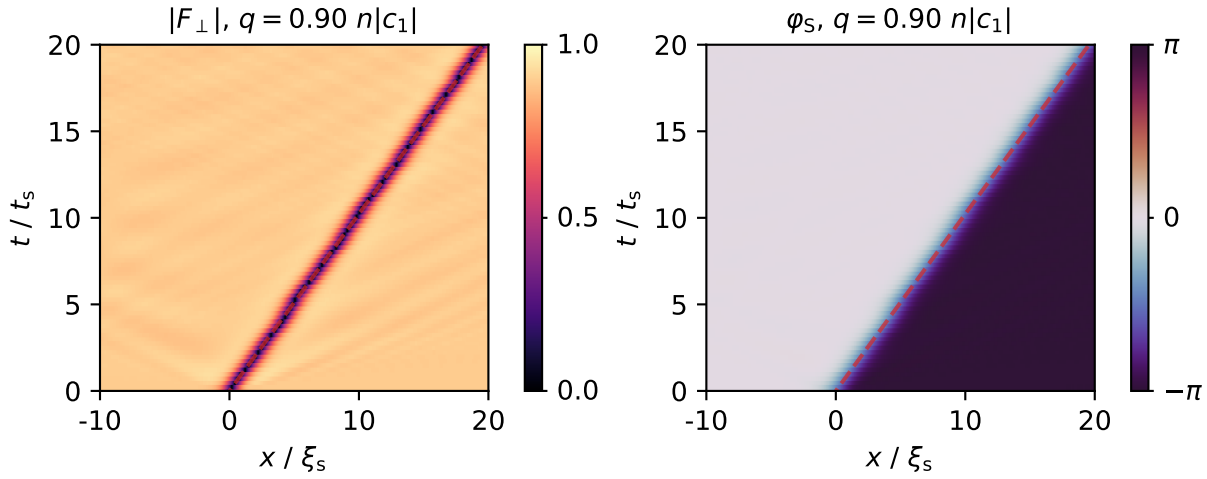

Figure 26: The moving soliton with a matched background at a higher q. When comparing with Fig. 23, the strong difference in stability is obvious. With a matched background for all set q ($q \leq 1.9n|c_1|$) the single solitons follow stable trajectories and there is no strong radiation in the spinorphase or $|F_\perp|$.

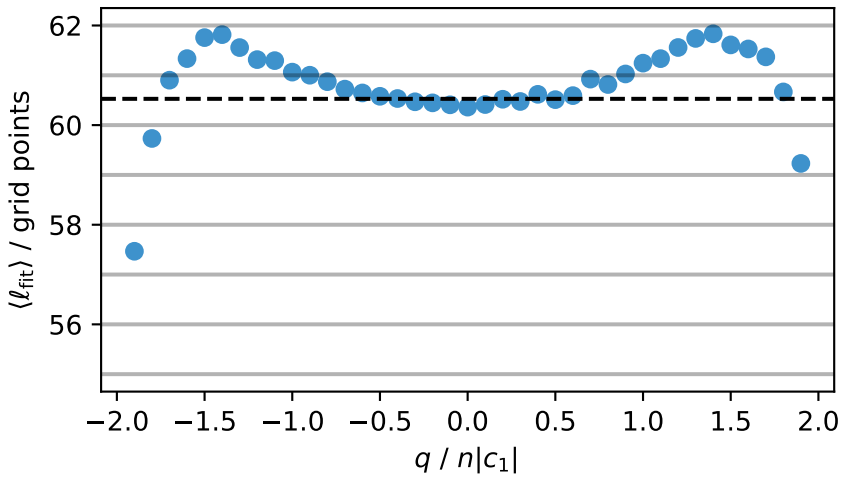

Figure 27: Mean width $\langle \ell_{\text{fit}} \rangle$ of the soliton in numeric grid points as obtained from fits to the simulation for different q. Up until $|q| = 1.0n|c_1|$ the width of the soliton does not deviate more than one grid point from the theoretical expected width ℓ, shown as the dashed black line.

In the physical coordinates one now gets:

$$v_{\text{obs}} = \frac{\overline{x}}{\tilde{x}}\frac{x}{\overline{x}}\frac{\overline{t}}{t}v = \frac{\hbar k_{\xi_s}}{2M}\sqrt{\left(\frac{\overline{x}}{\tilde{x}}\right)^2 - \frac{m^2}{2}} \tag{54}$$

For $k \approx k_{\xi_s}$, no additional space transform is needed, so $\frac{\tilde{x}}{\overline{x}} = 1$, leading to the two different velocity relations:

$$v_{\text{obs}} = \frac{\hbar k_{\xi_s}}{2M}\sqrt{2(1-\overline{q}^2) - 2(1-2\overline{q}^2)} = \frac{\hbar k_{\xi_s}}{\sqrt{2}M}\overline{q} = \frac{\hbar}{\ell}q\,, \quad \text{for } k \approx 0 \tag{55}$$

$$v_{\text{obs}} = \frac{\hbar k_{\xi_s}}{2M}\sqrt{1 - \frac{4}{1-\overline{q}^2}\overline{A}}\,, \quad \text{for } k \approx k_{\xi_s} \tag{56}$$

The same result as for $k \approx 0$ is obtained by a derivation of the soliton velocity from the spin-1 continuity equation [1]. In the sine-Gordon limit this now motivates two different fit functions. The case $k \approx 0$ motivates to fit a linear function and the case of $k \approx k_{\xi_s}$ motivates a fit function of the shape

$$\begin{aligned} v_{\text{obs}} &= \text{sgn}(\overline{q})\sqrt{a_0 + a_1\overline{q}^2 + a_2\overline{q}^2(1-\overline{q}^2) + a_3\overline{q}^2(1-\overline{q}^2)^2} \\ &= \text{sgn}(\overline{q})\sqrt{b_0 + b_1\overline{q}^2 + b_2\overline{q}^4 + b_3\overline{q}^6}\,, \end{aligned} \tag{57}$$

when plugging in $\overline{A}$ and instead of constant prefactors using flexible fit parameters a_i. This is then rewritten as a polynom with the same orders of q in the square-root, as this performs significantly better for fitting and the parameters a_i can also be obtained from b_i. The optimal parameters obtained from the fit are shown in Table 1 together with the a_i calculated from these.

i	b_i	$a_i(b_i)$	a_i
0	0.0019 ± 0.0022	b_0	0.0019 ± 0.0022
1	4.80 ± 0.04	$b_1 + b_2 + b_3$	2.79 ± 0.23
2	0.023 ± 0.167	$-b_2 - 2b_3$	4.04 ± 0.34
3	-2.03 ± 0.15	b_3	-2.03 ± 0.15

Table 1: The optimal parameters b_i found when fitting the function shown in Eq. 57 to the data shown in Fig. 28. From these the parameters used in the effective theory a_i are calculated by the given formulas.

As before, there is now constant offset found by the fit and the $\overline{q}^2$ term below the square-root dominates for small $\overline{q}$. For larger $\overline{q}$ the fourth order of $\overline{q}$ is also approximately not contributing and only the sixth order contributes again. This calculated values for a_i do not match the prefactors given in $1 - \frac{4}{1-\overline{q}^2}\overline{A} = 2\overline{q}^2 - 4\overline{q}^2(1-\overline{q}^2) - 8\overline{q}^2(1-\overline{q}^2)^2$ even within 3 standard deviations. But while giving a good fit function to the velocities this would also not be expected, as for larger q, where the higher orders only get relevant

in the fit, the assumption of a constant width is broken, and the system is not in the sine-Gordon limit of the effective theory anymore.

In the case $k \approx 0$, flexible parameters in front of each order of $\overline{q}^2$ in the square-root give $v_{obs} = \sqrt{a_0 + a_1 \overline{q}^2}$, which, when fitted, gives $a_0 = (0.037 \pm 0.022) \frac{\xi_s^2}{t_s^2} \approx 0$ and therefore is nearly equivalent to a linear fit. When using a linear fit for small $q \leq 0.8n|c_1|$, similar to the unmatched background and also using q and not $\overline{q}$ (as above), one gets:

$$\begin{aligned} \alpha_0 &= (0.0006 \pm 0.0007) \frac{\xi_s}{t_s} \\ \alpha_1 &= (1.0980 \pm 0.0015) \frac{\xi_s}{t_s} \frac{1}{n|c_1|} \end{aligned} \tag{58}$$

These fit values match those found for the unmatched background with the experiment-like initial starting condition within one standard deviation, see Eq. 50. So, for small absolute $|q| \leq 0.40n|c_1|$, it can be stated that the oscillating background and small deviations of the initial condition from the perfect shape of the soliton do not have an effect on the dynamics of a single soliton, but for larger values of q the background oscillations start to have an effect.

The linear behaviour for small q can now also be compared to data taken in the experiment, shown in Fig. 29. For the experimental data $v(q = 0) = 0$ was taken as given to find $q = 0$ from the linear fit to the velocities. Similar to the data above, also in the experiment for $q < 0$ the soliton is stable and moves in the opposite direction. To compare the two different unit systems the mean width in the experiment of $\langle \ell_{\text{fit}} \rangle = 5.02\mu\text{m}$ can be used to obtain ξ_s, t_s and $n|c_1|$ in SI-units. This can then be used to express the fit

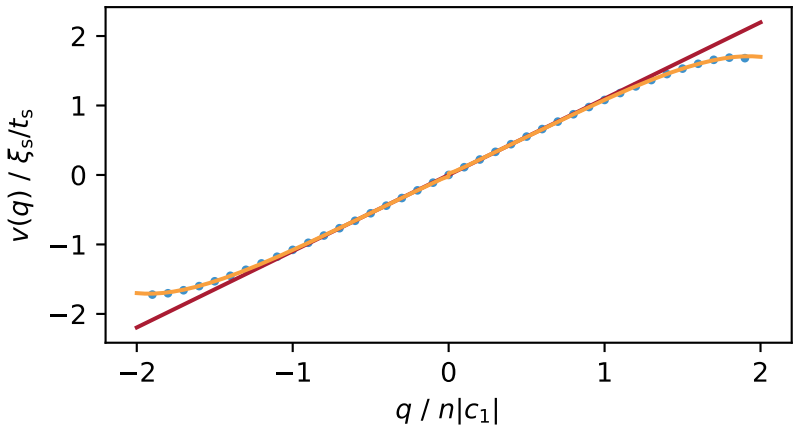

Figure 28: The extracted velocities for different q, with a matched background and the correct imprint shape in φ_S. The linear fit (red) was made to the data points with $|q| \leq 0.8n|c_1|$ while the fit with parameters b_i, as shown in Eq. 57, (orange) was made to the complete dataset. The optimal parameters found by this fit are shown in Table 1.

parameter α_1 found for the unmatched background data in SI-units, leading to:

$$\alpha_{1,\mathrm{sim}} = (48.79 \pm 0.18)\mu\mathrm{m\,s^{-1}\,Hz^{-1}} \tag{59}$$

This matches the experimental fit value $c_{1,\mathrm{exp}} = (41.45 \pm 3.15)\mu\mathrm{m\,s^{-1}\,Hz^{-1}}$ within 3 standard deviations. Some deviation to a larger value in the simulation is also expected here as the mean width $\langle \ell_{\mathrm{fit}} \rangle$, similar to Fig. 15, very likely overestimates the width ℓ leading to a larger ξ_{s} in SI-units. Additionally, values of q, which were not used for the linear fit in the unmatched background data anymore, were used here. When excluding values with $|q| > 0.4n|c_1|$, one obtains

$$\alpha_{1,\mathrm{exp}} = (45.47 \pm 3.92)\mu\mathrm{m\,s^{-1}\,Hz^{-1}}\,, \tag{60}$$

which is much closer to the value found in the simulation.

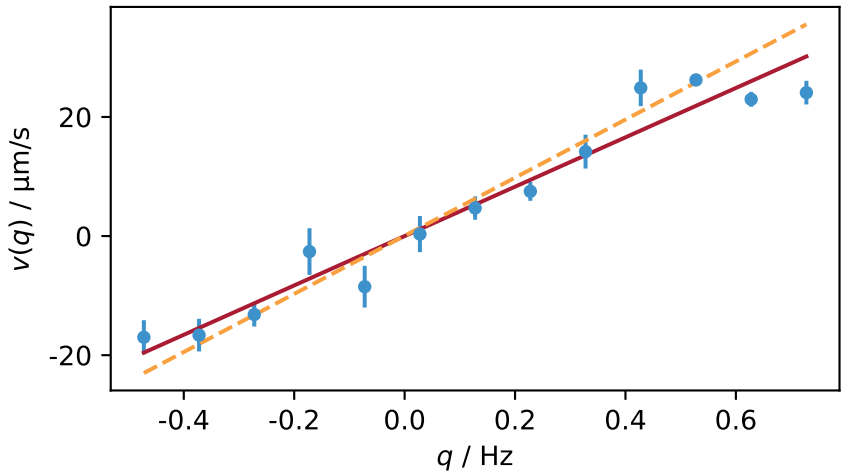

Figure 29: Soliton velocities in the experiment over q, as also shown in [1]. The red line is a fit to the experimental $|F_\perp|$-data. Its offset is used to determine $q = 0$ and the found slope is $\alpha_{1,\mathrm{exp}} = (41.45 \pm 3.15)\mu\mathrm{m\,s^{-1}\,Hz^{-1}}$. The dashed orange line is the function found from a fit to the simulated data with the unmatched background. To get to SI-units from the fit parameters found in the simulation, the mean width in the experiment of $\langle \ell_{\mathrm{fit}} \rangle = 5.02\mu\mathrm{m}$ was used.

3.5 Lifetime

It was also found that the solitons described here decay for 10 to $15 \cdot 2\pi t_{\mathrm{s}}$ in the simulations. This is expected, as the solitons live in a spin-1 BEC and are also simulated for a spin-1 system, both with $c_1 \sim -\frac{c_0}{200}$, which is fully described by non-integrable models. For the dark-antidark-dark- (DAAD) and antidark-dark-antidark-solitons (ADDAD), which, as will be shown in Sec. 5, are closely related to the solitons described here, thorough

studies regarding their decay mode have already been made in [15]. The solitons described here decay due to small local differences of n_{+1} and n_{-1} emerging directly next to the soliton position. These differences then lead to a runaway effect as the $+1$- and -1-modes are immiscible, leading to a local F_z expectation value, as shown in Fig. 30. As already mentioned, this is very similar to the decay of the DAAD- and ADDAD-solitons in [15] and somewhat expected, which is why no further studies regarding the decay were made here.

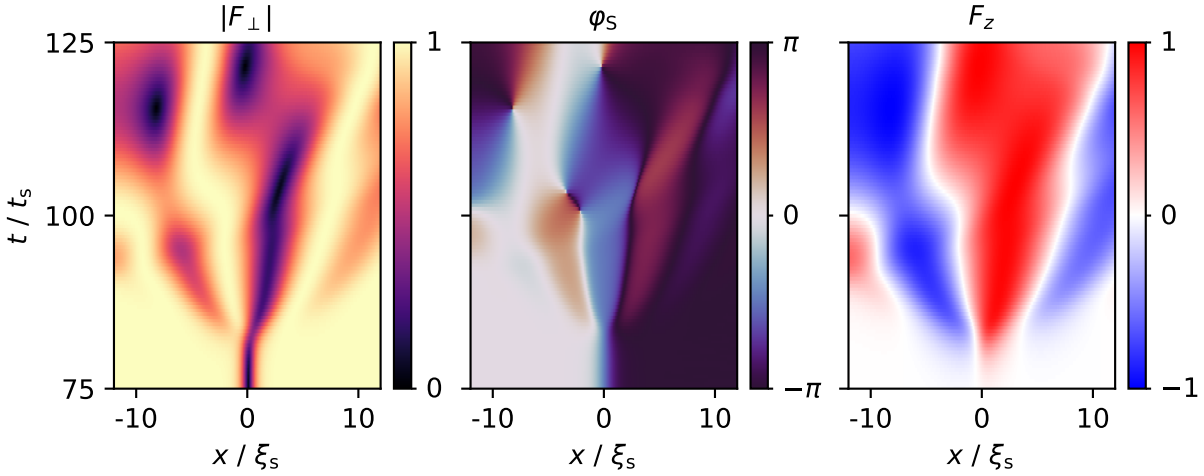

Figure 30: The decay of a soliton simulated with the correct initial width at $q = 0.001n|c_1|$. While in the beginning there are no obvious signs of the decay in $|F_\perp|$ and φ_S, the emerging expectation values in F_z at the soliton position are already visible.

4 Breather

For $q = 0$ the effective theory reduces to a pure sine-Gordon model. The previous results hint towards the spin-1 system coming close to this integrable theory in this case, which will be tested with other unique solutions of the sine-Gordon model, i.e. the breather, in the following. These simulations were again performed at $q = 0.001n|c_1|$ so that the system is not at the critical point of exactly $q = 0$, but the effective model describing it should still be very close to a sine-Gordon model. As a starting condition for this, first a starting condition based on Eq. 18 was used. The width of this imprint was adapted such that it is the same as the soliton width ℓ, leading to the following shape:

$$\varphi_{\mathrm{s,br}} = 2 \arctan\left(\tan(\mu) \frac{\sin(t_0 \cos(\mu))}{\cosh\left(\frac{x-x_0}{\ell} \sin(\mu)\right)}\right) \tag{61}$$

This is a similar parametrisation as in Eq. 18 only now using the amplitude μ instead of a frequency, which is the more natural parameter for an initial condition, where the resulting frequency is unknown. It is important to note that μ is half the amplitude at the maximum of the breather in the spinorphase. For different μ this was simulated, to check whether all imprints are stable and behave like sine-Gordon breathers.

The first result is that these imprints are indeed stable and show breathing, although with deviations from sine-Gordon breathers, in the spinor phase φ_{S}, shown in Fig. 31. For amplitudes of $\mu > \frac{\pi}{2}$ they oscillate, in contrast to the sine-Gordon breathers, around the potential minimum at $\varphi_{\mathrm{S}} = \pm\pi$ instead of the background value $\varphi_{\mathrm{S}} = 0$. This can be understood when looking not only at φ_{S}, but also at the observables F_x, Q_{yz} and Q_0, which make up the nematic sphere, see Fig. 32 and 33. In F_x the breather keeps a constant shape consisting of a dip, the depth of which depends on the breather amplitude μ. This means in $|F_\perp|$ there are either one or two dips present, depending on the initial amplitude, which is shown in Fig. A7. In Q_{yz} and Q_0 an oscillation is visible shifted by a phase of $\frac{\pi}{2}$ between the two observables. On the nematic sphere this observation corresponds to a rotation of a line on the sphere's surface around the F_x-axis, as shown in Fig. 34. The initial amplitude of the breather changes the length of the line on the surface of the sphere and the slower frequency of the rotation for a higher amplitude can also directly be seen. As for amplitudes $\mu > \frac{\pi}{2}$ F_x changes sign in the middle of the breather, this leads to a different minimum around which the oscillation in the spinorphase is performed at this point, as the angle φ_{S} between a negative F_x and any Q_{yz} is always in $[\pi/2, 3\pi/2]$. As Q_{yz} has the same sign for the whole breather at a single point in time, the sign change in F_x leads to a jump in spinorphase for $Q_{yz} = 0$.

From this data the frequency of the oscillation can also be extracted to compare it with the sine-Gordon relation for the imprint made (Eq. 19). A particular easy way to

do this is to calculate the angle θ between Q_{yz} and Q_0 at the middle of the breather as the angle at which the breather is tilted on the sphere. When the resulting values are unwrapped numerically, one gets a linear behaviour in time, as shown in Fig. 35. To this a linear fit can then be performed, the slope of which is the frequency ω of the rotation of the breather on the sphere, corresponding to its frequency in the spinorphase. As seen in Fig. 36, this gives rise to a frequency amplitude relation different from the prediction Eq. 19 for sine-Gordon breathers, but still in a cosine shape. This cosine shape can then also be fitted as $\omega(\mu) = A\cos(\alpha_0\mu + \alpha_1) + B$ leading to:

$$\begin{aligned} A &= (1.0008 \pm 0.0004)\frac{1}{t_\mathrm{s}} \\ \alpha_0 &= 2.0049 \pm 0.0013 \\ \alpha_1 &= 0.0024 \pm 0.0013 \\ B &= (1.0004 \pm 0.0003)\frac{1}{t_\mathrm{s}} \end{aligned} \tag{62}$$

Compared to the expectation of $\omega = m\cos\mu$ (from Eq. 19 with $\mu = A/2$) for the sine-

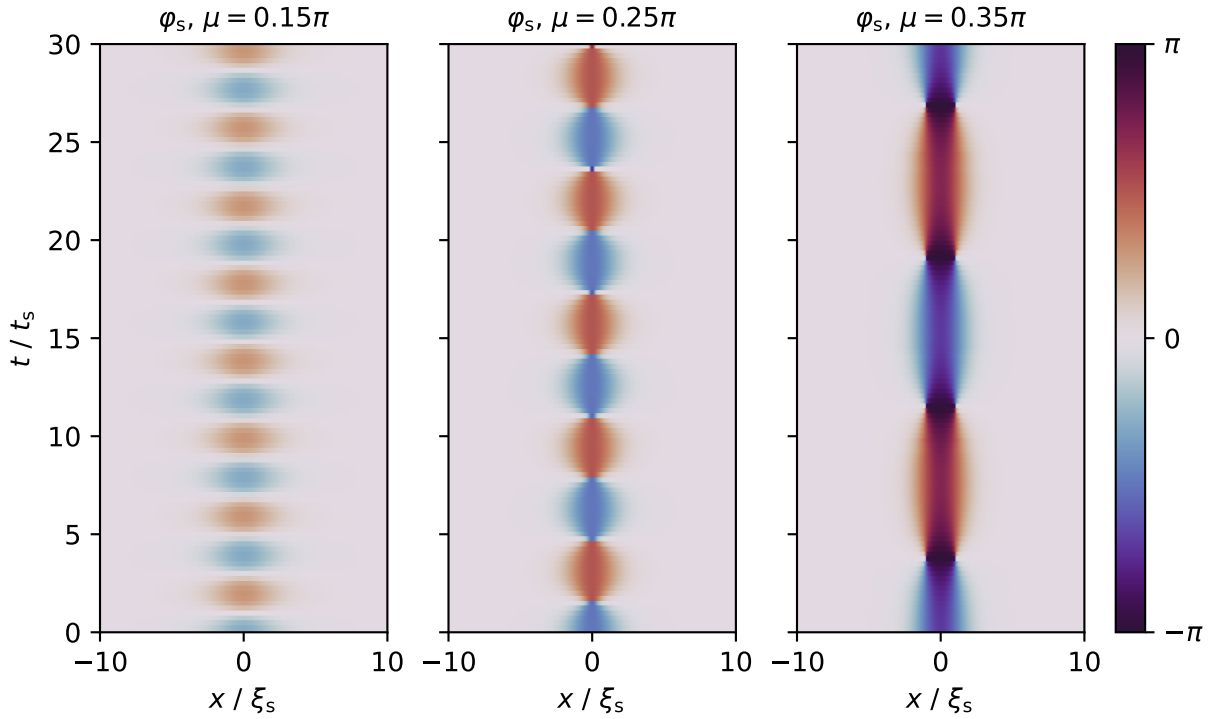

Figure 31: Result of the spin-1 simulation of the sine-Gordon breather profile as the initial condition, as defined in Eq. 61, in the spinorphase over time for different initial amplitudes μ. While for small μ the breather looks similar to the sine-Gordon breather (left), for large μ the middle of the breather oscillates not around the background but around the next minimum, which will be discussed later in detail. As is easily seen, the breather frequency gets smaller with higher amplitude.

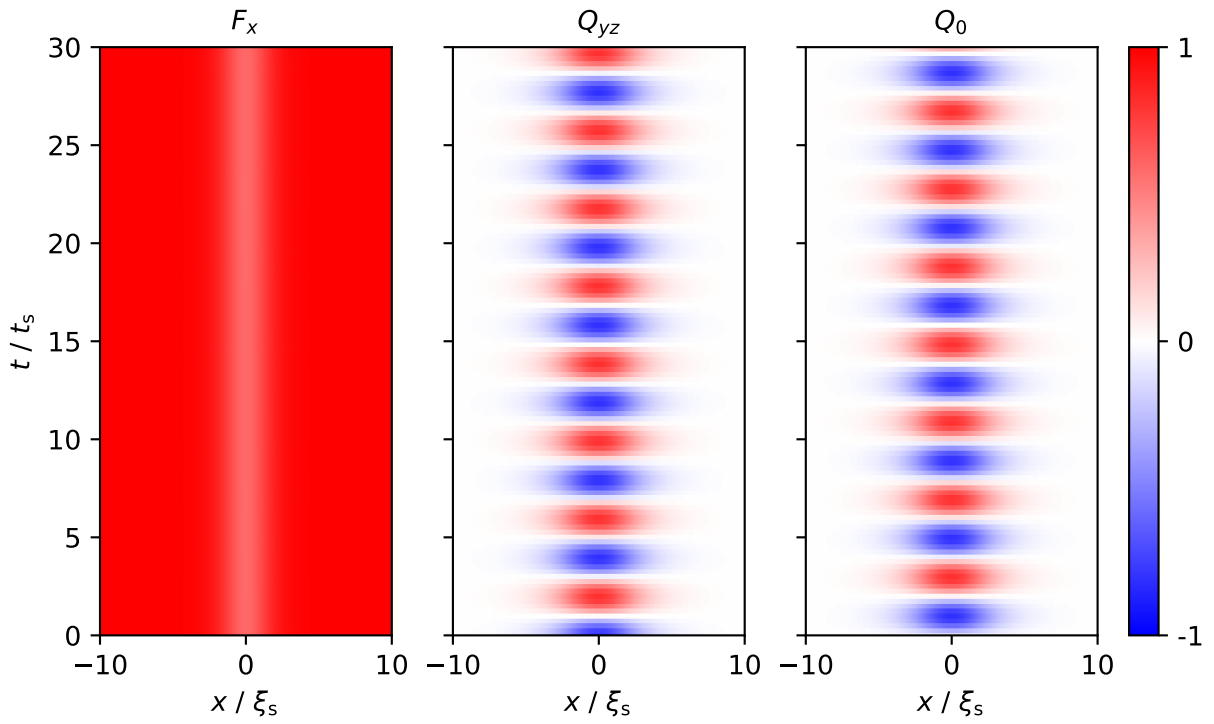

Figure 32: The breather in the observables making up the nematic sphere for a small initial amplitude of $\mu = 0.15\pi$. In F_x there is a stable dip (completely in the positive, so also one dip in $|F_\perp|$), and Q_{yz} and Q_0 oscillate with a $\pi/2$ phase.

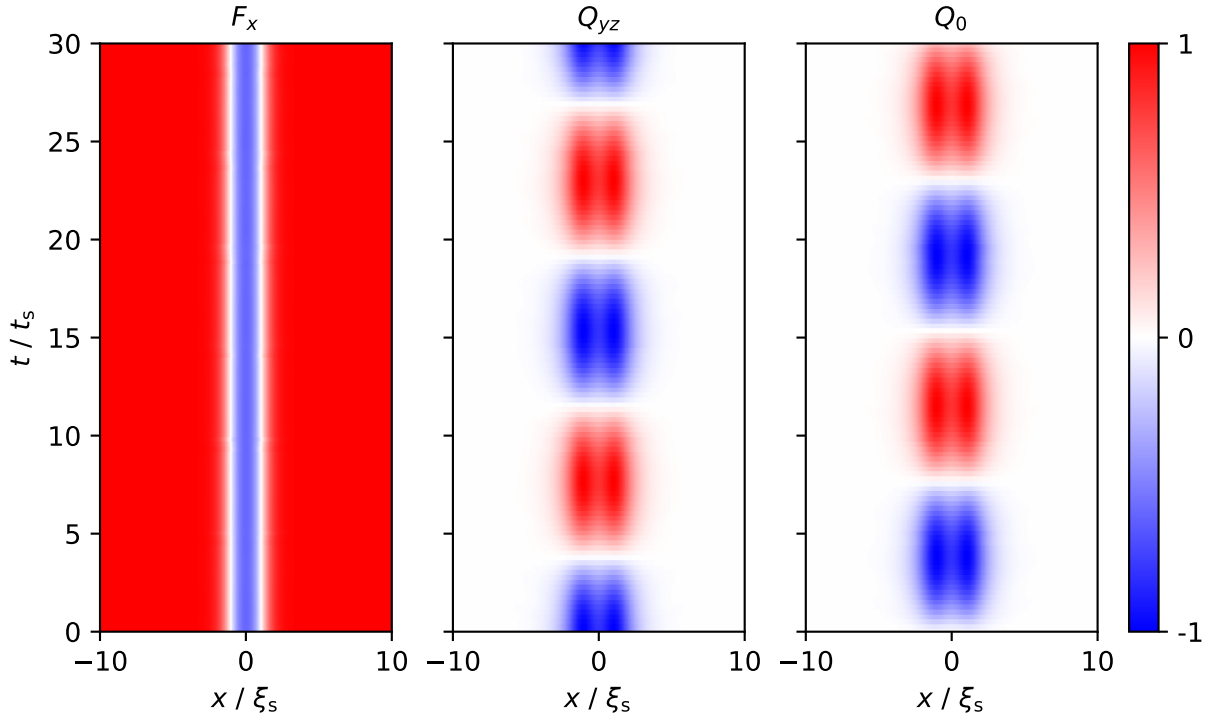

Figure 33: For a large initial amplitude of $\mu = 0.35\pi$, the dip in F_x extends to negative values (leading to two dips in $|F_\perp|$). Q_{yz} and Q_0 both still oscillate with a phase of $\pi/2$, but they now also are made up by two dips/peaks.

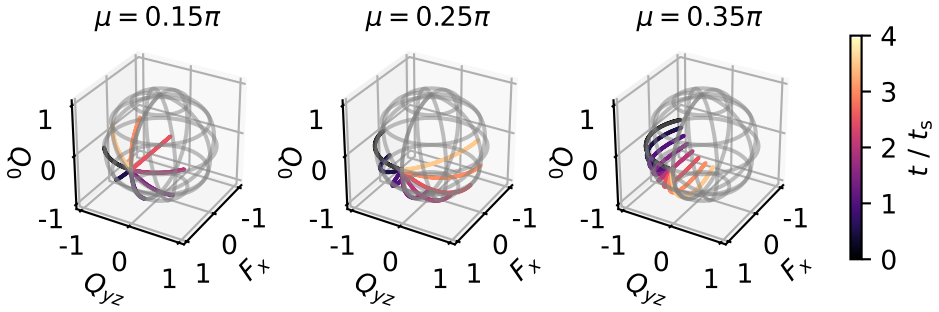

Figure 34: All spatial points of the breather plotted on the nematic sphere for different times (dark corresponds to early, light to later) and different imprint depths. As one can see the breather in space corresponds to a line on the surface of the sphere that rotates around the F_x-axis with the frequency of the breather oscillation, so for a imprint with higher amplitude (here longer line) the rotation gets slower, which can also be seen here as the time interval plotted is the same for all three cases.

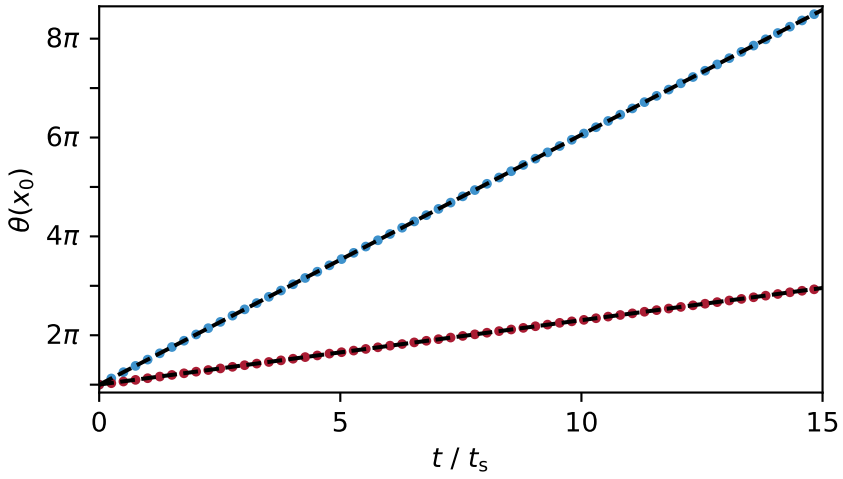

Figure 35: The linear evolution of the tilt angle over time for $\mu = 0.15\pi$ (blue) and $\mu = 0.35\pi$ (red). The black dashed lines are the linear fits made to these which prove an easy and efficient way of extracting the frequency of the breather compared to fits to the oscillation in φ_S. This fit leads to the same results (see Fig. A6), but is very sensitive to initial fit parameters, which is also the case for the oscillation in Q_0 and Q_{yz}. Additionally, this allows to fit oscillations even if a complete period is not captured.

Gordon model, this is approximately $\omega = 2\cos^2\mu$, so a different, although related relation. Although the factor 2 would actually match the prediction of the sine-Gordon mass m for $k \approx 0$, this cannot be compared because of the difference in the observed shape of the relation. As the effective theory was developed for small perturbations around the potential minima, a difference to the sine-Gordon model of the breather is expected, as its dynamics are mostly located between the minima, maximally violating this assumption.

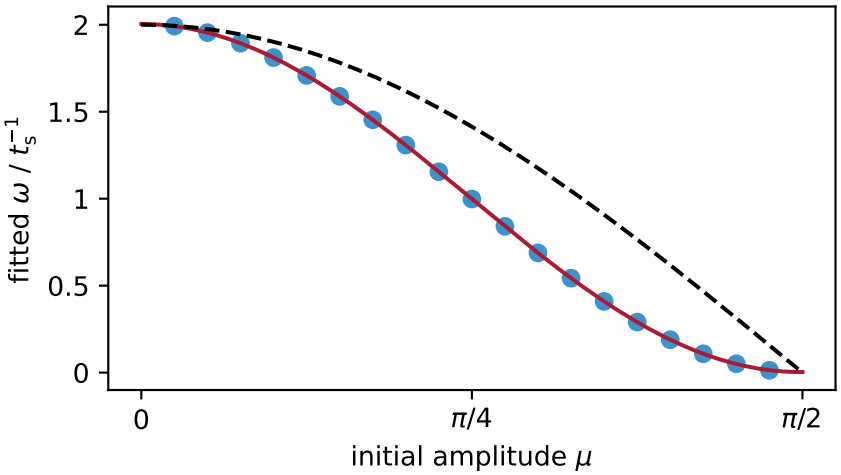

Figure 36: Measured frequency for the breather in spin-1 for different amplitude parameters μ with a fit made to the data points (red), with the fit parameters of the cosine, Eq. 62, this is approximately $\omega = 2\cos^2\mu$. Additionally, the sine-Gordon breather relation, chosen as $\omega = 2\cos\mu$, such that the maxima are the same, is plotted as the dashed line.

As the frequency depends on the amplitude of the breather, for the realisation in the experiment the question arises which impact the wrong initial amplitude for a chosen imprint shape has. For this, an initial condition as before, see Eq. 61, with a constant μ and a changing factor A in front of it, was simulated. These different factors correspond to always setting the same imprint shape with a different global amplitude, so in the experiment with different local magnetic field durations. When defining the width from a value of φ_S relative to its global maximum (like e.g. full width at half maximum), this only changes the amplitude but keeps the width constant. As the initial correct function to which the factor was applied the breather with $\mu = \frac{\pi}{6}$ was chosen, as the high frequency (low amplitude) breathers behave closer to a sine-Gordon breather and we are interested in changes occurring other than the oscillation around the other minimum (see Fig. 37).

From this data two different radiation patterns of the imprint adopting to a stable shape can be seen. They are especially visible in Q_0 and Q_{yz}. As shown in Fig. 38, for an amplitude smaller than the correct one for the set shape, the oscillations radiate outward approximately in the middle of each peak or dip. For an initial condition that has too large of an amplitude for the given width, the radiation pattern has double the frequency of the oscillation and due to this can also have the opposing sign compared to the current

state of the breather in the given observable.

What is also directly visible in this data and even better so in Fig. 37, is the change in frequency due to different amplitudes, although the general shape and therefore width stayed the same. Unlike before, the frequency when only changing the depth is not perfectly constant anymore, as the breather changes its shape over time. This can also be seen especially when looking at the sign changes of the spinorphase for $A = 1.30$ in Fig. 37. But using again a linear fit to the tilt angle of the breather over time, it is possible to extract a mean frequency over time, which is a good approximation when excluding early times where the change in the shape is strongest and late times where the radiation reaches the breather again due to the periodic boundary conditions. When looking at the resulting mean frequency over amplitude relation, see Fig. 39, with the constant relative width, it can be seen that already small changes in imprint depth lead to significant changes in frequency of the breather. For too small amplitudes the frequency becomes nearly constant approaching the maximum value of $\omega = 2$ found before, while for too large amplitudes it becomes approximately linear. Finding the observable Q_0 as a useful observable for the breather with these simulations and the radiation patterns in Q_0 for a mismatch in amplitude already helped in the currently ongoing realisation and investigation of the breather in the experiment. In this direction, future simulations of the soliton at $q \neq 0$ would also be very interesting from an experimental point of view.

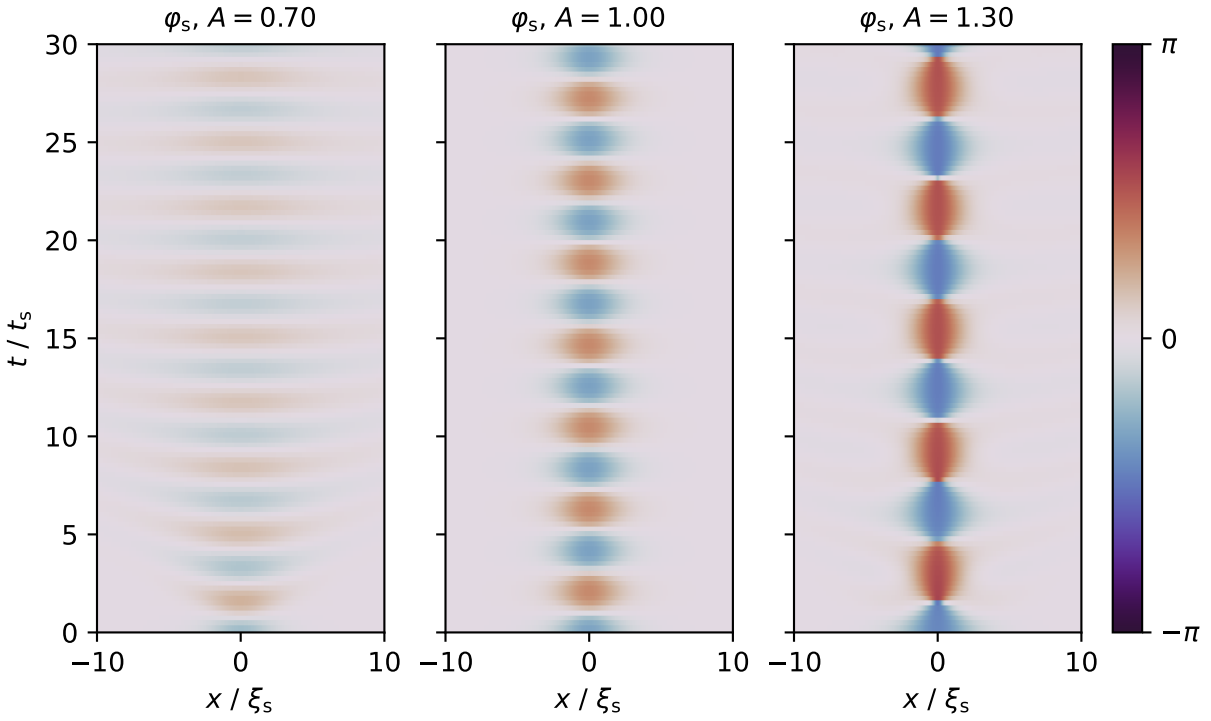

Figure 37: The breather for different amplitudes at a constant width in the spinorphase at $q = 0.001n|c_1|$. For an imprint with a lower amplitude the width gets noticeably larger over time, while for a larger amplitude the radiation is better visible in Fig. 38.

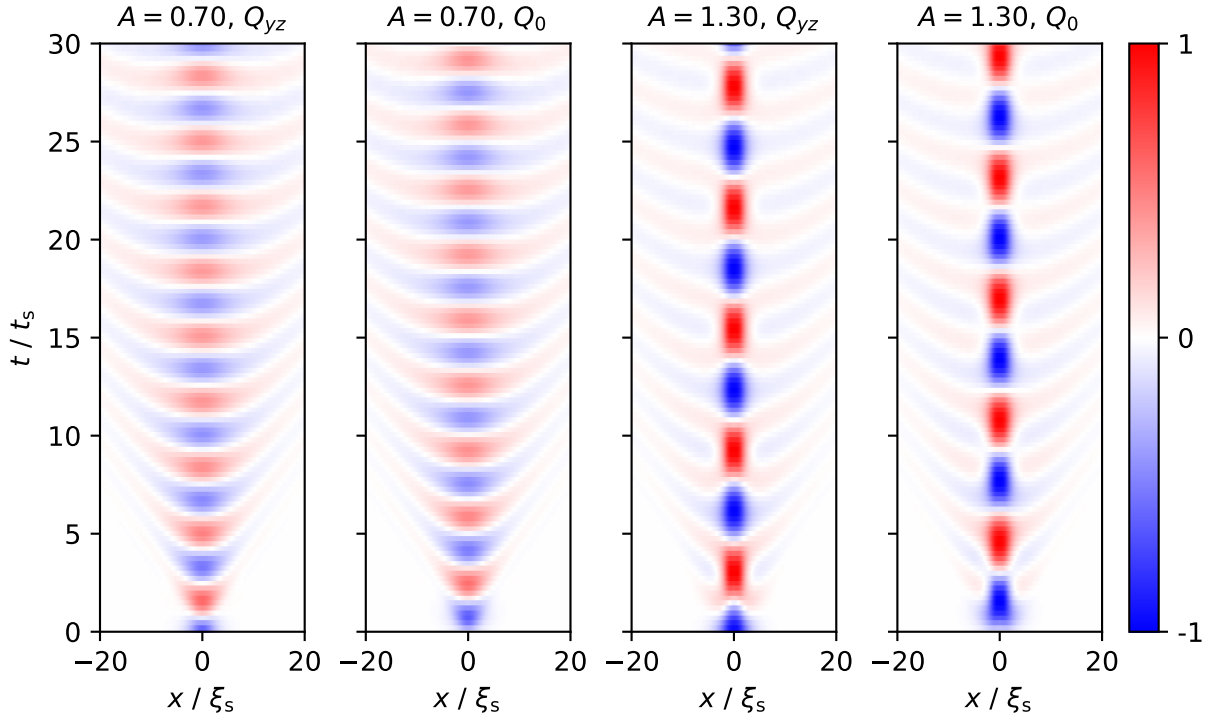

Figure 38: The radiation patterns in Q_{yz} and Q_0. The most notable difference is the number of radiation oscillations during one breather oscillation. For a lower amplitude it is one and in phase while for the greater amplitude it is two.

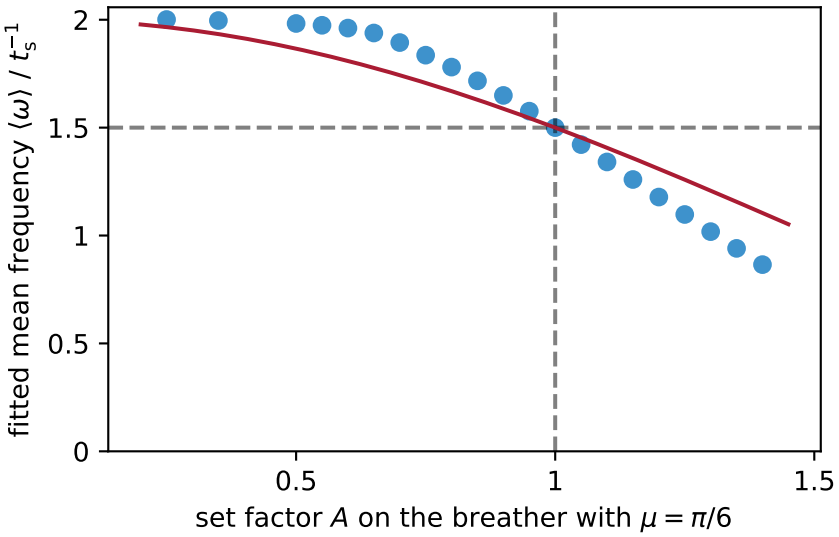

Figure 39: The mean frequency of the breather against the amplitude factor on the initial condition. The dashed lines mark the breather with correct shape and the red line is the fitted function for correct initial conditions as a comparison.

5 Tilting solitons on the spin-nematic sphere

It was insightful to track all observables on the spin-nematic sphere for the breather. Therefore and as dynamics on the nematic sphere were also observed during collisions, which will be discussed more detailed in Sec. 6, we now look at a single soliton on this sphere. From their F_x, Q_{yz} and Q_0 expectation values (see Fig. 17 and A3), one can directly see that for $q \approx 0$ the solitons discussed in Sec. 3 correspond to a half circle on the equator of the spin-nematic sphere interpolating between the two fix points in space. For both a kink and an antikink this is shown in Fig. 40. As one can see from the figure, for a kink-antikink solution these half circles overlap, but go in different directions on the sphere, while a complete circle on the equator corresponds to a kink-kink or antikink-antikink solution, depending on the direction of the circle.

As $q \approx 0$ is only an edge case of the solitons and they only start to move for $q \neq 0$, we now want to discuss how a soliton for $q > 0$ looks on the sphere when preparing it with a matched background or with a fully elongated background. In the easy-plane phase, the fix points on the spin-nematic sphere move upwards on the spheres surface along the curve with $Q_{yz} = 0$. This means that $|F_x|$ gets smaller (as can be seen in $|F_\perp|$ in Fig. 26)

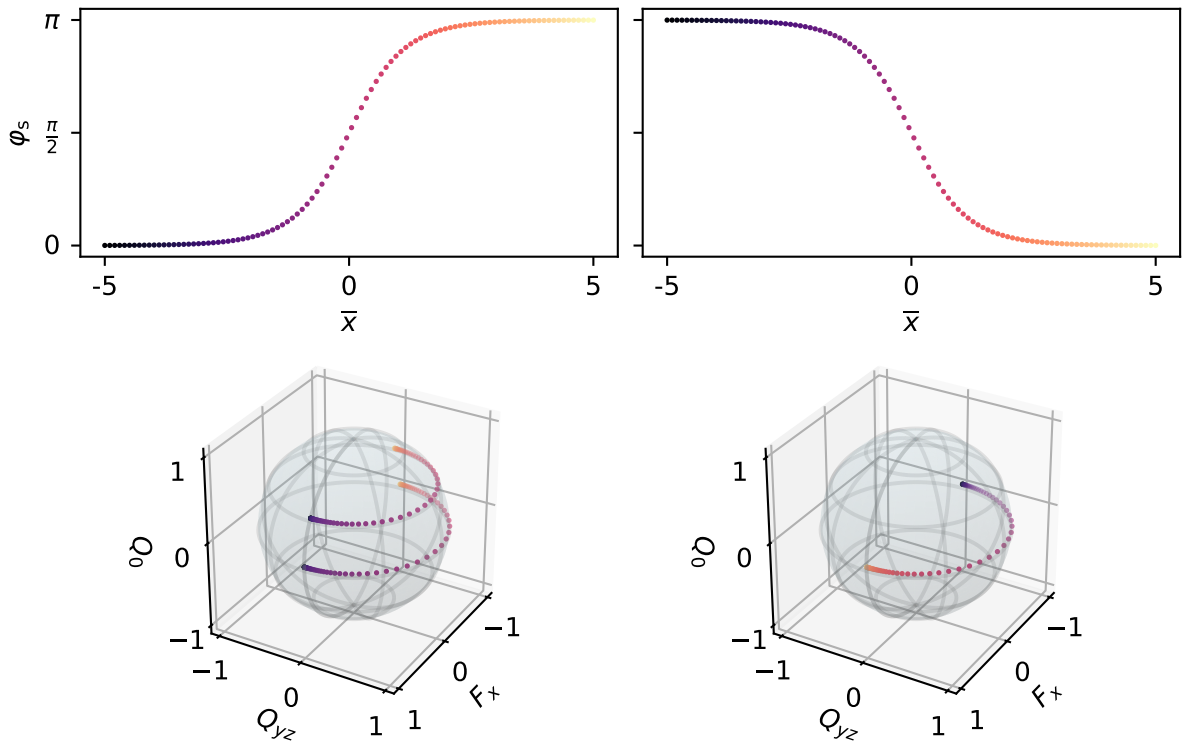

Figure 40: Kink (left) and antikink (right) in space displayed on the sphere. As one can see they run on the same side, just in opposite directions. The kink is also shown for $q = n|c_1|$ and a matched background. It looks like the unshifted kink, just moved upwards on the sphere's surface.

and Q_0 gets larger. When looking at Q_0 of the soliton for $q > 0$, one notices that it stays constant at the background value for the given q, which we will call Q_0', see Fig. 40.

The rotation of the breather around the sphere now leads to the question of whether other dynamically stable soliton solutions are also possible by rotating the solitons around the F_x-axis by an angle θ. Unlike in the case of the breather, the background value of Q_0' is not necessarily zero now, either due to preparing a matched background or the oscillations of an unmatched background for $q \neq 0$. This is incorporated in the definition of the tilting angle θ on the sphere as:

$$\theta = \arctan \frac{Q_0 - Q_0'}{Q_{yz}} \tag{63}$$

For the case of $Q_0' = 0$, this is shown in Fig. 41. As can be seen in the figure, a tilt angle leads to a steeper profile of the kink in φ_S as the spinorphase is defined by a projection onto the plane, in which the background is located (so the plane with $Q_0 = Q_0'$).

To realise a tilt angle for an unmatched background one can simply rotate the starting condition used before around the F_x-axis by the given angle. This method is chosen for the simulations, as such an F_x-rotation can also be realised in the experiment, which is

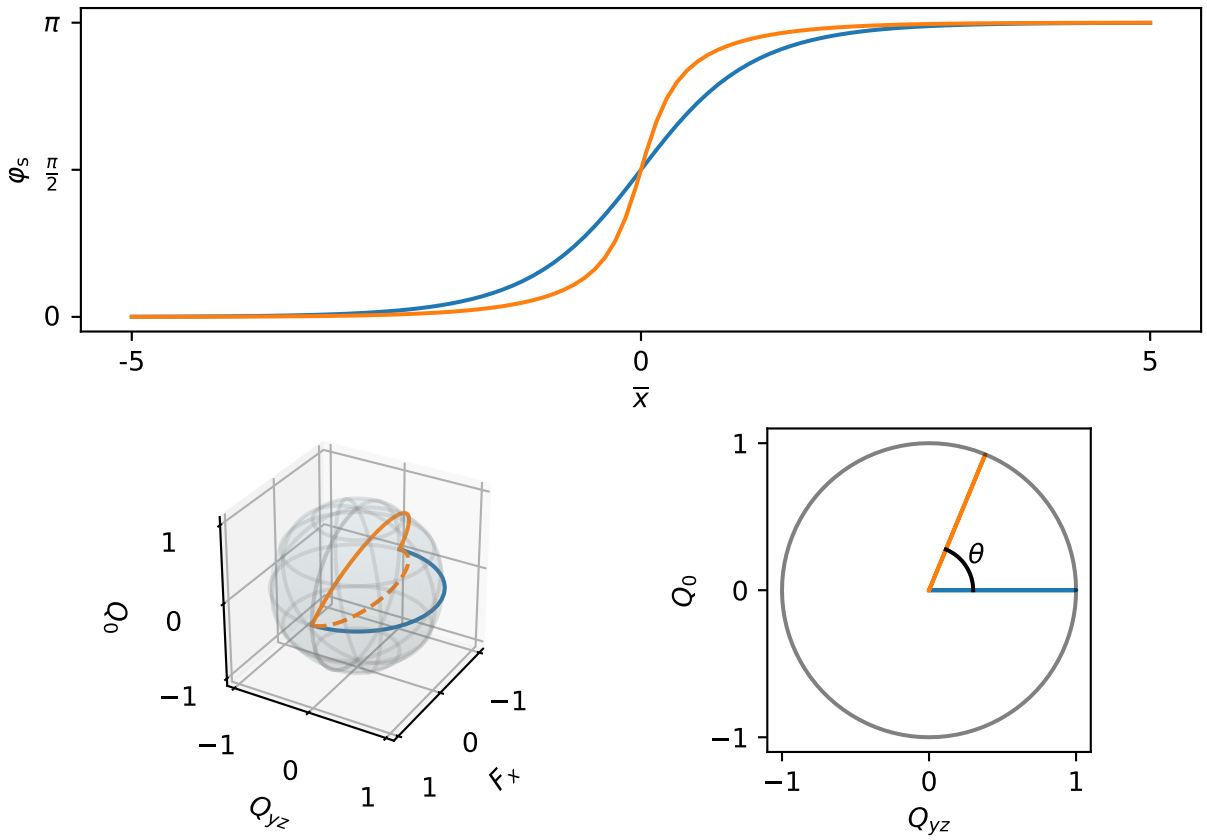

Figure 41: The definition of the tilt for $q = 0$ ($Q_0' = 0$). The projection of the tilted soliton onto the plane (dashed line) leads to a steeper spinorphase profile.

discussed in Sec. 5.1. On the spin-sphere this does not lead to any change as the state there is located on the F_x-axis, while a matched background would be modified by this rotation around the F_x-axis. A simulation of this shows that a rotated soliton indeed is stable and, as predicted, shows a steeper spinorphase profile. In the other observables this presents itself as the Q_{yz} dip or peak becoming smaller and with this at the soliton position a Q_0 dip or peak emerging, the size of which depends on the tilt angle θ. As F_x is not changed by the rotation, the profile of the soliton in F_x, and therefore also $F_\perp$, is similar to the solitons discussed before. This is comparable to the breather where the F_x-, and with it the $F_\perp$-profile, also do not change in time.

Through a rotation by $\theta = \pi$ the tilt now also connects the kink and antikink with a negative Q_{yz} expectation value to those with a positive Q_{yz} expectation value. This transforms a kink to an antikink in the spinorphase and the other way around, and therefore also switches the sign of the soliton velocity. Following this logic, there has to be a change in velocity of the soliton when changing the tilt angle. To obtain this relation, we simulated solitons tilted by different angles θ at $q = 0.30n|c_1|$ for an unmatched background. The initial tilt angle θ_{init} was achieved by taking the theoretical initial condition (see Eq. 45), so there is no radiation from adapting to the correct shape in the spinorphase, and then applying a rotation around the F_x-axis with the angle θ_{init} of the global state. To extract the velocity, the same procedure as in Sec. 3.4 is used. Additionally, the mean tilt angle at the soliton position $\langle\theta\rangle$ has to be extracted, as due to the oscillating background the tilt angle also slightly oscillates. For this, the tilt angle is calculated using Eq. 63 at the positions extracted from the fit needed to obtain the velocities and then the mean is taken in time. The resulting data (Fig. 44) shows a

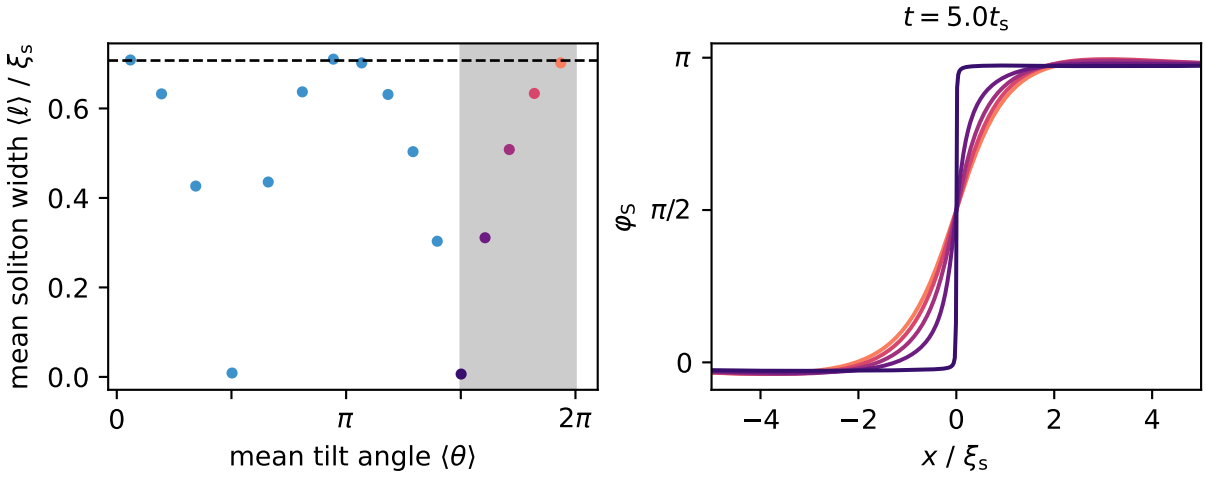

Figure 42: The mean widths of the soliton in the spinorphase over the mean tilt angle $\langle\theta\rangle$. On the right the spinorphase profiles for a kink for the last five tilt angles, marked by the shadowed region, are shown. As one can see, for $\theta \to \frac{3\pi}{2}$ the kink approaches a sharp step.

cosine-like dependence of the velocity on the tilt angle, motivating a fit function of the shape $v(\langle\theta\rangle) = v_{\text{max,fit}} \cos(\alpha_0\langle\theta\rangle + \alpha_1) + v_{\text{offset}}$. With the optimal parameters found by the fit,

$$\begin{aligned} v_{\text{max,fit}} &= (-0.3337 \pm 0.0009)\frac{\xi_s}{t_s} \\ v_{\text{offset}} &= (-0.0012 \pm 0.0012)\frac{\xi_s}{t_s} \\ \alpha_0 &= (1.000 \pm 0.003) \\ \alpha_1 &= (0.001 \pm 0.011)\,, \end{aligned} \tag{64}$$

the relation between velocity and tilt angle can approximately be written as

$$v(\theta) = -v_{\text{max}}(q)\cos\theta\,. \tag{65}$$

The "untilted" solitons discussed in Sec. 3 correspond to the case of highest velocity $v_{\text{max}}(q)$, as they have a tilt angle of $n\pi$, with $n \in \mathbb{Z}$.

This zero velocity case also makes the connection between the solitons described here

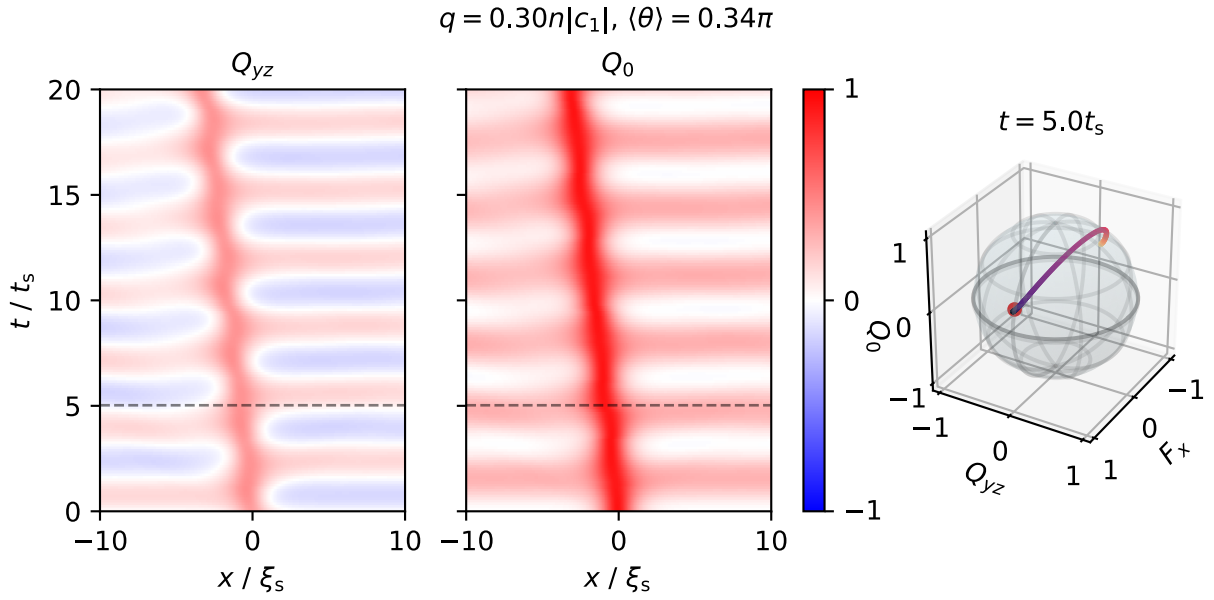

Figure 43: Q_{yz} and Q_0 for a kink with a mean tilt of $\langle\theta\rangle = 0.34\pi$. For this tilt angle the peak in Q_{yz} already is smaller as the peak in Q_0. The oscillations can be understood from the single mode dynamics (see Fig. 1). Q_0 on both sides oscillates around the positive fix point and during this staying positive, and as both sides of the soliton correspond to different sides of the sphere, they oscillate out of phase. On the right, the kink is shown for one point in time (dashed line in the other plots) on the sphere with dark points corresponding to small x-values and bright points to large ones, similar to Fig. 40. To better see that the background is at a $Q_0' > 0$, the fix point for $q = 0.30n|c_1|$ is marked in red and the equator of the sphere is highlighted.

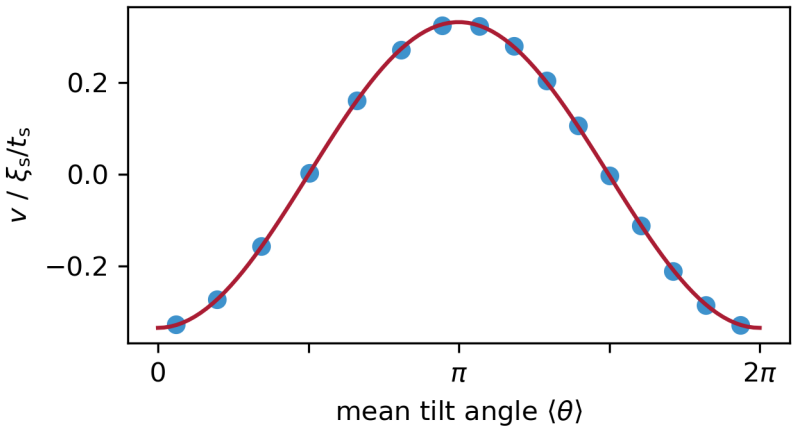

Figure 44: Soliton velocity for different mean tilt angles at the soliton position with a cosine fitted to this (red). The optimal fit parameters are given in Eq. 64. For the non-tilted sine-Gordon case discussed in Sec. 3, $\theta = n\pi$ with $n \in \mathbb{Z}$, the absolute velocity is maximal, while for the DAAD and ADDAD [15], $\theta = \left(n + \frac{1}{2}\right)\pi$, it is zero.

and the DADD- and ADDAD-solitons from [15], as the DAADs and ADDADs are just the special case of $\theta = \pm\frac{\pi}{2}$, so the soliton going over one of the poles of the sphere and having zero velocity. Additionally, this now also connects to the Ferro-Dark solitons in [16, 17], only the density dip is significantly smaller for our case of $c_1 = -\frac{c_0}{200}$, compared to the $c_1 = -\frac{c_0}{2}$ used there. In a recent publication by the same author [19], a parameter Θ, corresponding to the tilt angle used here multiplied by a factor one half, is introduced. From the solutions for the FDS given in Table I in [17] one can now also get an initial condition for preparing the tilted solitons with a matched background by taking the solutions given there and then normalizing everything to a flat density. The solitons with a tilt angle in $(0, \pi)$ correspond to the type-I and solitons with a tilt angle in $(\pi, 2\pi)$ to the type-II FDS respectively. This connection has also further been investigated by Florian Schmitt, a PhD student from the theory group of Thomas Gasenzer, who used Newton relaxation to see how the FDS behave for a changing c_1 and found that the FDS with $Q_{yz} = 0$ for $c_1 \sim \frac{c_0}{200}$ correspond to the DADD- and ADDAD.

5.1 Realisation in the experiment

To realise the tilting of the solitons on the nematic sphere in the experiment, first the soliton imprint is performed as before. After the imprint, an RF-pulse is applied rotating around the axis in the F_x-F_y-plane along which the spin is oriented in the starting condition. So, when calling this axis F_x, a rotation around F_x is performed. To find this axis, a scan of the phase setting of the pulse for a fixed pulse duration is made. This phase determines around which axis in spin-space a rotation is performed. If the F_x-axis is not hit, a signal will be visible in the F_z-readout as the part of the spin not parallel to the

readout axis will be rotated in F_z, which can be seen in Fig. 45. Afterwards, the pulse length can be calibrated using again the F_z-readout as the local non-zero expectation value of Q_{yz} at the soliton position now gets rotated to Q_0. This is shown in Fig. 45. By measuring the expectation value in Q_0 for different pulse durations, one can obtain the duration needed to obtain a certain depth in Q_0. As can also be seen, at the right of the dip, some additional structure appears. The reason for this structure, likely is that this is where the imprint is performed, which could for example not be uniform enough.

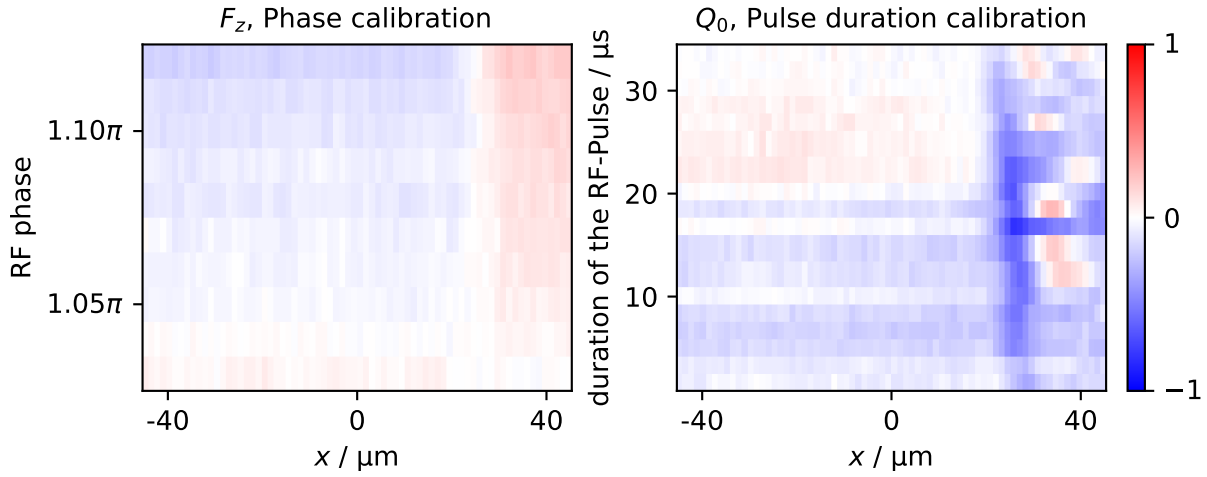

Figure 45: Calibration of the RF-pulse phase to match an F_x-rotation. For this the F_z-readout is used, as a rotation around the wrong axis leads to a non-zero F_z-expectation value in the background. The pulse duration for this calibration was set to $0.4 \cdot \tau_\pi/2 = 13\mu s$. From this an optimal phase of 1.03π was obtained, which was then used to compare the pulse duration to the tilt angle. This was measured in the F_z-readout again, as the interesting value is Q_0, where the depth of the resulting dip at the soliton position relates directly to the tilt angle. As one can see, the dip gets deeper for longer pulse durations.

The first results obtained by using this imprint are shown in Fig. 46. They are measured using the F_z-readout and show a time evolution of differently tilted solitons in Q_0. The strength of the tilt was set by different durations of the rotation pulse leading to visibly different depths of the emerging dip in Q_0. While there are still visible deviations from the intended initial state, like the negative Q_0 value in the left half of the image, the soliton can still be identified. To highlight its position the minimum of Q_0 in each time step is marked by the additional line. Here, it is also visible that the velocity of the dip gets lower for longer pulse durations, and the dip is stable for longer than a second, even when bouncing on the wall. So, while there is still work needed regarding the calibration, and for an $F_\perp$- and φ_S-readout with this preparation, to verify if these are indeed the tilted solitons, these results look very promising.

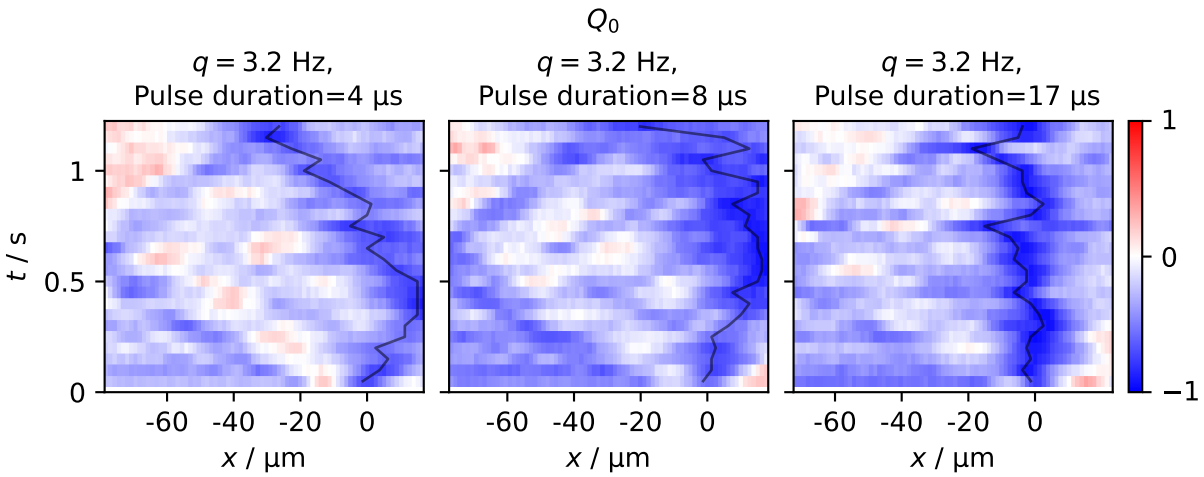

Figure 46: At a constant $q = 3.20$Hz and phase of the F_x-pulse of 1.03π, the time evolution of the soliton was taken for different rotation pulse durations, so different initial tilt angles. While there is still some work needed to get a more stable background, the minimum in Q_0 in the right half in space (marked by the line) is clearly visible over time. When tracing it one can also see the velocity getting smaller for a larger dip in Q_0 as one would expect from the numerics. An interesting feature visible in all three measurements is the region of negative Q_0 on the left that starts directly next to the dip, goes towards the wall and there seems to be reflected as a single dip.

6 Collisions

As shown in Sec. 3 and 4, the untilted solitons share characteristics of sine-Gordon solitons, and for small amplitudes also the realised breathers behave similarly to sine-Gordon breathers. To further probe how close the underlying model is to a sine-Gordon model and as collisions were also the first observed proof of these solitons in the experiment, soliton collisions are investigated in the following. Especially the phase shift δx, which is the coordinate shift between in- and outgoing trajectory of elastically colliding solitons, as shown in Fig. 7, is of interest for this, as for sine-Gordon kink-antikink collisions there is a clear prediction of the phase shift for different incoming velocities, given in Eq. 17.

6.1 Collisions for different quadratic Zeeman shifts

As the effective model was derived for the regime of the untilted solitons, we first simulate collisions of these and use q to control their initial velocity. To obtain a first result with minimal additional influence on the phase shifts, this is done with the theoretical initial condition in the spinorphase and a matched background, in contrast to the experiment where the background was not matched for $q > 0$. As only q is changed, kink and antikink have the same absolute incoming velocity $|v_{\text{in}}|$ only with opposing signs. When putting them close to each other, this directly leads to a kink-antikink collision, although the distance between them has to be chosen large enough to get a linear incoming trajectory, needed for extracting phase shifts.

The results confirm that, like in the sine-Gordon model (see Fig. 7), the spinorphase flips at the collision point. The spin-1 system realises this phase flip by a rotation around the spin-nematic sphere, which can be seen in the observables spanning the sphere in Fig. 48 and always goes over the south pole of the sphere, so negative Q_0. To now investigate the collision and this flip on the sphere more in depth, first the soliton positions are extracted again for every time step. This is done similar to the approach used in Sec. 3.4, only now there is a profile of two dips fitted to $|F_\perp|$. With the positions of the solitons the rotation of a soliton on the sphere can now be quantified by calculating the tilt angle at the found position of the soliton for every time step. For this Eq. 63 is used and, as kink and antikink have the same tilt angle not only in the starting condition (see Fig. 40) but also during the rotation (follows from Fig. 48), it is enough to further look into this for one of them. When plotting the tilt angle at the soliton position over time, Fig. 49, it was empirically found that it follows a tanh. With this, the tilt angle over time during the collision $\theta(t)$ is then fitted as

$$\theta(t) = \theta_{\text{amp}} \tanh\left((t - t_{\text{col}})/\tau_{\text{col}}\right) + \theta_{\text{offset}} \,, \tag{66}$$

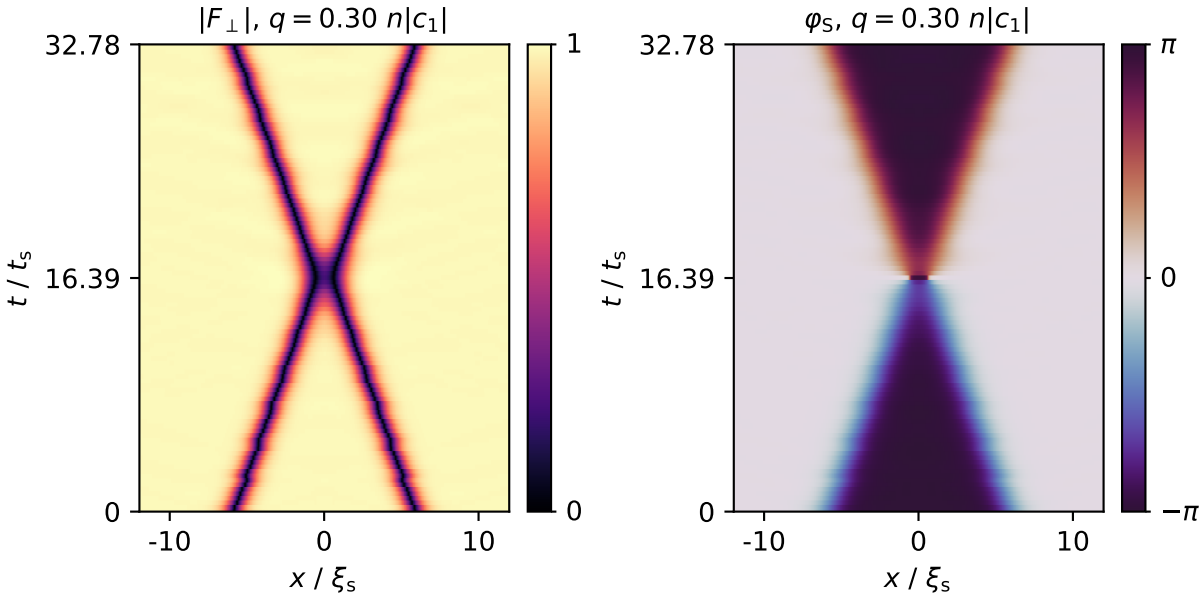

Figure 47: The collision between an antikink and a kink in the simulation at $q = 0.30n|c_1|$. In $|F_\perp|$ one can nicely follow the trajectory of the solitons, which is extracted through a fit to the two dips. In the spinorphase the flip of the occupied potential minimum between the kink and the antikink from $-\pi$ to π, and with this the switch from antikink-kink to kink-antikink, at the collision point is clearly visible, leading up to the question of how the solitons traverse the nematic sphere during the collision.

where especially the collision time t_{col} and the width of the collision in time τ_{col} are interesting for further analysis. Additionally, the amplitude of this function θ_{amp} and its offset θ_{offset} are obtained in the fit. To extract the phase shift we need a linear incoming and a linear outgoing trajectory. If the velocity of a soliton depends on the tilt angle like in Eq. 65 also during the interaction with another soliton, the asymptotic behaviour of the tanh can be used to define regions of constant velocity. To test this, the initial velocity v_{init} of one soliton is obtained by a linear fit to the first few time steps and then using the initial position x_0 and Eq. 65 with $\theta(t)$ the trajectory predicted by the tilt angle for the left antikink with $\theta(t = 0) = \pi$ is:

$$x_\theta(t) = x_0 - \sum_{t'=t_{\text{start}}}^{t} \Delta t_{\text{saved}} v_{\text{init}} \cos\theta(t') \tag{67}$$

Here Δt_{saved} is the spacing between two time slices saved in the simulation and for the right kink the sign in front of the sum changes. The trajectory arising from this is then compared with the actual soliton trajectory in Fig. 49. Between the two trajectories mostly a small offset in the beginning is noticeable. This is very likely due to the density dip forming at the soliton position and the soliton itself not being accelerated instantaneously.

Through the extracted trajectory the tilt angle now helps in quantitatively evaluating

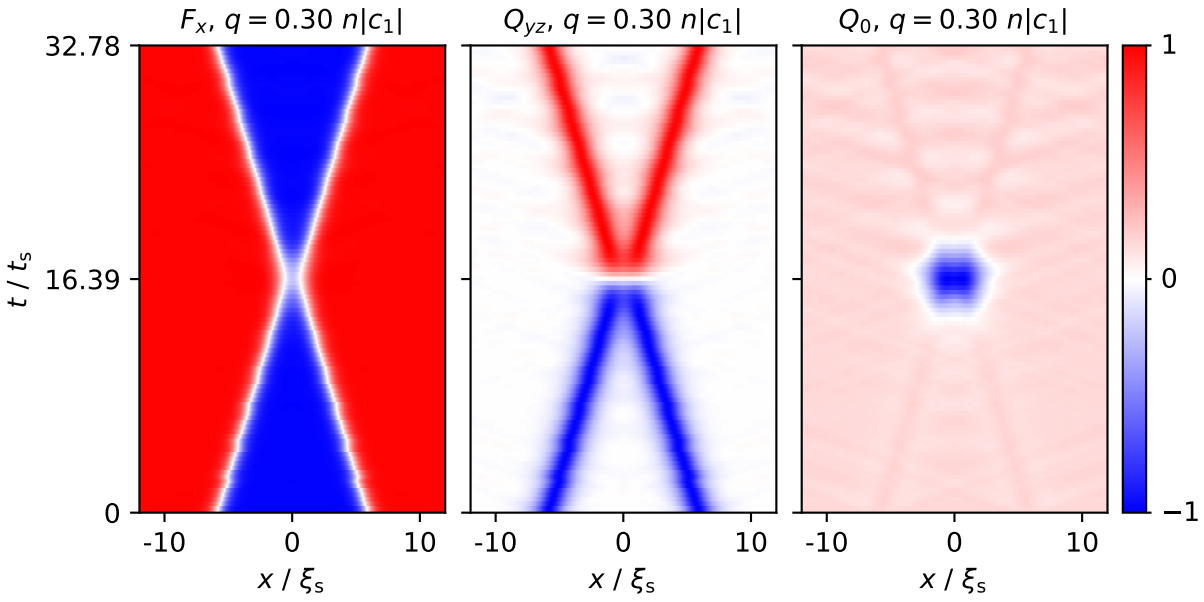

Figure 48: The collision in the observables making up the spin-nematic sphere. While F_x stays approximately constant, Q_{yz} flips its sign and in Q_0 a dip emerges during the collision. On the sphere this corresponds to a rotation from the initial $\theta_{\text{init}} = \pi$ over the south pole to the opposite site $\theta = 2\pi$. As can also be seen here, the solitons develop a small peak in Q_0 on the order of $Q_0' + 0.01$ compared to the background value Q_0'. This is comparable to the size of the radiation from the formation of the soliton (compare Fig. A3).

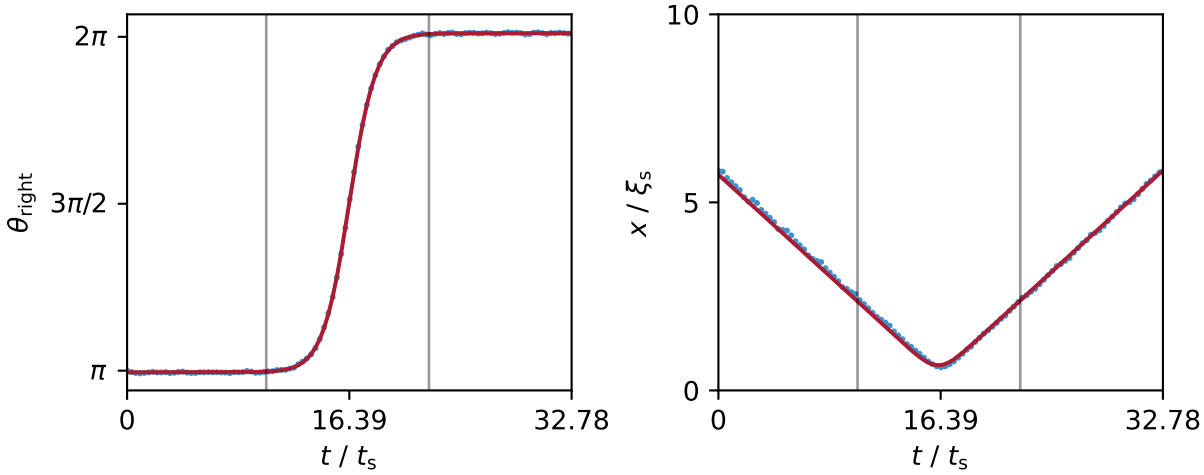

Figure 49: The tilt angle of the right soliton for the collision shown in Fig. 47 and 48. To this a tanh is fitted (red line) from which the position t_{col} and width τ_{col} of the collision is extracted. This is then used to define the collision region $[t_{\text{col}} - 3\tau_{\text{col}}, t_{\text{col}} + 3\tau_{\text{col}}]$ indicated by the two grey lines. On the right the trajectory obtained by the tilt angle using the incoming velocity of the soliton and the starting position through Eq. 65 (red line) is compared to the actual trajectory of the soliton.

the collisions, as it allows defining a region of constant velocity, and thereby a linear trajectory, before and after the collision. For this, the collision position t_{col} and width τ_{col} extracted from the fit to the tilt angle are used to define the collision region as $[t_{\mathrm{col}} - 3\tau_{\mathrm{col}}, t_{\mathrm{col}} + 3\tau_{\mathrm{col}}]$, shown in Fig. 49 as the grey lines. The times before the collision region are then used to obtain the incoming trajectory, and the times after the collision region to obtain the outgoing trajectory. Both trajectories are then defined by taking the distance between the solitons at each time step in the specific region and making a linear fit to them. This is shown in Fig. 50. Here, the distance between the solitons is taken, so only relative shifts between the solitons are taken into account, which is relevant in the experiment, where the same evaluation method is used. As can be seen in Fig. 50 the phase shift δx can then be extracted by "reflecting" the incoming trajectory at the point where it goes to zero and then taking the distance between this linear function and the linear function fitted to the outgoing trajectory. This difference is then twice the phase shift as it is the shift in the distance between the solitons, but we are interested in the shift of the trajectory of one soliton. When using this method, one assumes that the velocity of the kink is the same as that of the antikink also after the collision. This is confirmed by performing two separate linear fits yielding that the absolute value of the ratio between the velocity of the left and right soliton differs less than $2 \cdot 10^{-4}$ from one, which is shown in Fig. A8.

In the sine-Gordon model collisions are fully elastic, so $\left|\frac{v_{in}}{v_{out}}\right| = 1$, with the incoming velocity v_{in} and the outgoing velocity v_{out}. As one can see in Fig. 51 on the left, here the elasticity is approximately one for small q, but starting at $q \approx 0.4|nc_1|$ gets noticeably

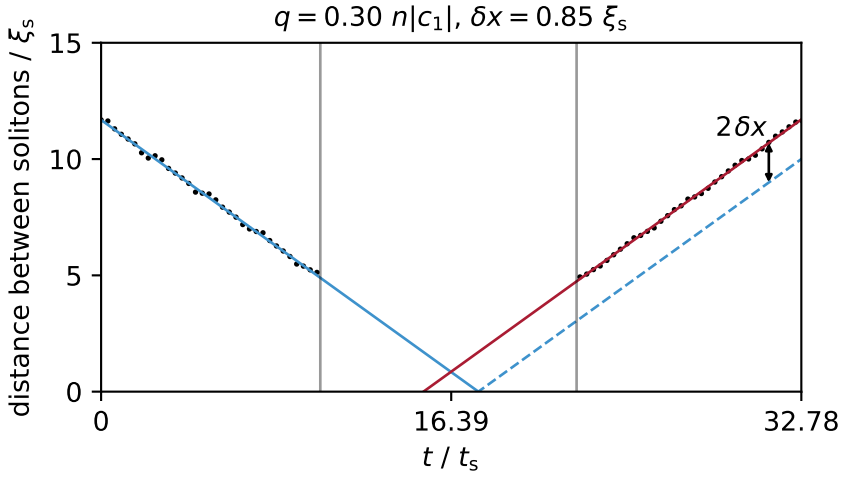

Figure 50: The linear fits to the distance between the solitons before (blue) and after the collision (red). The coordinate shift between in- and outgoing trajectories is clearly visible, when comparing the fit to the soliton distance without phase shift (blue dashed). The distance between the two lines in this plot is two times the phase shift δx, as it is the change in distance between the solitons and not of one soliton position.

smaller. This is expected as the double frequency term of the double-sine-Gordon model should now play a larger role, but also means that the extracted phase shifts get less exact, as the obtained value depends mostly on the time at which it is measured if the elasticity differs from one.

The phase shifts obtained for this data are plotted in Fig. 51 on the right over the incoming velocity v_{in} of the solitons. To the points, at which the elasticity deviates at maximum by one percent from one, the sine-Gordon prediction with the inverse of the speed of sound of the underlying effective sine-Gordon model c^{-1},

$$\delta x = \frac{2}{m}\sqrt{1-(c^{-1}v)^2}\ln\left|\frac{1}{c^{-1}v}\right|, \tag{68}$$

see also Eq. 17, is fitted. The result of the fit is shown in Fig. 51 and gives the optimal parameters:

$$\begin{aligned} m &= (2.50 \pm 0.03)\xi_{\text{s}}^{-1} \\ c^{-1} &= (0.993 \pm 0.014)\frac{t_{\text{s}}}{\xi_{\text{s}}} \end{aligned} \tag{69}$$

The inverse of the speed of sound approximately being one means that for this case the ratio between ξ_{s} and t_{s} is the same as the ratio between dimensionless space and time of the effective sine-Gordon model, as in [2], matching the prediction by the LEEFT for $k \approx k_{\xi_{\text{s}}}$ (see Eq. 24 and 25). However, the sine-Gordon mass m obtained by this fit differs notably from the sine-Gordon mass predicted by the LEEFT (see Eq. 36 and 37). It has to be noted that the sine-Gordon mass m here also includes a potential scaling factor of x, as the phase shifts are given in units of ξ_{s}, which might not be the natural unit of space of the underlying sine-Gordon model, although the speed of sound being approximately one hints towards a different origin of the observed sine-Gordon mass. A very likely source for this is the fact that the LEEFT is derived for the plane with constant $Q_0 = Q_0'$ including the fix points, so the planes in which the solitons lie when not interacting for an unmatched background. During the collision they now get tilted and therefore leave this plane, leading to different potential contributions to the phase shift. To get a better understanding of this an effective theory describing the tilt angle dynamics could be very helpful.

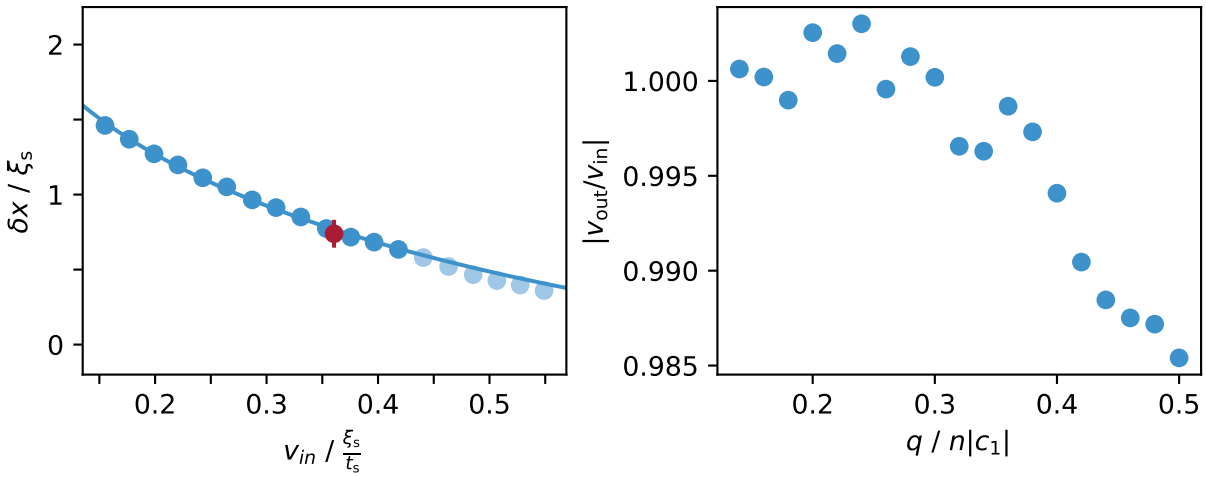

Figure 51: (left) The elasticities of the collisions for different q. For large q it is close to one so in- and outgoing velocity are approximately the same, while for larger q it gets more inelastic. (right) The phase shift δx of collisions for different incoming velocities (v_{in}) controlled by setting a different q. The fit is made to values for which the elasticity deviates at maximum by 0.5% from one, leading to the parameters given in Eq. 69. The values with an elasticity deviating by more than 0.5% from one are transparent. In red the value obtained from the experiment [1] is shown.

6.2 Collisions in the experiment

In Fig. 51 an additional red point is included. This point stems from a collision measured in the experiment, shown in Fig. 52. To obtain the phase shift there, the F_x-F_y-readout is used. Due to this, the tilt angle cannot be used to extract the collision region, as this would require too many additional observables. Instead, the distance between the solitons d_{solitons} relative to the mean width of the solitons $\langle \ell \rangle$ is used to fix the collision region as $d_{\text{solitons}} < 3\langle \ell \rangle$. Afterwards, the same analysis as on the numerical data was made, leading to an elasticity of $\left|\frac{v_{in}}{v_{out}}\right| = 0.90 \pm 0.02$ and a phase shift of $\delta x = (5.82 \pm 0.73)\mu\text{m}$ at an incoming velocity of $v_{\text{in}} = (16.76 \pm 0.27)\mu\text{m}\,\text{s}^{-1}$. To then compare this with the values from the numerical simulation, the SI-units have to be converted to the spin-1 units ξ_s and t_s. For this, the mean width of the soliton $\langle \ell \rangle = 5.6\mu\text{m}$ is obtained from the fits in the experiment and then Eq. 41 and 42 are used to obtain approximate values for $\xi_s = 7.9\mu\text{m}$ and $t_s = 0.17\text{s}$ in the experiment. With this, the incoming velocity $v_{\text{in}} = 0.36\frac{\xi_s}{t_s}$ and the phase shift $\delta x = 0.74\xi_s$ are found, which match the values found in the simulation well, as shown in Fig. 51.

One can also experimentally obtain a dataset where spinorphase φ_S and transversal spin $|F_\perp|$ are measured simultaneously. This readout, called the dual-phase-readout (DuPR), "dual" as it allows the readout of φ_L and φ_S in one shot, was developed by the other master's student of the team [37]. With this readout the same behaviour for φ_S during the collision as numerically is found, see Fig. 53. As the signal in φ_S is still relying

on the spin being at least partially aligned with F_x, this picture is put together by shots from multiple scans. Due to this, this data was not used for the phase shift extraction, as on the timescale of multiple scans the quadratic Zeeman shift q, as seen by the atoms, and with it the incoming velocity might drift and due to there being less atoms used for obtaining F_x and F_y there is also larger noise on the data in $|F_\perp|$ compared to the data measured with the F_x-F_y-readout. However, especially the also developed full spin-nematic readout (F_x-Q_{yz}-F_z) [37] enables the extraction of the tilt angle during collision, which is subject of future work in the group.

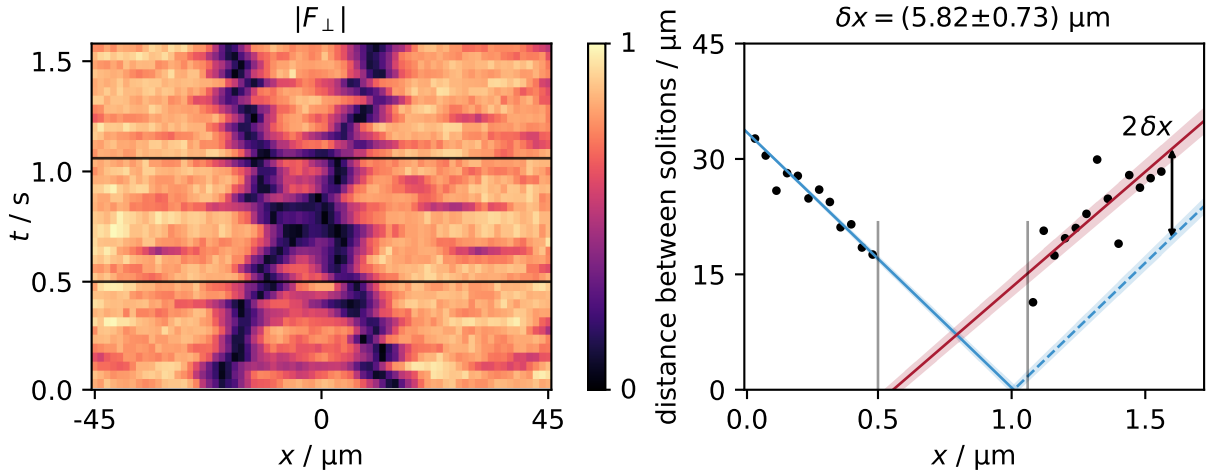

Figure 52: The $|F_\perp|$ data of the collision used to extract the phase shift from the experiment. With the black lines the collision region defined by the distance of the solitons is indicated. On the right the processed data for the phase shift extraction is shown. The data and figures are taken and modified from [1].

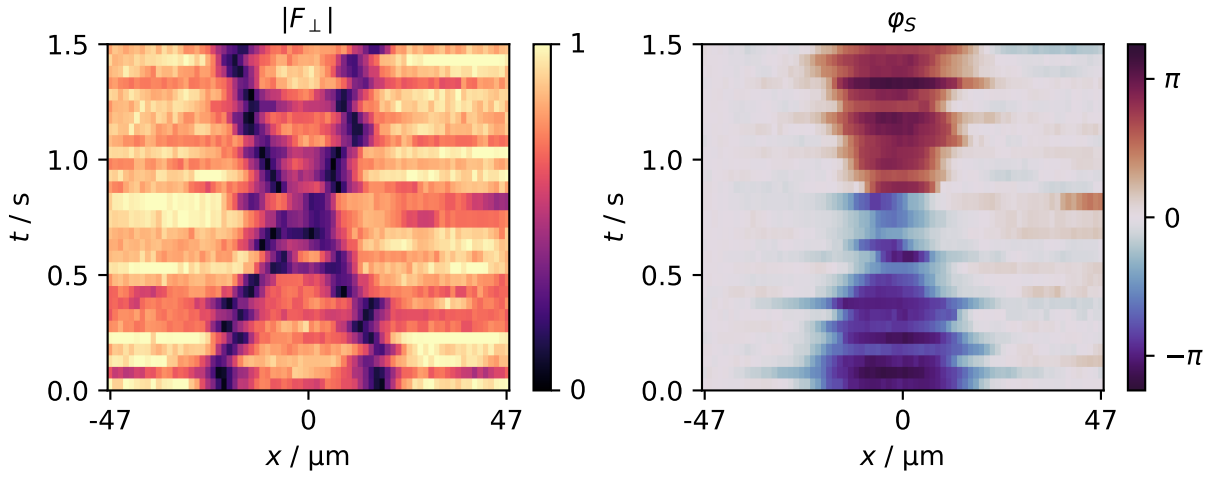

Figure 53: φ_S and $|F_\perp|$ for a kink-antikink collision in the experiment measured in a simultaneous readout. The readout allowing this was developed in [37] and the plot is taken and modified from [1].

6.3 Collisions with an unmatched background

Compared to the numerically obtained values for the elasticity, the experimentally obtained value is significantly lower. To look into potential reasons for this, the collisions are also simulated for an unmatched background, as the matching of the background already had an impact on the velocities starting from $q \approx 0.4n|c_1|$. Aside from the different preparation of the background the procedure for the phase shift extraction stays the same. The resulting elasticities do not follow a clear pattern, but already for small q deviate up to 6% from one, as shown in Fig. 54. The reason for this seems to be the phase of the background oscillation at the time of the collision t_{col}. From a maximum in $|F_\perp|$ they can draw kinetic energy making the collision superelastic ($\left|\frac{v_{in}}{v_{out}}\right| > 1$), while for collisions at the minimum they get inelastic ($\left|\frac{v_{in}}{v_{out}}\right| < 1$). This can be seen in Fig. 55, for which the collision was simulated at a constant $q = 0.50n|c_1|$ and the initial distance of the kink and antikink was changed leading to different collision times. These different collision times in return lead to a different background value at the collision time, shown in Fig. 56. In this figure, one can also see that the different collision times also lead to a different trajectory of the dips in $|F_\perp|$. For the superelastic collision the two dips merge into one dip, while for the nearly perfectly elastic collision they stay clearly separated. The oscillation of the background and the elasticity match not perfectly, which is also expected, as the background dynamic at the soliton position already differs visibly from the actual background away from the simulation taken as a value here, which also is visible in Fig. 56. This is currently analysed on experimental data by Alexander Schmutz (another PhD student from the group).

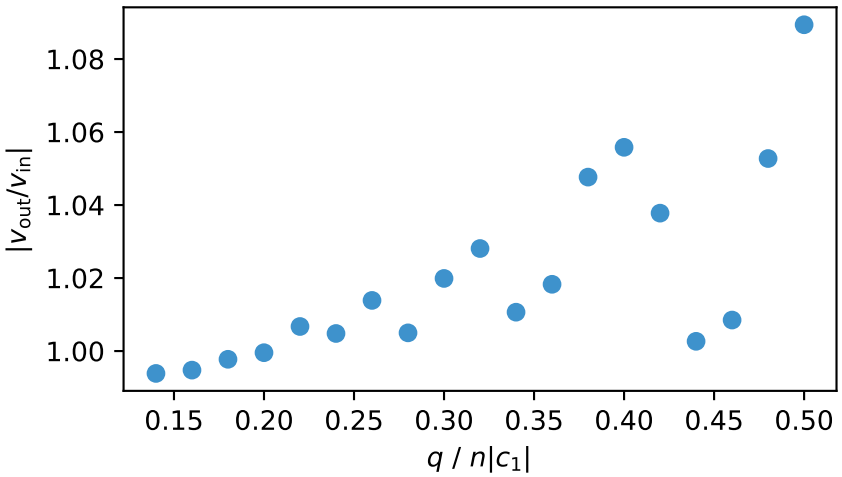

Figure 54: Elasticities for different q with an unmatched background, leading to superelastic collisions. As shown in Fig. 55 the elasticity depends on the background value at the collision time.

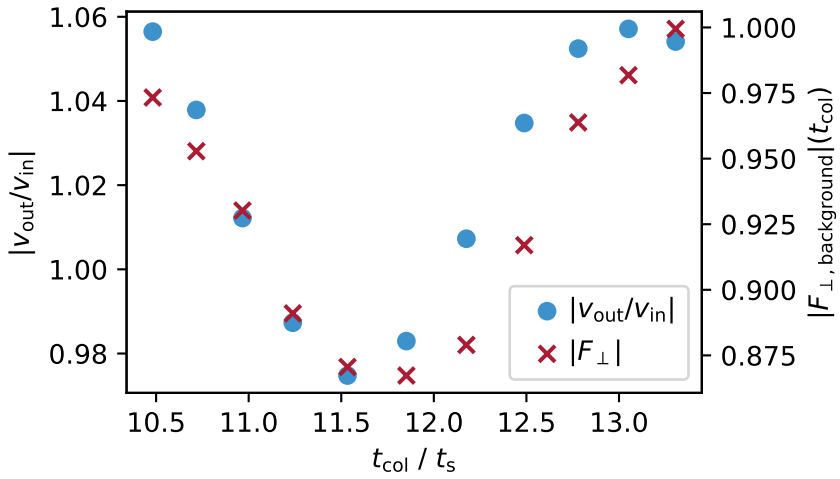

Figure 55: The background value of $|F_\perp|$ (red x) and the elasticity of the collision (blue points) for constant $q = 0.50n|c_1|$ and different collision times t_{col} due to different initial distances between kink and antikink. The background value is taken far away from the collision as a mean value of 20 grid points.

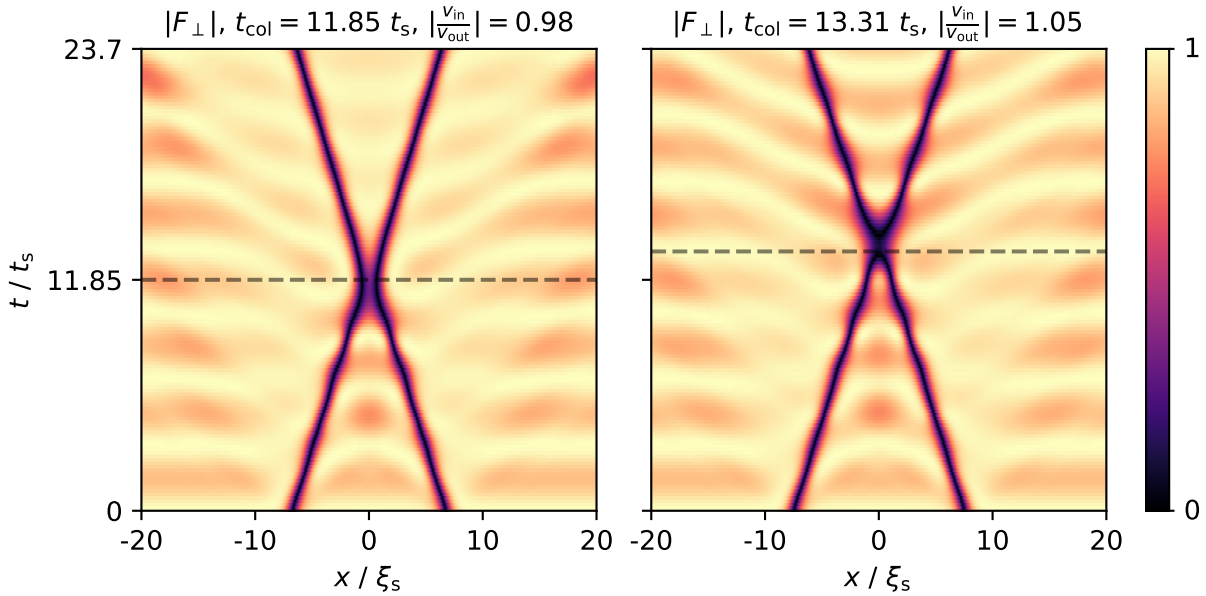

Figure 56: The collision in $|F_\perp|$ for two different initial distances between the solitons with an unmatched background at $q = 0.50n|c_1|$. The collision times are marked by the dashed line. On the left the background is approximately at the maximum of the oscillation at the collision point leading to a superelastic collision and on the right the background is approximately at its minimum leading to an inelastic collision.

6.4 Collisions at a constant tilt angle for different quadratic Zeeman shifts

To check if the origin of the deviation of the extracted sine-Gordon mass from the prediction by the LEEFT is due to leaving the plane of the stable points for the set q, the phase shifts are taken again for different q, but this time with the initial condition being tilted solitons. Similar studies have been made for a special case for strong spin-spin-interactions [18]. In the following, a tilt angle of $\theta = -3\pi/4$ is used for this. The resulting phase shifts allow for again fitting the sine-Gordon prediction (see Eq. 17), leading to:

$$\begin{aligned} m &= (2.515 \pm 0.007)\xi_\mathrm{s}^{-1} \\ c^{-1} &= (0.725 \pm 0.004)\frac{t_\mathrm{s}}{\xi_\mathrm{s}} \end{aligned} \tag{70}$$

The sine-Gordon mass combined with the potentially different scaling in space matches the one obtained from the untilted collisions within one standard deviation (compare Eq. 69), but the difference in the speed of sound is significantly larger. This means that either a change in space scaling or time scaling occurs. The fact that the sine-Gordon mass found here matches the one found for the untilted solitons is not conclusive for the question whether the actual sine-Gordon mass changes, as the fit parameter m also includes a scaling of space from the dimensionless sine-Gordon space to units of ξ_s, which might just compensate the change in the actual sine-Gordon mass. Pointing towards a change in spatial scaling is the fact that the width of the soliton also changes for a tilt, as shown in Fig. 42. Both a shift in space or time scaling mean that different tilt angles lead

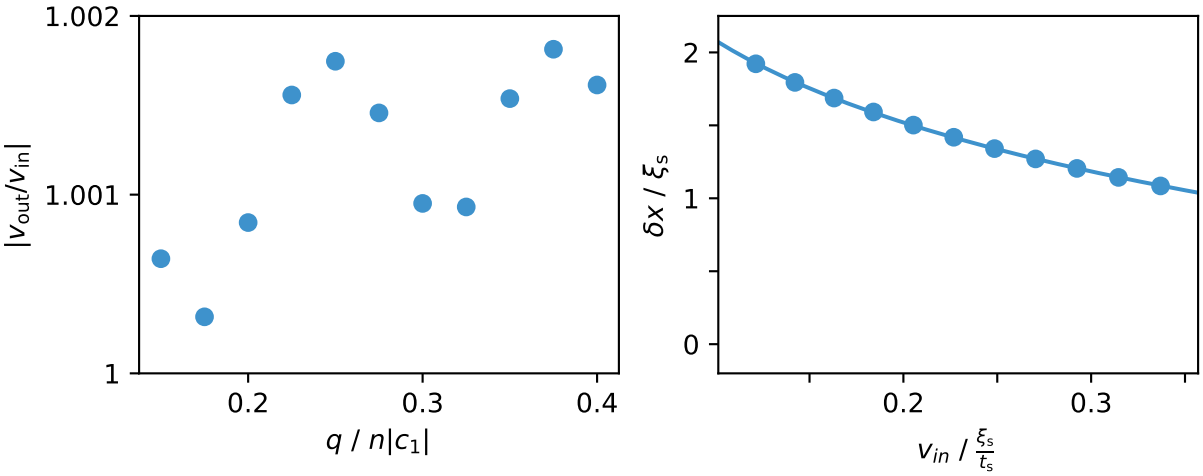

Figure 57: Elasticities and phase shifts for kink-antikink-collisions with both solitons at an initial tilt angle of $\theta = -3\pi/4$ and different q set. The elasticities only deviate from one by 0.2% and the parameters found by a fit to the phase shifts (shown as the line) are given in Eq.70.

to a different effective sine-Gordon model in the spinorphase. During the collision this leads to the solitons exploring different sine-Gordon models which sum up to a different sine-Gordon mass observed from the phase shift than in the sine-Gordon model of only the plane.

6.5 Collisions for different tilt angles

After collisions with a fixed initial tilt angle at different q, kink-antikink collisions for different initial tilt angles at a constant $q = 0.2n|c_1|$ were also simulated. The value of q was chosen this low to have an elasticity of approximately one for untilted solitons even with an unmatched background. By this, the tilting can be realised by an F_x-rotation, similar to the experimental preparation described in Sec. 5.1. When comparing the collisions, one finds that even for solitons with a positive Q_0 expectation value at their position, the rotation during the collision always occurs over the pole $Q_0 = -1$ of the spin-nematic sphere, which can be seen in Fig. 58. Their final position on the sphere, in the fully elastic case, is at the same value of Q_0 they initially had, just with the sign of Q_{yz} flipped, which is likely due to energy conservation. For all initial tilt angles the time evolution during the collision follows a tanh, which also still describes the trajectory outside of the core of the collision, as shown in Fig. 59 for an initial $Q_0 > 0$.

When plotting the elasticities and phase shifts for this, see Fig. 60, one notices that the elasticities of the solitons with a positive Q_0 expectation value tend to have a larger difference from one. These solitons are also significantly less stable, which agrees with the findings in [15], and already decay for times smaller than $10 \cdot 2\pi_\mathrm{s}$, when colliding. Due to the oscillating background, the elasticities in general differ by a larger amount from one than before. To accommodate for this, the fit to the phase shifts is now performed on the values with an elasticity differing by a maximum of 2% from one. This fit leads to the optimal parameters:

$$\begin{aligned} m &= (1.444 \pm 0.023)\xi_\mathrm{s}^{-1} \\ c^{-1} &= (1.82 \pm 0.03)\frac{t_\mathrm{s}}{\xi_\mathrm{s}} \end{aligned} \tag{71}$$

The value found for the sine-Gordon mass matches the prediction for the mass made by the LEFFT for $k = k_{\xi_\mathrm{s}}$, $m = \sqrt{2}$, within two standard deviations, but compared to before the speed of sound now has a value significantly different from one. It is interesting that controlling the soliton velocity in a different way, yields such a different outcome for the parameters of the phase shift relation, while in every case investigated here, still following a function of the shape expected in a sine-Gordon model. To make more precise statements on the change of the parameters for both changing θ and changing q further studies on larger datasets are needed.

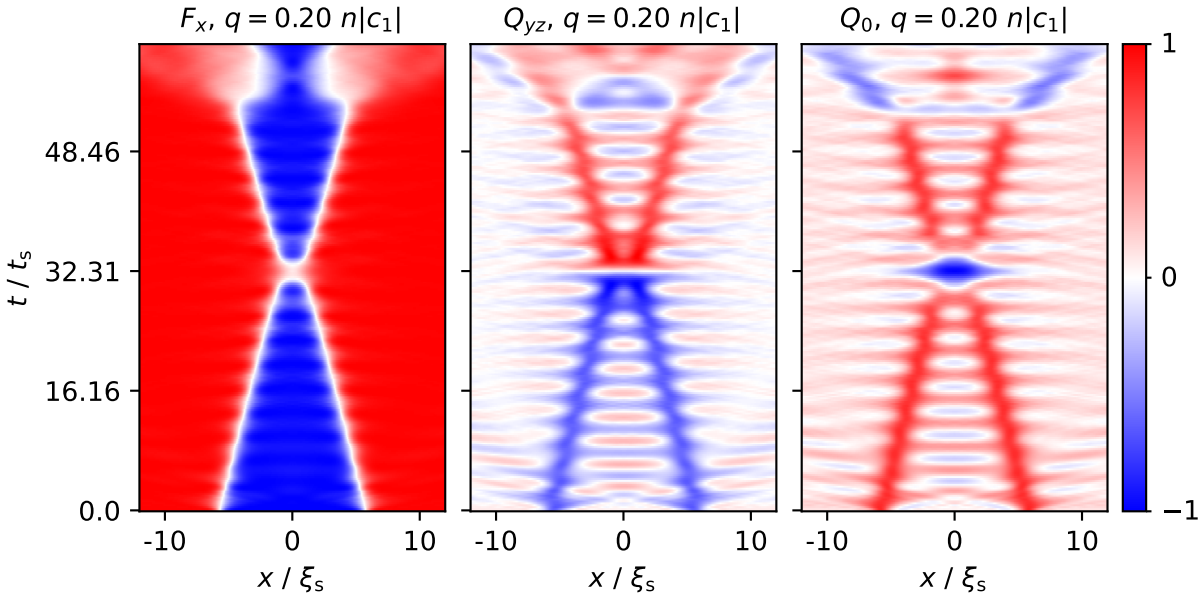

Figure 58: The kink-antikink collision with a mean initial tilt angle $\langle\theta_{\text{right}}\rangle = 0.72\pi$. Even with this positive initial Q_0 expectation value at the soliton position the solitons rotate over negative Q_0 during the collision and in F_x the domain in the negative vanishes during the collision and then emerges again, meaning the solitons do not stay a line connecting both fix points on the sphere during the collision. In all three observables the early decay of the solitons with positive Q_0 is visible.

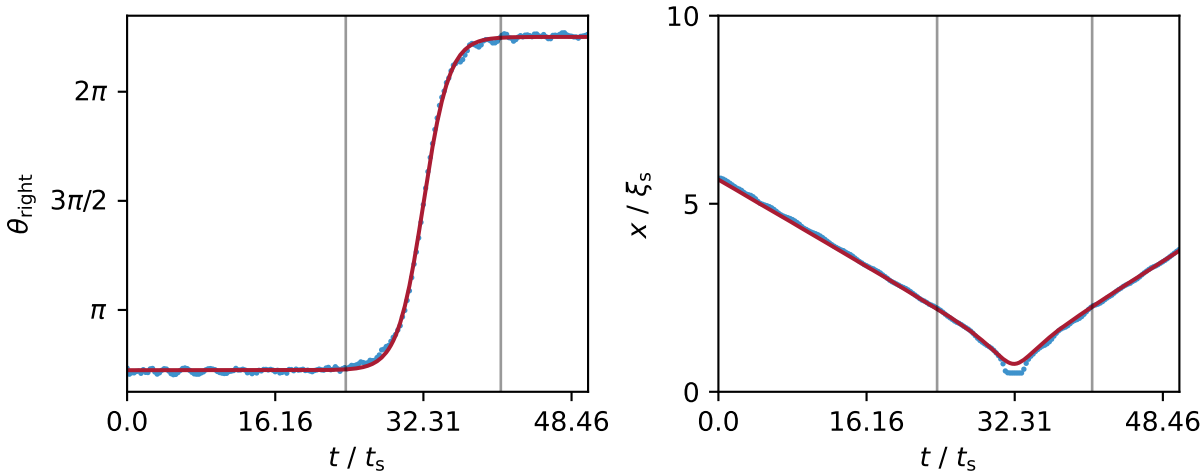

Figure 59: The tilt angle at the soliton position for the right soliton in the data shown in Fig. 58 still follows a tanh during the collision, which can also be fitted (red). Different to the collisions shown earlier (see Fig. 49), there are now clear deviations between the trajectory obtained from the tilt angle's time evolution (red) and the actual trajectory of the soliton during the collision. As can be seen in Fig 58, the solitons actually seem to become one small dip for a short time in F_x.

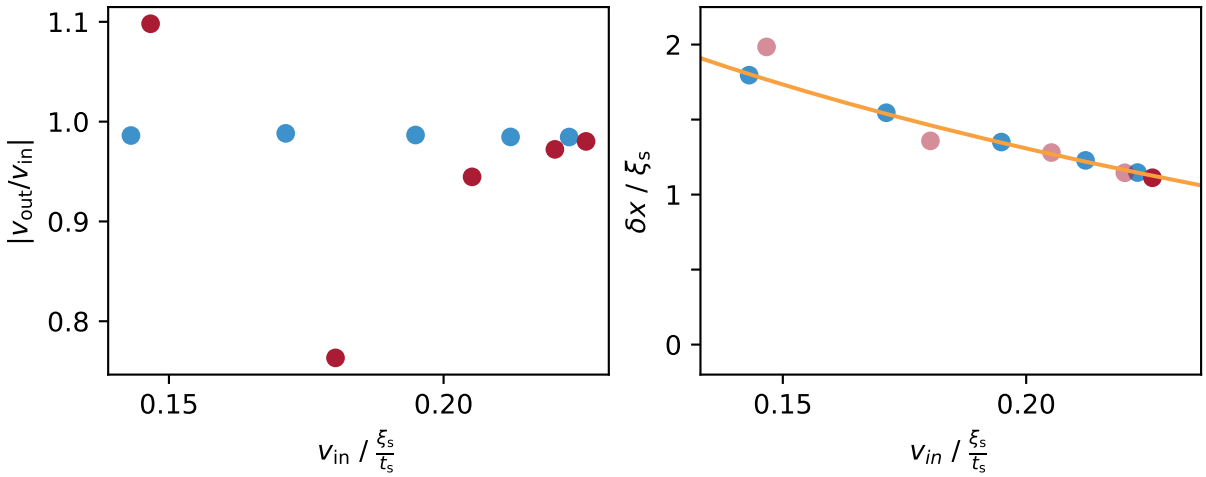

Figure 60: Elasticity and phase shift for different initial velocities due to different initial tilt angles. points with a positive Q_0 are marked red while those with a negative Q_0 are marked blue. For this data $q = 0.2n|c_1|$ was chosen and for the fit to the phase shifts all points with a elasticity deviating at maximum by 2% from one were used. The optimal parameters found for the fit (orange line) are shown in Eq. 71.

Additionally, for collisions of solitons with tilt angles $\theta \approx \frac{\pi}{2}$ at small q or at larger q even for a wider range of tilt angles, so called n-bounce collisions were observed. In such a collision, the solitons separate from each other after colliding to then change their direction and collide again. Depending on the number of collisions $n + 1$, the collision is then called an n-bounce collision (so for two collisions a 1-bounce collision). In two examples of these collisions, shown in Fig. 61, one can see that in the captured collisions in the spin-1 system, especially for the one at $q = 0.9n|c_1|$, the internal mode of the width oscillation of the solitons is excited. Interestingly, the time of the second collision and the third maximum of the width oscillation coincide with another. These collisions are an interesting topic for further investigation, as in the double sine-Gordon model, and similarly in the ϕ^4-theory, there are predictions for this internal mode and its relation to the structure of possible occurring bounces and the collisions are observed to have a fractal structure in their resonance spectra over the incoming velocity of the solitons v [31, 32].

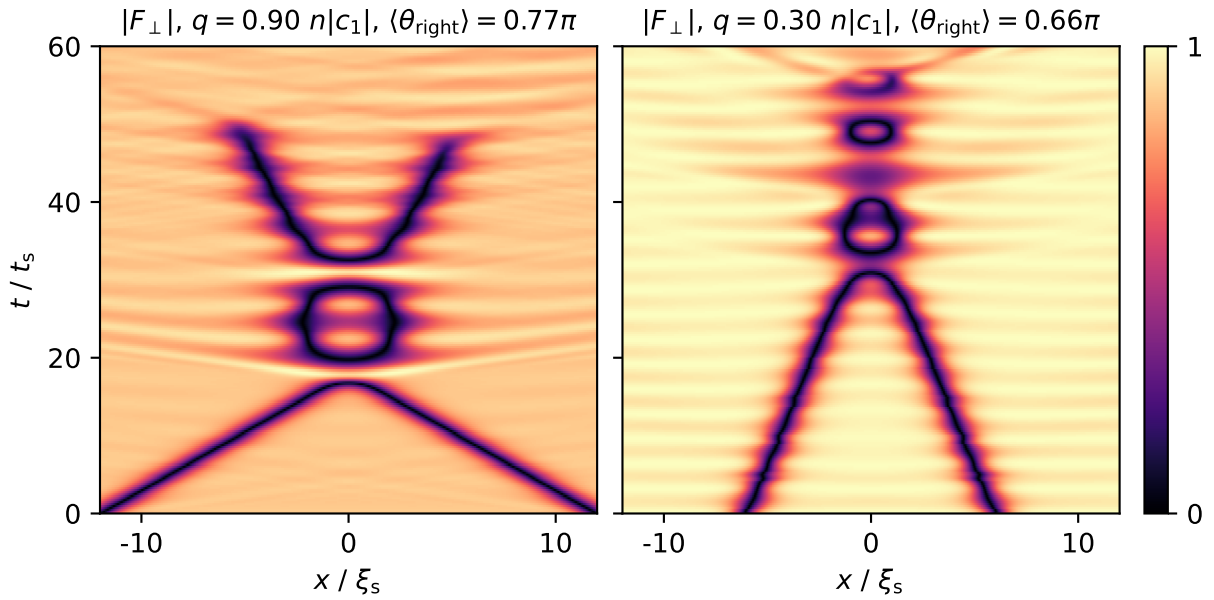

Figure 61: Two n-bounce collisions observed in the simulation. In both cases a tilt angle with a positive Q_0 expectation value at the soliton position was chosen. This leads to a decay after $t < 10 \cdot 2\pi t_s$. The data with $q = 0.90n|c_1|$ was taken with a matched background and the tilting from the FDS solution [17] while the data with $q = 0.30n|c_1|$ was taken with a matched background and the tilt realised by a rotation around F_x.

7 Discussion and outlook

In this thesis the sine-Gordon solitons previously observed in a ^{87}Rb spinor BEC were further investigated using a spin-1 mean-field GPE simulation, with a focus on free dynamics of a single soliton and their collisions. The goal of this simulations was to provide further insight regarding the sine-Gordon nature of the solitons, see how they can be controlled and observed best and if the spin-1 system shares other features with the sine-Gordon model, such as the existence of a breather solution.

First, the effect of experimental imperfections in the initial condition on the soliton dynamics was investigated, and it was found that perturbations in the imprint width lead to an oscillation of the soliton width approximately around the stable width $\ell = \frac{\xi_s}{\sqrt{2}}$. The larger the perturbation, the more this becomes an approximation, as the mean of the oscillation is slightly larger than ℓ. Unlike a soliton in the sine-Gordon model, changing the width of the soliton does not change its velocity, instead the experimental finding that the velocity depends linearly on the quadratic Zeeman shift q, which can also be understood in the framework of the effective theory, could be verified. Numerically it was validated that the zero crossing of the linear function is indeed at $q = 0$ and as observed in the experiment the solitons are also stable outside of the easy-plane phase when crossing the zero and the soliton velocity changes sign for this $v(-q) = -v(q)$. This linear relation is valid up to $|q| \approx 0.8n|c_1|$, when matching the background to the ground state of the easy-plane phase for the chosen q. An imperfect initial soliton shape and an oscillating background, due to the initial state being the ground state for $q = 0$, do not lead to a measurable difference in the velocity of the soliton for small q up to $|q| \leq 0.4n|c_1|$. When applying this constraint on the linear region of q used for the fit on the experimental data, the slope found by this fit matches the numerical slope well.

For a similar simulation with a matched background, a fit using the general dependence of the sine-Gordon mass m on q in the case $k \approx k_{\xi_s}$ can be made, although the found parameters cannot be compared to the predictions made in [2], as one would expect that the system is far from the sine-Gordon limit for the values of q needed to fit more than a linear function.

In addition to the profile of a sine-Gordon kink or antikink in the spinorphase, the profile of a sine-Gordon breather at $q \approx 0$ also leads to stable breathing, i.e., localised and time periodic dynamics, in the spinorphase, although the dynamical behaviour differs from the analytical sine-Gordon breather. While small amplitude breathers still behave similar to a sine-Gordon model, for larger amplitudes the frequency starts to differ from the expectation. The relation between initial imprint depth 2μ and resulting frequency of the breather ω was found to be described by $\omega = 2\cos^2\mu$ instead of $\omega = 2\cos\mu$, which would be the expectation from the sine-Gordon model. When imprinting the breather with a

constant width but different amplitudes, one also gets different frequencies for the different amplitudes. If the amplitude is too small compared to the set width, the frequency is larger than expected and if the amplitude is too large, the frequency is smaller than expected. This means when realising breathers in the experiment and comparing frequencies the correct initialisation is crucial. Additionally, starting at an initial amplitude of $\mu = \pi/4$, all points with an initial value of $\pi/2$ in the spinorphase oscillate around the potential minimum $\varphi_S = \pi$ instead of $\varphi_S = 0$. This was found to be due to the breather in spin-1 rotating rigidly around the F_x-axis of the spin-nematic sphere. To describe this rotation the tilt angle θ on the sphere was introduced.

Expanding on this, solitons tilted on this sphere by a tilt angle θ were simulated. These tilted solitons were found to be stable and now also connect the solitons described before to the DADD- and ADDAD-solitons described in [15] and the FDS described in [16–19]. For $q > 0$, it was found that the velocity of the solitons changed depending on the tilt angle. With a fit to the data for different tilt angles, the relation $v(\theta) = -v_{\max}(q)\cos\theta$ was obtained for this change. Tilting the solitons was also tested in the experiment by applying an additional RF-pulse for a rotation around F_x after the initialisation of a soliton imprint. The first results showed stable dips in Q_0 for up to approximately a second at the soliton position the depth of which can be controlled by the pulse length and that move with a lower velocity when the dip in Q_0 is larger, reaching $v \approx 0$ for the longest pulse duration used. This preparation seems to be very sensitive on a good calibration of the imprint, which has to be taken into account for future measurements but the data taken already strongly hints that preparing and measuring tilted solitons is possible in the experiment.

With the two possible ways found for controlling the soliton velocity collisions between kink and antikink were simulated. The results for the phase shift δx of a soliton due to the collision support the fact that in the limit of small q the solitons can be described by an effective sine-Gordon model, both when controlling the velocity by the tilt angle and by the quadratic Zeeman shift, respectively. However, the parameters found by fits of the sine-Gordon relation between phase shift and velocity differ between the data and in each case also at least one value differs from the prediction made by the effective model. While the sine-Gordon masses from the fit for different q to change the incoming velocity, match for a non-tilted ($\theta_{\text{init}} = \pi$) and a tilted ($\theta_{\text{init}} = \frac{5}{4}\pi$) soliton collision, for a constant $q = 0.20n|c_1|$ and different tilt angles a different sine-Gordon mass is obtained. In return this value matches the prediction from the effective theory for $k \approx k_{\xi_s}$ at $q \to 0$. The speed of sound obtained by the three fits was found to be different in all three cases. For the untilted solitons and different q, this is approximately one, meaning that for these solitons it agrees with the effective theory. For the tilted solitons the inverse of the speed of sound gets smaller than one, qualitatively agreeing with the found decrease in soliton

width in the spinorphase for a tilted soliton. Contrary to this, by just changing the tilt angle the optimal value found by the fit for the inverse of the speed of sound gets significantly larger.

When looking at the dynamics of a single soliton during the collisions, it was also found that the they can be described by the dynamics of the tilt angle. During the collision, the solitons explore the full nematic sphere and rotate over the pole with $Q_0 = -1$ to approximately the tilt angle with the same Q_0 expectation value they had before and the Q_{yz} undergoing a sign change as a result of the rotation. The time evolution of the tilt angle is given by $\tanh(t)$, opening the question for future research, whether this functional shape can be explained by deriving an equation of motion for the tilt angle and by this achieving a better understanding of the soliton and breather dynamics and interactions, especially for initial conditions leaving the equatorial plane of the nematic sphere. The change of the speed of sound for different initial tilt angles also implies that the underlying effective sine-Gordon model changes with the tilt angle. Together these results could explain the different phase shift relations found, as this would mean that during the collision the soliton explores a large variety of effective sine-Gordon models which all contribute to the resulting phase shift again summing up to the result expected by an effective sine-Gordon model. Additionally, n-bounce collisions, which are a hallmark of non-integrable dynamics, were found for the collisions of the tilted solitons in certain parameter regimes, especially solitons tilted to a positive Q_0 expectation value at the soliton position seem promising for achieving this kind of collisions. Further investigation of these collisions both numerically and in the experiment would especially be interesting regarding the resulting resonance spectra, as it inhabits a fractal structure in a double sine-Gordon model.

References

[1] Y. Deller et al., Observation of sine-Gordon solitons in a spinor Bose-Einstein condensate, submitted, 2025.

[2] I. Siovitz et al., Double sine-Gordon class of universal coarsening dynamics in a spin-1 Bose gas, *Phys. Rev. A* 112, 023304 (2025), DOI: 10.1103/df5w-3yfd.

[3] M. J. Ablowitz, Nonlinear Dispersive Waves: Asymptotic Analysis and Solitons, Cambridge University Press, 2011, ISBN: 9781107012547, DOI: 10.1017/CBO9780511998324.

[4] D. R. Christie, The morning glory of the Gulf of Carpentaria - A paradigm for non-linear waves in the lower atmosphere, *Aust. Met. Mag.* 41, 21–60 (1992).

[5] T. Heimburg and A. D. Jackson, On soliton propagation in biomembranes and nerves, *Proceedings of the National Academy of Sciences* 102.28, 9790–9795 (2005), DOI: 10.1073/pnas.0503823102.

[6] S. Burger et al., Dark Solitons in Bose-Einstein Condensates, *Phys. Rev. Lett.* 83, 5198–5201 (1999), DOI: 10.1103/PhysRevLett.83.5198.

[7] J. Denschlag et al., Generating Solitons by Phase Engineering of a Bose-Einstein Condensate, *Science* 287.5450, 97–101 (2000), DOI: 10.1126/science.287.5450.97.

[8] L. Khaykovich et al., Formation of a Matter-Wave Bright Soliton, *Science* 296.5571, 1290–1293 (2002), DOI: 10.1126/science.1071021.

[9] K. E. Strecker et al., Formation and propagation of matter-wave soliton trains, *Nature* 417, 150–153 (2002), DOI: 10.1038/nature747.

[10] B. Eiermann et al., Bright Bose-Einstein Gap Solitons of Atoms with Repulsive Interaction, *Phys. Rev. Lett.* 92, 230401 (2004), DOI: 10.1103/PhysRevLett.92.230401.

[11] A. Weller et al., Experimental Observation of Oscillating and Interacting Matter Wave Dark Solitons, *Phys. Rev. Lett.* 101, 130401 (2008), DOI: 10.1103/PhysRevLett.101.130401.

[12] S. Lannig et al., Collisions of Three-Component Vector Solitons in Bose-Einstein Condensates, *Phys. Rev. Lett.* 125, 170401 (2020), DOI: 10.1103/PhysRevLett.125.170401.

[13] A. Farolfi et al., Observation of Magnetic Solitons in Two-Component Bose-Einstein Condensates, *Phys. Rev. Lett.* 125, 030401 (2020), DOI: 10.1103/PhysRevLett.125.030401.

[14] X. Chai et al., Magnetic Solitons in a Spin-1 Bose-Einstein Condensate, *Phys. Rev. Lett.* 125, 030402 (2020), DOI: 10.1103/PhysRevLett.125.030402.

[15] C.-M. Schmied et al., Dark-antidark spinor solitons in spin-1 Bose gases, *Phys. Rev. A* 102, 053323 (2020), DOI: 10.1103/PhysRevA.102.053323.

[16] X. Yu and P. B. Blakie, Dark-soliton-like magnetic domain walls in a two-dimensional ferromagnetic superfluid, *Phys. Rev. Res.* 3, 023043 (2021), DOI: 10.1103/PhysRevResearch.3.023043.

[17] X. Yu and P. B. Blakie, Propagating Ferrodark Solitons in a Superfluid: Exact Solutions and Anomalous Dynamics, *Phys. Rev. Lett.* 128, 125301 (2022), DOI: 10.1103/PhysRevLett.128.125301.

[18] Y. Bai, J. Biguo and X. Yu, Ferrodark soliton collisions: breather formation, pair reproduction and spin-mass separation, 2025, arXiv: 2509.04769 [cond-mat.quant-gas].

[19] X. Yu, Oscillating ring ferrodark solitons with breathing nematic core in a homogeneous spinor superfluid, 2025, DOI: 10.48550/arXiv.2509.13874, arXiv: 2509.13874 [cond-mat.quant-gas].

[20] Y. Kawaguchi and M. Ueda, Spinor Bose–Einstein condensates, *Physics Reports* 520.5, Spinor Bose–Einstein condensates, 253–381 (2012), DOI: https://doi.org/10.1016/j.physrep.2012.07.005.

[21] P. Kunkel, Splitting a Bose-Einstein condensate enables EPR steering and simultaneous readout of noncommuting observables, dissertation, Universität Heidelberg, 2019, DOI: 10.11588/heidok.00027462.

[22] C. D. Hamley et al., Spin-nematic squeezed vacuum in a quantum gas, *Nature Physics* 8.4, 305–308 (2012), DOI: 10.1038/nphys2245.

[23] D. M. Stamper-Kurn and M. Ueda, Spinor Bose gases: Symmetries, magnetism, and quantum dynamics, *Rev. Mod. Phys.* 85, 1191–1244 (2013), DOI: 10.1103/RevModPhys.85.1191.

[24] H. Strobel, Fisher Information and entanglement of non-Gaussian spin states, dissertation, Universität Heidelberg, 2016, DOI: 10.11588/heidok.00020251.

[25] S. Lannig, Vector Solitons and Different Scenarios of Universal Dynamics in a Spin-1 Bose-Einstein Condensate, dissertation, Universität Heidelberg, 2022, DOI: 10.11588/heidok.00032047.

[26] B. Eiermann, Kohärente nichtlineare Materiewellendynamik - Helle atomare Solitonen, dissertation, Universität Konstanz, 2004, URL: http://web1.kip.uni-heidelberg.de/Veroeffentlichungen/download.php/4663/ps/diss_eiermann.pdf (visited on 20/11/2025).

[27] P. Kunkel et al., Simultaneous Readout of Noncommuting Collective Spin Observables beyond the Standard Quantum Limit, *Phys. Rev. Lett.* 123, 063603 (2019), DOI: 10.1103/PhysRevLett.123.063603.

[28] J. Cuevas-Maraver, P. G. Kevrekidis and F. Williams, The sine-Gordon Model and its Applications, Cambridge, England: Springer Nature, 2014.

[29] I. V. Baryakhtar, V. G. Baryakhtar and E. N. Economou, Kinetic and transport equations for localized excitations in the sine-Gordon model, *Phys. Rev. E* 60, 6645–6655 (1999), DOI: 10.1103/PhysRevE.60.6645.

[30] R. Koch and A. Bastianello, Exact thermodynamics and transport in the classical sine-Gordon model, *SciPost Phys.* 15, 140 (2023), DOI: 10.21468/SciPostPhys.15.4.140.

[31] D. K. Campbell, M. Peyrard and P. Sodano, Kink-antikink interactions in the double sine-Gordon equation, *Physica D: Nonlinear Phenomena* 19.2, 165–205 (1986), ISSN: 0167-2789, DOI: https://doi.org/10.1016/0167-2789(86)90019-9.

[32] R. H. Goodman and R. Haberman, Kink-Antikink Collisions in the ϕ^4 Equation: The n-Bounce Resonance and the Separatrix Map, *SIAM Journal on Applied Dynamical Systems* 4.4, 1195–1228 (2005), DOI: 10.1137/050632981.

[33] I. Siovitz, Universal scaling and emergent symmetries in a spin-1 Bose gas far from equilibrium, dissertation, Universität Heidelberg, 2025, DOI: 10.11588/heidok.00037531.

[34] F. Klein, Nonlinear Spin Dynamics Initiated by Local Control of the Spinor Phase in a Bose-Einstein Condensate, Masterarbeit, Universität Heidelberg, 2024, URL: https://www.kip.uni-heidelberg.de/Veroeffentlichungen/download.php/7046/temp/4790.pdf (visited on 20/11/2025).

[35] Y.-J. Lin et al., Synthetic magnetic fields for ultracold neutral atoms, *Nature* 462, 628–632 (2009), DOI: 10.1038/nature08609.

[36] F. Schmidt et al., Precision measurement of the ^{87}Rb tune-out wavelength in the hyperfine ground state $F = 1$ at 790 nm, *Phys. Rev. A* 93, 022507 (2016), DOI: 10.1103/PhysRevA.93.022507.

[37] A. Flamm, Novel readout sequences and local control for spinor Bose-Einstein condensates, Masterarbeit, Universität Heidelberg, 2025, URL: https://https://www.kip.uni-heidelberg.de/Veroeffentlichungen/details.php?id=4955 (visited on 20/11/2025).

A Additional plots

A.1 Theoretical and experimental background

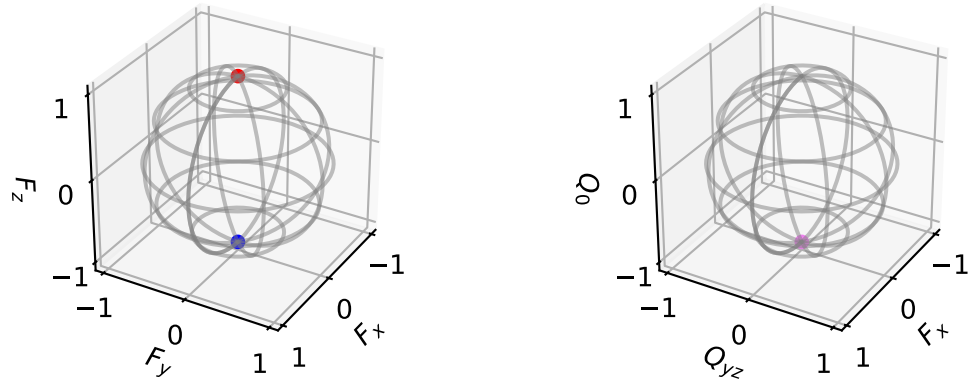

Figure A1: The groundstate of the easy-axis ferromagnet phase on the spin sphere (left) and the spin-nematic sphere (right). On the spin sphere the state is located either on the north or the south pole, which means that the spin is fully elongated and aligned along F_z. This directly leads to $Q_0 = -1$, which means that it is located on the south pole of the spin-nematic sphere.

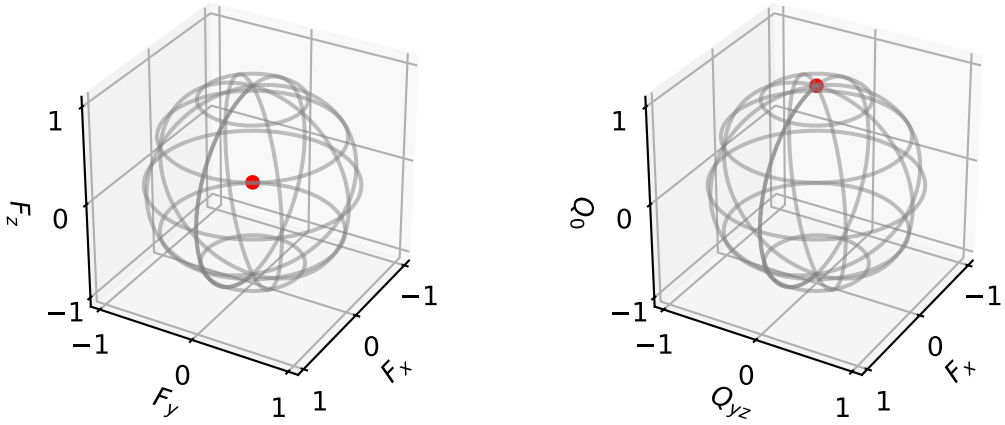

Figure A2: The groundstate of the polar phase on the spin sphere (left) and the spin-nematic sphere (right). In this state all atoms are in the $m_F = 0$-mode, leading to all F_i having an expectation value of 0 and $Q_0 = 1$.

A.2 Single solitons

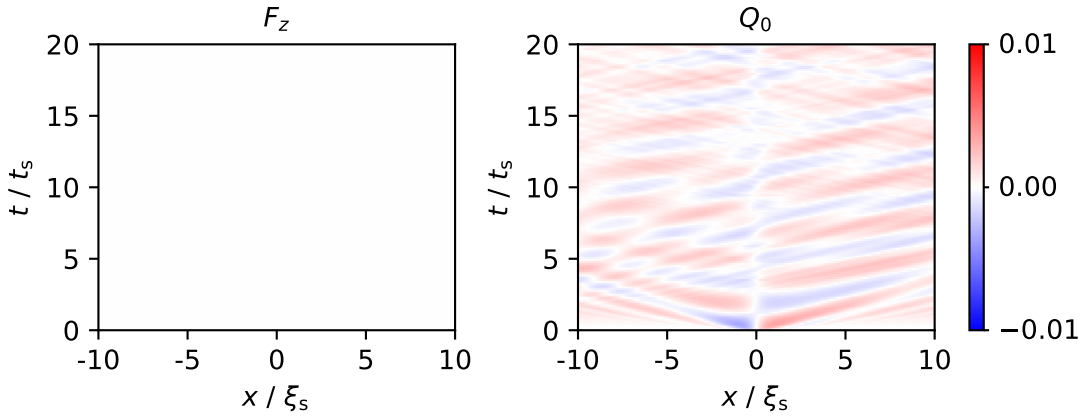

Figure A3: F_z for the soliton at $q \approx 0$ is flat. In Q_0 there is also radiation below the one percent level in the formation of the soliton. This radiation presents itself as oscillation that are shifted by a phase of π on the two sides of the soliton.

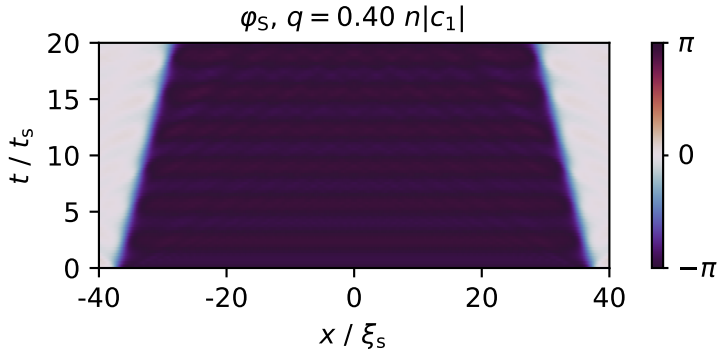

Figure A4: Kink (right) and antikink (left) moving in opposite direction with the same velocity for a given $q \neq 0$. For the initial condition closer to the experiment and an unmatched $|F_\perp|$ background, oscillations in the spinorphase background are visible.

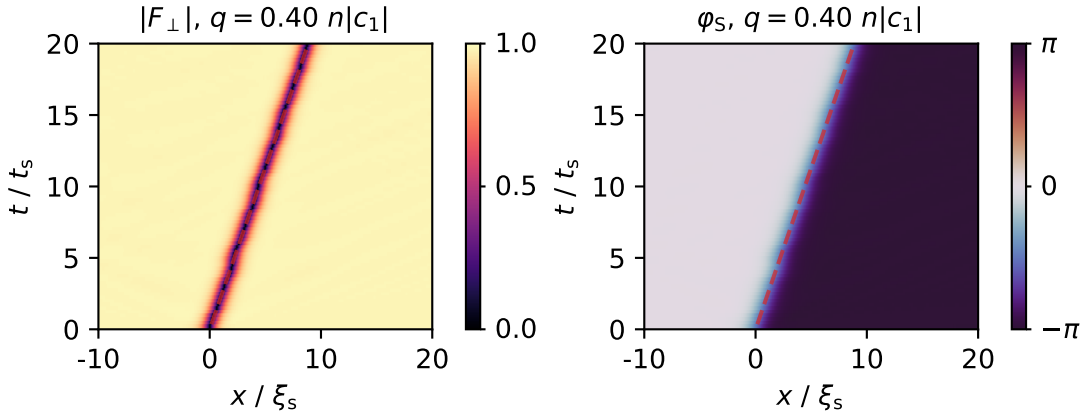

Figure A5: The moving soliton at $q = 0.40n|c_1|$ in $|F_\perp|$ and φ_S with a matched background and the correct imprint shape. The dashed line is the linear fit to the trajectory.

A.3 Breather

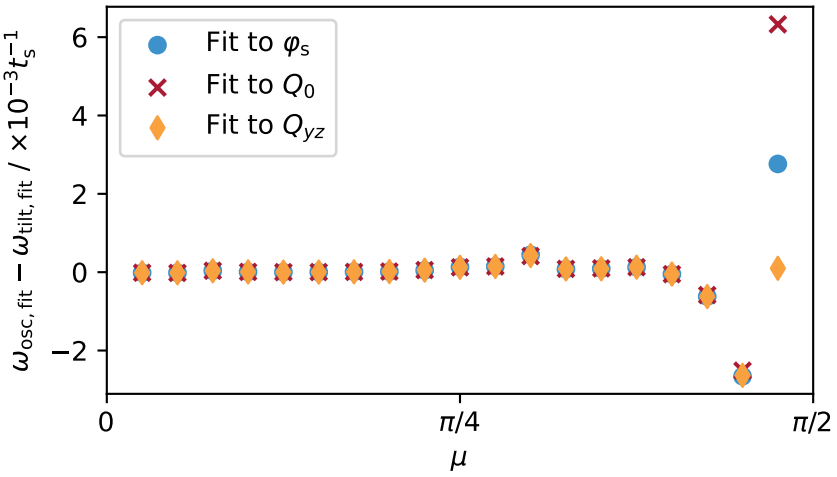

Figure A6: The frequencies as extracted for the breather, when changing μ, for the three oscillations in φ_S, Q_0, and Q_{yz} all compared to the frequency extracted from the linear fit to the tilt angle. The deviations get larger for large μ, where less than one period of the fit is captured, which makes the oscillation fits less exact.

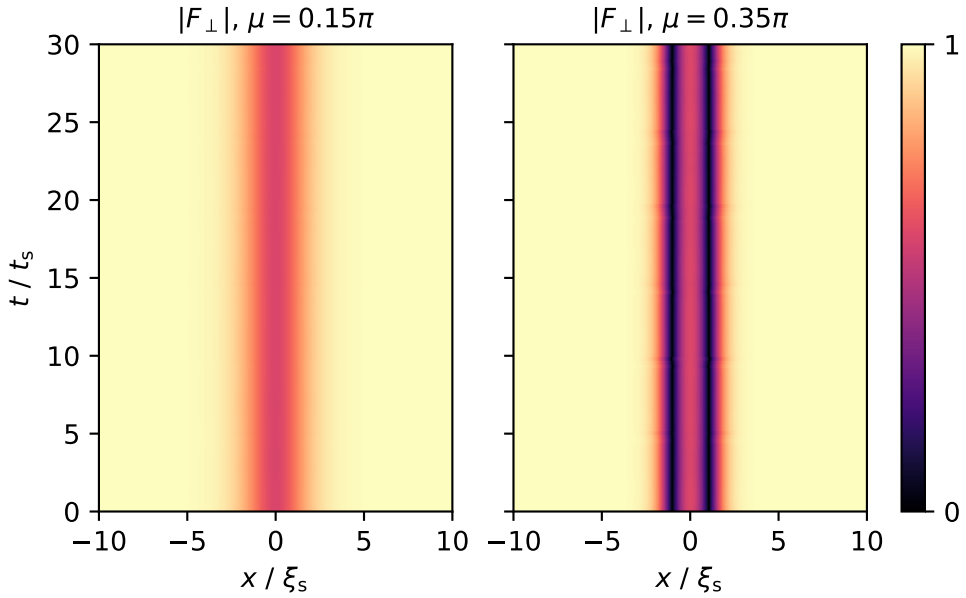

Figure A7: The breathers shown in Fig. 32 and 33 in $|F_\perp|$. While for an initial $\mu < \pi/4$ only one dip is visible, for larger values it looks similar to the $F_\perp$ profile of two solitons close to each other (compare Fig. 20).

A.4 Collisions

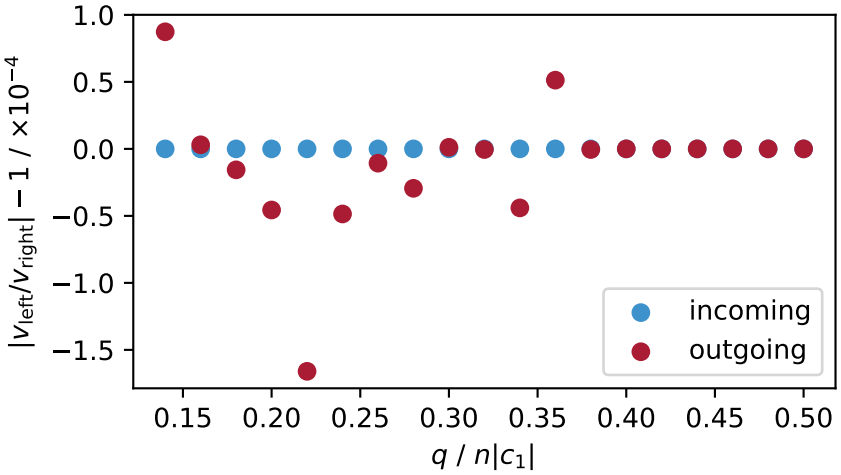

Figure A8: The velocity of the left and right soliton for different q and untilted soliton with a matched background is in good approximation the same, as the ratio of the two velocities differs for the outgoing solitons by less than $2 \cdot 10^{-4}$ from one and for the incoming solitons on an even lower level.

Acknowledgements

At first, I would like to thank Markus for giving me the opportunity to, after my bachelor's thesis, again work in his group at the BEC and supervising my thesis. The meetings were always a great source of inspiration thanks to your curiosity and excitement.

Furthermore, I would like to thank Thomas for agreeing to be the second referee of my thesis.

Additionally, I would like to thank Helmut for always giving additional insight with his experience, and, especially in the lab, somehow always knowing what to check when there is a problem.

A special thanks goes to Yannick, Alex, and Alex for taking time to answer all my questions, lots of good discussions, proof-reading my thesis, and aside from that always being open for a joke in the lab or office.

A big thanks also has to go to Ido for sharing the code used for all the simulations in this thesis and answering my questions regarding it, and best practices for simulations on the EINC.

As his successor in questions regarding the EINC and the trips to our office, I also want to thank Andreea for listening to my complaints, when no GPU was available.

Another thanks goes to Christiane and Petra for helping with all administrative questions.

A thank you also goes to all the other people from the Matterwave-group for all the good and funny discussions at lunch, the DPG, PhD defenses, or just during the day in the offices or labs.

At last, I also would like to thank Chiara and all my friends and family for supporting me all the time and always listening to me talk, likely too much, about the project.

Erklärung:

Ich versichere, dass ich diese Arbeit selbstständig verfasst habe und keine anderen als die angegebenen Quellen und Hilfsmittel benutzt habe.

Heidelberg, den 21.11.2025

R. Schäfer